Integrated Visible-Light Platforms, Devices, and Systems for Augmented Reality and Beyond

by

Milica Notaros

B.S., University of Colorado Boulder (2017)
S.M., Massachusetts Institute of Technology (2019)

Submitted to the
Department of Electrical Engineering and Computer Science
in partial fulfillment of the requirements for the degree of

DOCTOR OF PHILOSOPHY

at the

MASSACHUSETTS INSTITUTE OF TECHNOLOGY

September 2023

Authored by: Milica Notaros
Department of Electrical Engineering and Computer Science
August 31, 2023

Certified by: Erich P. Ippen
Elihu Thomson Professor of Electrical Engineering Emeritus
Professor of Physics Emeritus
Thesis Supervisor

Accepted by: Leslie A. Kolodziejski
Professor of Electrical Engineering and Computer Science
Chair, Department Committee on Graduate Students

Integrated Visible-Light Platforms, Devices, and Systems for Augmented Reality and Beyond

by

Milica Notaros

Submitted to the Department of Electrical Engineering and Computer Science
on August 31, 2023, in partial fulfillment of the requirements for the degree of
DOCTOR OF PHILOSOPHY

Abstract

Augmented-reality head-mounted displays have many wide-reaching applications in defense, medicine, etc. However, current commercial head-mounted displays are bulky, heavy, and indiscreet. Moreover, these current displays are not capable of producing holographic images with full depth cues; this lack of depth information results in users experiencing eyestrain and headaches that limit long-term and wide-spread use of these displays. Here, to address these limitations, VIPER (Visible Integrated Photonics Enhanced Reality), a novel integrated-photonics-based holographic display, is developed and demonstrated. The VIPER display consists of a single transparent chip that sits directly in front of the user's eye and projects 3D holograms.

First, this VIPER display concept is proposed. Second, the first transparent 300-mm-wafer foundry platform on glass for visible-light integrated photonics is developed. Third, a novel passive optical-phased-array-based architecture and holographic image encoding methodology are developed and used to demonstrate a large-scale passive version of the VIPER display. Fourth, to enable compact and efficient modulation for dynamic encoding of the VIPER display, liquid-crystal material is integrated into the VIPER platform and used to demonstrate the first integrated visible-light liquid-crystal-based phase and amplitude modulators. Fifth, these liquid-crystal-based modulators are leveraged to demonstrate the first actively-tunable visible-light integrated optical phased arrays. Sixth, these liquid-crystal-based components are used to develop and demonstrate a novel active version of the optical-phased-array-based VIPER pixel. Seventh, the architecture for the full active VIPER display is developed and used to demonstrate dynamic video display functionality.

Finally, applications beyond augmented reality are presented, including chip-based underwater communications, 3D printers, trapped-ion systems, and optical tweezers.

Thesis Supervisor: Erich P. Ippen
Title: Elihu Thomson Professor of Electrical Engineering Emeritus
Professor of Physics Emeritus

Acknowledgments

I want to thank my thesis supervisor, Prof. Erich Ippen. I feel genuinely honored to be able to say that I worked with and was advised by Prof. Ippen. He gave me such meaningful advice and guidance, pointing out what things should be explored further and also highlighting successes and things that were going well. Prof. Ippen, I am incredibly grateful for all that you have done for me.

I would also like to thank Prof. Jelena Notaros, who is the PI on this work. Her drive and ambition as a researcher and adviser enables her students to accomplish really great things. I have seen firsthand just how much Jelena cares about her research group and her students, both with respect to their work and with respect to themselves as people. Jelena, thank you for all the effort that you put into your research group and into your students.

I would like to thank my remaining thesis committee members, Prof. Duane Boning and Prof. Juejun Hu, both of whom I have had the great experience of collaborating with. They both make significant impacts on the field of silicon photonics, not only in research in the area, but also in bringing the field of silicon photonics to others through education.

I would like to thank Dr. Michael Watts and members of the Photonic Microsystems Group, specifically Manan Raval and Diedrik Vermeulen, who were an important part of the initial work on the VIPER project.

Also, a huge thank you to the Photonics and Electronics Research Group (PERG): Prof. Jelena Notaros, Sabrina Corsetti, Tal Sneh, Ashton Hattori, Daniel DeSantis, Andres Garcia Coleto, Michael Torres, Benjamin Mazur, Henry Crawford-Eng, Abigail Shull, Dianne Lior, and Pearl Nelson-Greene. One of my favorite things about this group is the ability to do strong, impactful research, while maintaining the cool, relaxed PERG energy. When the new students started trickling into the group about two years ago, they brought such positive energy and excitement with them. I have definitely thrived from being around them, both in terms of research and personally. I will definitely miss seeing them every day in the office and in the lab. PERGers,

you all should be really proud of what you have already managed to achieve in two years or less, and I am so excited to see what you all accomplish in the future.

I would also like to thank the Antenna Research Group at CU Boulder, which is led by my undergraduate research advisor, Prof. Dejan Filipovic. They first introduced me to and got me interested in research as an undergraduate student. Thank you all for being so welcoming and helpful.

The majority of the platforms, devices, and systems demonstrated in this work were fabricated at the State University of New York Polytechnic Institute's (SUNY Poly) Albany NanoTech Complex in Albany, New York. A special thank you to Thomas Dyer, Christopher Baiocco, Daniel Coleman, Kevin Fealey, and Seth Kruger, with whom we closely collaborated.

I would also like to thank Kurt Broderick and Gary Riggott for training me on the originally daunting tools and processes in the Massachusetts Institute of Technology fabrication facilities and for their complete willingness to share their extensive knowledge. The in-house fabrication and liquid-crystal packaging done in this work would not have been possible without their advice and guidance.

Additionally, I would like to thank our collaborators at MIT Lincoln Laboratory and the MIT Quanta Group, who we collaborated with on the trapped-ion-cooling project, namely, John Chiaverini, Robert McConnell, Reuel Swint, Patrick Callahan, Gavin N. West, Felix Knollmann, Thomas Mahony, Ethan R. Clements, Cheryl Sorace-Agaskar, Dave Kharas, and Colin Bruzewicz. I would like to thank our collaborators in the MIT Biological Microtechnology and BioMEMS Group, who we collaborated with on the optical trapping project, namely, Prof. Joel Voldman and Kruthika Kikkeri. Also, I would like to thank our collaborators in the ZAP Group at UT Austin, who we collaborated with on the 3D printing project, namely, Prof. Zachariah A. Page and Alex Stafford.

I would like to thank the RLE, MTL, MIT.nano, and EECS staff, especially Melissa Sheehan, Stephanie Muto, Bill Gibbs, Matthew McGlashing, Bill Adams, Prof. Leslie Kolodziejski, Janet Fischer, Alicia Duarte, and Kathy McCoy.

This work was supported by the Defense Advanced Research Projects Agency

(DARPA) Visible Integrated Photonics Enhanced Reality (VIPER) program (Grant No. FA8650-17-1-7713) (managed by Dr. Gordon Keeler), the National Science Foundation (NSF) Graduate Research Fellowship Program (GRFP) (Grant No. 1122374), the National Science Foundation (NSF) CAREER Program (Grant No. 2239525), and a Massachusetts Institute of Technology Jacobs Presidential Fellowship.

I would like to thank all the friends I have made along the way, both before MIT and during my time here. It is so helpful to have great friends that can be attenuators when there is a difficult situation, amplifiers when there is an exciting success, and isolators to separate work and fun.

My family has always been so important to me, and we have always been so close. Mama, Tata, Jelena, Tesh, and Max, you all mean so much to me.

My parents are the reason why I am here, in so many ways, and they are so supportive of me. They are always around to celebrate successes, and, more importantly, they are always around to help when there is a problem or challenge; they help give advice and find a solution. I honestly cannot imagine what it would even mean to have parents that are more supportive.

Jelena, Tesh, and Maxime, you all have been my home base here in Cambridge.

Jelena puts so much care and effort into everything that she does. When Jelena cares about something or someone, she will do absolutely everything in her power to help that person. Whether that be with some much-needed tough love or with great empathy. She is truly an outstanding role model, both personally and academically, whom I greatly admire and look up to.

Maxime came into my life two years ago. When I think about my life from before then and compare it to my life now, it is almost completely incomparable. My life is just so different in so many wonderful ways with Max in it. It makes such a world of difference when you have someone that you know will always be there for you, no matter what. Max, you have made my life so much better and richer.

Contents

List of Figures

Chapter 1

Introduction

1.1 Introduction to Visible-Light Applications and Head-Mounted Displays

Integrated photonics systems at visible wavelengths have many wide-reaching potential applications, including image-projection systems [1–4], underwater optical communications [5–9], trapped-ion systems [10–14], and optogenetics [15–19], as shown in Fig. 1.1.

One very impactful visible-light application area is head-mounted displays. In many situations, such as military operations and medical procedures, access to real-time information can be a key determinant for success (Fig. 1.2) [20–23]. Traditionally, this information has been displayed in real time using head-down or head-up displays [24]. However, recently, there have been extensive efforts in developing head-mounted displays that are capable of relaying information directly in the user's field of view (FOV) [25–28]. These head-mounted displays enable the user to remain engaged with their surroundings while referencing information to real-world objects and events for an augmented-reality experience.

Typical commercially-available augmented-reality head-mounted displays employ an optical relay system for each eye, wherein an image produced by a microdisplay is magnified using a system of lenses to generate an image superimposed on the

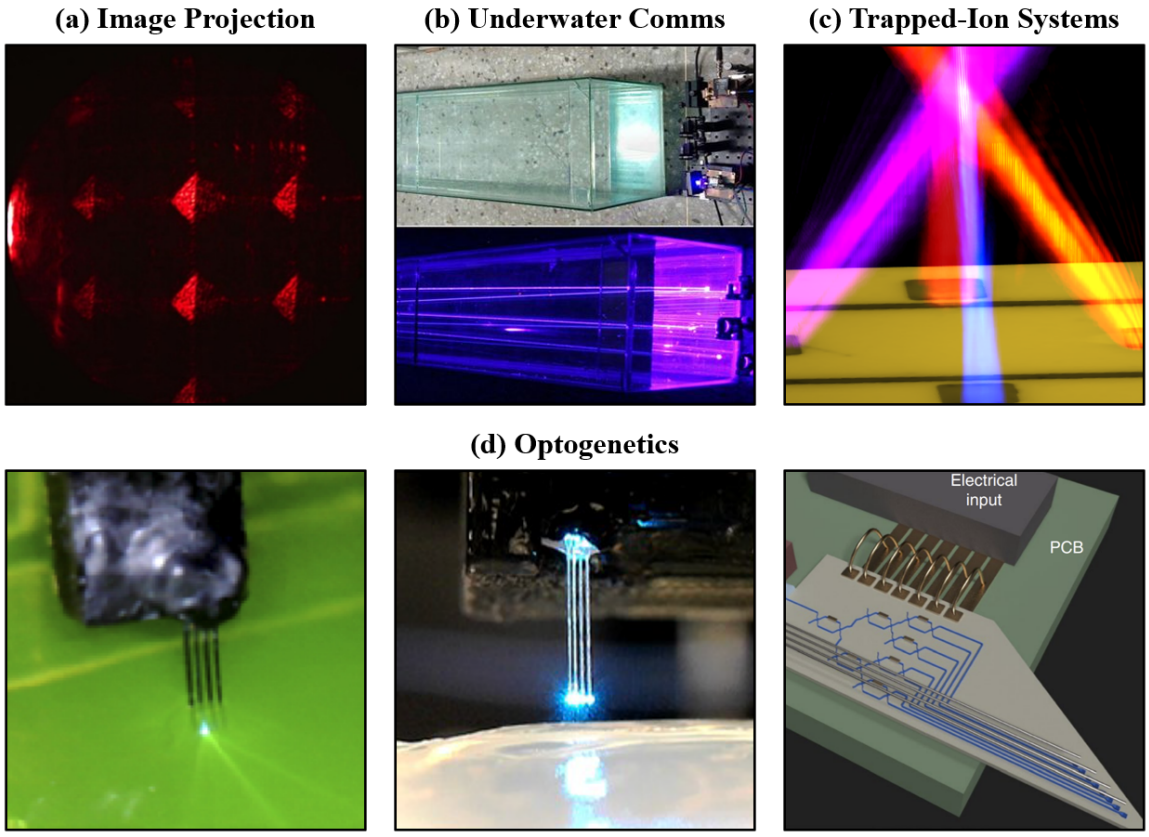

Figure 1.1: Overview of select visible-light applications, including (a) image projection (figure from [2]), (b) underwater optical communications (figure from [8]), (c) trapped-ion systems (figure from [10]), and (d) optogenetics (figures from [15, 18, 19]).

external scene at a single virtual focal plane in the user's FOV [26–28], as shown in Fig. 1.3. However, the bulk-optics components utilized in these typical head-mounted

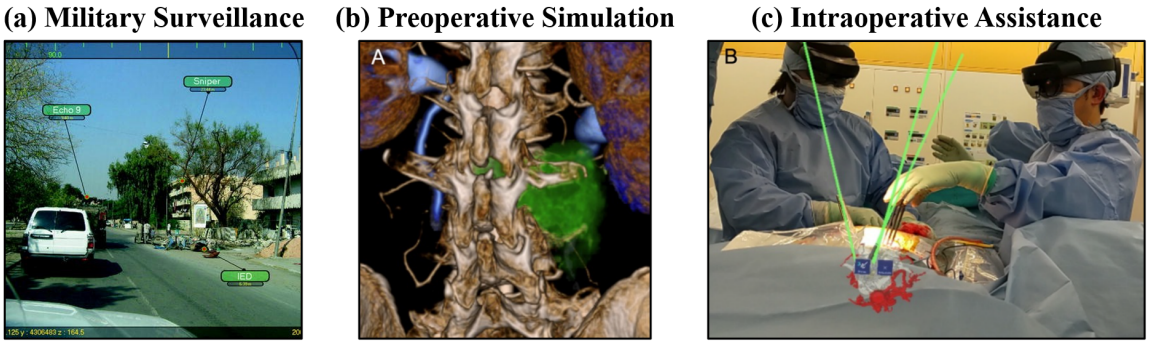

Figure 1.2: Overview of select use cases for augmented and virtual reality, including (a) military surveillance (figure from [20]), (b) preoperative simulations for surgery (figure from [23]), and (c) intraoperative assistance during surgery (figure from [23]).

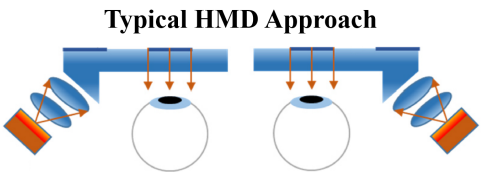

Figure 1.3: Simplified diagram of a typical head-mounted-display approach using an optical relay system.

displays result in large, heavy, and indiscreet systems. Additionally, typical head-mounted displays employ low-luminance microdisplays (approximately 1000 cd/m2), which render the systems inadequate for use in ambient daylight conditions, and optical relay systems with limited FOVs (limited to $< 40°$ compared to the $60°$ near-peripheral FOV of the human eye). Finally, typical head-mounted displays magnify the microdisplay image such that it appears at a single virtual focal plane (they are not capable of producing holographic images with full depth cues); this lack of depth information results in users experiencing eyestrain and headaches that limit long-term and wide-spread use of these displays (an effect known as the vergence-accommodation conflict, whose origin is depicted in Fig. 1.4) [29–31].

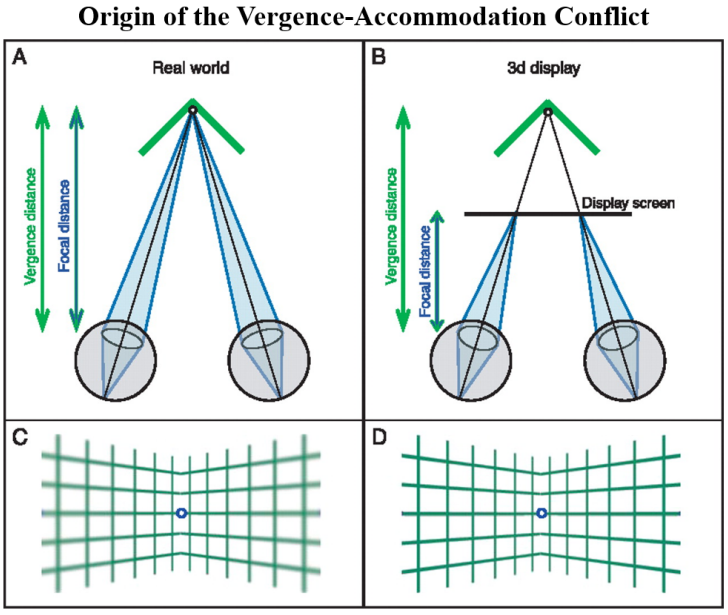

Figure 1.4: Origin of the vergence-accommodation conflict, showing that the vergence and accommodation distance are equal for a user viewing their environment, but different for a user of a typical 3D display (figure from [30]).

Although there have been a number of recent proposals and initial passive demonstrations of near-eye displays that utilize holographic image projection to emit full phase fronts and resolve the vergence-accommodation conflict [2,32–38], there is still a growing need for a dynamic, discrete, mobile, large-FOV, high-brightness augmented-reality head-mounted display with full binocular and monocular depth cues.

1.2 Introduction to VIPER

The field of silicon photonics has the potential to enable a paradigm-shifting solution to address this need for a next-generation augmented-reality display. By enabling chip-scale optical microsystems with new functionalities, improved system performance, and reduced size, weight, and power, silicon photonics has enabled next-generation optical technologies that have facilitated revolutionary advances for numerous fields spanning science and engineering, including computing, communications, sensing, and quantum engineering, as shown in Fig. 1.5 [10–14, 39–42].

An emerging class of integrated photonic systems is integrated optical phased arrays, which consist of an array of on-chip optical antennas fed with controlled phases and amplitudes using an integrated photonic circuit, enabling emission and dynamic control of free-space radiated light in a compact form factor, at low costs, and in a non-mechanical way [42–58]. Select demonstrations are shown in Fig. 1.6.

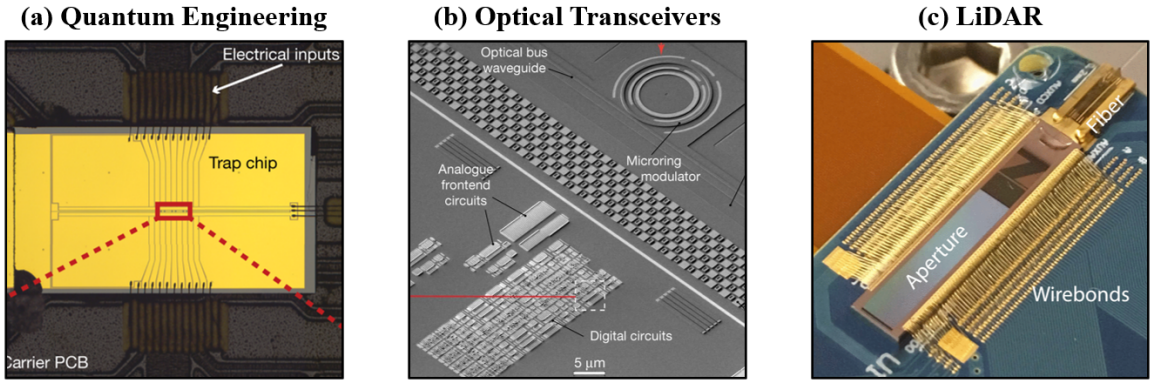

Figure 1.5: Overview of select advances achieved with silicon photonics, including (a) quantum engineering (figure from [14]), (b) optical transceivers (figure from [39]), and (c) light detection and ranging (LiDAR) (figure from [42]).

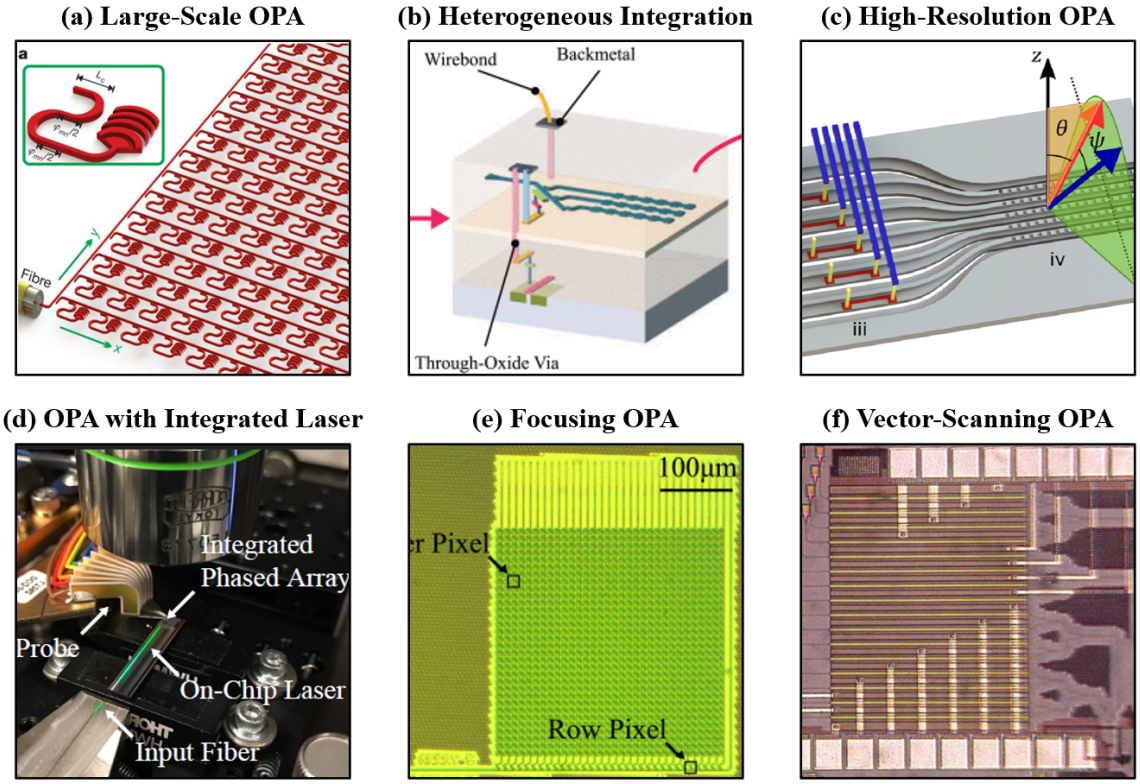

Figure 1.6: Overview of select integrated optical-phased-array demonstrations (a) large-scale two-dimensional optical phased array (figure from [45]), (b) active optical phased array heterogeneously integrated with CMOS electronics (figure from [46]), (c) high-resolution beam-steering optical phased array (figure from [53]), (d) optical phased array integrated with an erbium-doped laser (figure from [48]), (e) near-field focusing optical phased array (figure from [47]), (f) vector-scanning optical phased array (figure from [51]).

As such, optical-phased-array-based systems have already emerged as a prominent and promising solution for next-generation LiDAR sensors for autonomous vehicles [42–44]. However, motivated by this initial LiDAR application, integrated-optical-phased-array demonstrations to date have primarily focused on systems that operate at infrared wavelengths and that form and non-mechanically steer beams in the far field of the array. Integrated optical phased arrays, and the field of silicon photonics in general, have never before been leveraged to successfully demonstrate an augmented-reality display.

In this work, VIPER (Visible Integrated Photonics Enhanced Reality), a novel integrated-photonics-based visible-light near-eye holographic display, is proposed and

experimentally demonstrated as a scalable solution to address this need for an advanced augmented-reality display. The VIPER display consists of a single discreet transparent chip that sits directly in front of the user's eye to enable a direct-view near-eye display approach. The display is comprised of a grid of on-chip visible-light optical phased arrays that are encoded to emit light with the appropriate amplitudes and phases to form a virtual holographic image that only the user can see. It presents a highly discreet and fully holographic solution for the next generation of augmented-reality displays.

1.3 VIPER Concept

The proposed VIPER display consists of a single discreet transparent chip that sits directly in front of the user's eye, as shown in Fig. 1.7, and projects visible-light 3D holograms that only the user can see.

The VIPER chip is fabricated in a custom 300-mm-diameter silicon-photonics process at the State University of New York Polytechnic Institute's (SUNY Poly) Albany NanoTech Complex to take advantage of the scaled production, reduced cost, and increased reliability of the CMOS-foundry model. A first-of-its-kind custom wafer-scale fabrication process that transfers the photonics layers from a traditional opaque silicon substrate to a transparent glass wafer was developed (the transparent

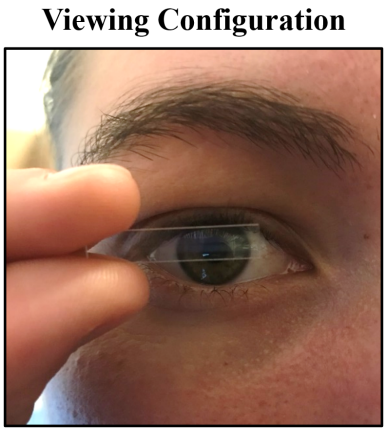

Figure 1.7: A glass-bonded VIPER chip in the near-eye modality, demonstrating how the VIPER display would be used for augmented reality.

wafer-scale fabrication process is described in Sec. 2.2.1). This fabrication process enables a highly discreet and transparent augmented-reality system.

This transparent platform enables the VIPER chip to sit directly in front of the user's eye, as shown in Fig. 1.7, to enable a direct-view near-eye display approach, as shown in Fig. 1.8a, which eliminates the need for an optical relay system typically required for traditional head-mounted displays. Instead, the display emulates the specific amplitude and phase distribution of the light necessary to generate a virtual holographic image behind the display and projects that information to the retina of the user, as shown in Fig. 1.8b (this is in comparison to traditional displays that only contain amplitude information generated by a microdisplay and, as a result, are unable to generate holographic images with proper depth cues).

To generate this holographic information, the VIPER display utilizes a 2D grid of on-chip visible-light integrated optical phased arrays that act as the pixels of the display, as shown in Fig. 1.9. These optical-phased-array-based pixels are encoded to emit light with the appropriate amplitudes and phases such that a holographic image is formed. Specifically, the phase and amplitude distributions necessary for generating the desired holographic image on the retinal plane are closely approximated

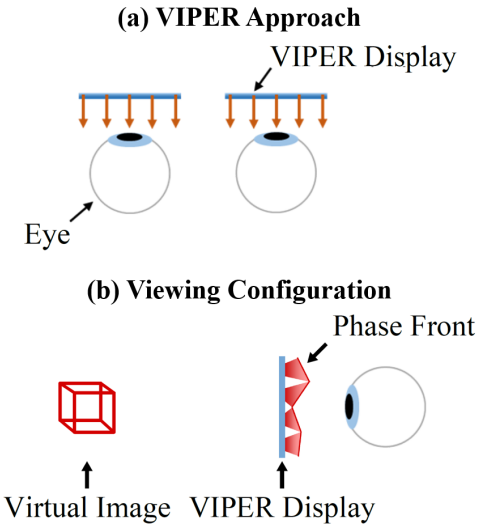

Figure 1.8: (a) Simplified diagram of the direct-view near-eye VIPER approach. (b) Viewing configuration for the VIPER display showing the virtual-image hologram formed behind the display.

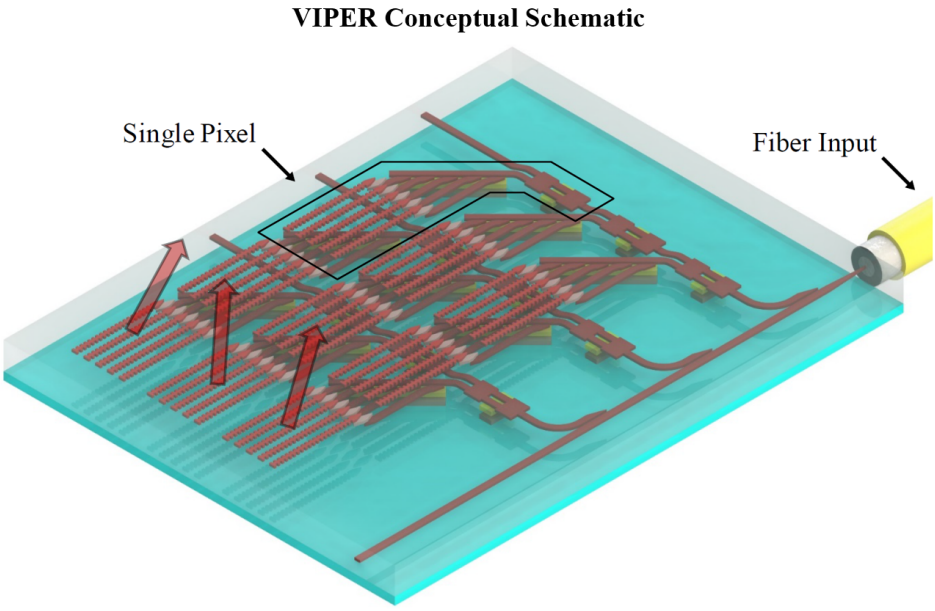

Figure 1.9: Simplified schematic of the VIPER display concept showing the input optical fiber, active distribution network, and grid of optical-phased-array-based pixels.

by discretizing these distributions into local one-dimensional phase gradients with arbitrary amplitudes and absolute phases corresponding to the size of the pixels in the display.

To enable routing and emission of light at visible wavelengths, the system is based on silicon-nitride waveguides, since silicon nitride has a low absorption coefficient within the visible spectrum and is CMOS compatible. However, silicon nitride has a low thermo-optic coefficient and does not exhibit significant electro-optic properties, which has made integrated modulation at visible wavelengths challenging [59,60]. As such, liquid-crystal material, with a strong birefringence in the visible spectrum, is integrated into the VIPER platform and used to enable dynamic modulation and encoding of the optical-phased-array-based pixels.

Finally, the VIPER display is designed to be heterogeneously integrated with a custom thin-film-transistor electronics backplane to enable integrated control of the display and future scaling up to a large-scale video-hologram demonstration with multi-wavelength RGB functionality.

1.4 Thesis Overview

This thesis details key platform, device, architecture, and fabrication development and proof-of-concept experimental demonstrations that pave the way towards the VIPER display vision.

First, in Sec. 1.3, this general VIPER display concept is proposed and outlined.

Second, in Ch. 2, to enable fabrication of the VIPER display, the first transparent 300-mm-wafer foundry platform on glass and the first 300-mm-wafer foundry platform on flexible substrates are developed for visible-light integrated photonics.

Third, in Ch. 3, as an initial proof-of-concept demonstration, a novel passive optical-phased-array-based architecture and holographic image encoding methodology are developed and used to demonstrate a large-scale passive version of the VIPER display that generates a static virtual holographic image.

Fourth, to enable compact and efficient modulation for dynamic encoding of the VIPER display, liquid-crystal material is integrated into the VIPER platform and used to demonstrate the first integrated visible-light liquid-crystal-based phase and amplitude modulators. In Ch. 4, background information on important liquid-crystal properties is given, integration of the liquid-crystal media with the photonics platform is discussed, and the in-house chip-scale liquid-crystal packaging process is described.

In Ch. 5, the first integrated visible-light liquid-crystal-based phase modulators are proposed, designed, and experimentally demonstrated. These devices utilize the birefringence of liquid crystal to vary the effective refractive index of the mode in a waveguide situated directly underneath the liquid crystal to induce a phase shift. The device operation is described, key variables that affect the mode interaction and resulting phase shift are discussed, and phase modulation is experimentally demonstrated.

In Ch. 6, we propose and experimentally demonstrate the first integrated visible-light liquid-crystal-based variable-tap amplitude modulators. These devices leverage the birefringence of liquid-crystal medium to actively tune the coupling coefficient between two waveguides and, hence, vary the amplitude of light coupled between

these waveguides. First, we propose and develop the theory behind these integrated liquid-crystal-based variable-tap devices. Next, we outline the design procedure for how we determine the optimal waveguide widths and coupler lengths of these devices to maximize amplitude modulation. Finally, we demonstrate experimental results of example fabricated devices.

Fifth, in Ch. 7, these liquid-crystal-based modulators are leveraged to demonstrate the first actively-tunable visible-light integrated optical phased arrays.

Sixth, in Sec. 8.1, these liquid-crystal-based components are used to develop a novel compact and efficient active version of the optical-phased-array-based VIPER pixel and experimentally validate its functionality. Seventh, using this active pixel as a building block, the architecture for the full active VIPER display is developed and used to demonstrate initial dynamic video display functionality, in Sec. 8.2.

Finally, in Ch. 9, applications beyond augmented reality are presented, including underwater optical communications, chip-based 3D printers, trapped-ion quantum systems, and integrated optical tweezers.

Chapter 2

Integrated Visible-Light Silicon-Photonics Platform, Fabrication Process, and Transfer Process to Unique Substrates

In this chapter, our developed visible-light silicon-photonics platform and fabrication process are discussed in Sec. 2.1. Then, our developed wafer-scale transfer process to unique substrates is discussed in Sec. 2.2, with our transparent silicon-photonics wafer-scale fabrication process and results discussed in Sec. 2.2.1 and our flexible silicon-photonics wafer-scale fabrication process and results discussed in Sec. 2.2.2.

The following work was done in collaboration with Thomas Dyer (SUNY Poly), Manan Raval (MIT), Christopher Baiocco (SUNY Poly), Andres Garcia Coleto (MIT), Ashton Hattori (MIT), Kevin Fealey (SUNY Poly), Seth Kruger (SUNY Poly), Michael Watts (MIT), and Jelena Notaros (MIT). This work has been published in [61, 62].

2.1 Integrated Visible-Light Silicon-Photonics Platform and Wafer-Scale Fabrication Process

The silicon-photonic devices and systems discussed in this work were fabricated in a CMOS-compatible 300-mm wafer-scale silicon-photonics process at the State University of New York Polytechnic Institute's (SUNY Poly) Albany NanoTech Complex. The developed photonics platform consists of five silicon-nitride (Si_3N_4) layers, a metal layer for electrical routing and contact pads, a trench layer for holding liquid crystal, and a dicing trench for fiber coupling.

In the platform, the devices and systems were fabricated on a 300-mm-diameter silicon handle wafer covered with a 2-µm-thick silicon-dioxide (SiO_2) layer. A cross-sectional diagram of the platform stack is shown in Fig. 2.1.

First, a Si_3N_4 layer was deposited on top of the buried silicon-dioxide layer using a plasma-enhanced-chemical-vapor-deposition (PECVD) process. The deposited silicon nitride was subsequently polished by a chemical-mechanical planarization (CMP) step to reduce optical scattering loss, resulting in a final layer thickness of 60 nm. The silicon-nitride layer was finally patterned using 193-nm immersion lithography and dry etching. A tetraethylorthosilicate (TEOS) PECVD SiO_2 layer was then deposited on top of the Si_3N_4 layer and its top surface was planarized using a CMP step, leaving 50 nm of SiO_2 above the Si_3N_4 layer. This waveguide formation process was then

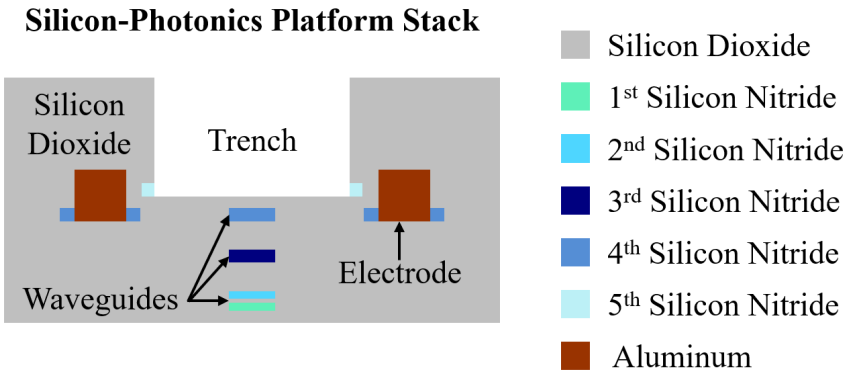

Figure 2.1: Simplified cross-sectional diagram of the platform stack, showing the five silicon-nitride layers, the metal layer, and the silicon-dioxide trench (not to scale).

repeated four times, for a second 60-nm-thick Si_3N_4 layer with a 250-nm-thick SiO_2 layer on top, a third 160-nm-thick Si_3N_4 layer with a 250-nm-thick SiO_2 layer on top, a fourth 160-nm-thick Si_3N_4 layer with a 60-nm-thick SiO_2 layer on top, and a fifth 160-nm-thick Si_3N_4 layer with a 640-nm-thick SiO_2 layer on top. The first, second, and third Si_3N_4 layers are used as waveguiding layers to route the light on the chip, the fourth Si_3N_4 layer is used as both a waveguiding layer to route the light and an etch-stop layer for the integrated metal electrodes, and the fifth Si_3N_4 layer serves as an etch stop for the silicon-dioxide trench.

Next, a trench was formed in the SiO_2 cladding above the waveguide in the fourth Si_3N_4 layer. This trench was etched 800 nm deep into the SiO_2 using the fifth Si_3N_4 layer as an etch stop. The Si_3N_4 etch stop was then dry etched selectively to the underlying silicon dioxide.

A metal layer was then formed by etching a 1020-nm-deep trench into the SiO_2 cladding using the fourth Si_3N_4 layer as an etch stop, and filling the trench with 820-nm-thick aluminum using a metal deposition process followed by an aluminum CMP step and a subsequent deposition of a 200-nm-thick SiO_2 cap using the TEOS PECVD process. This metal layer is used for routing of electronic signals and definition of pads for electronic probe connection.

Finally, the silicon dioxide above each metal pad was removed to create an opening for each pad to permit electrical contact with a probe, and a deep dicing trench was

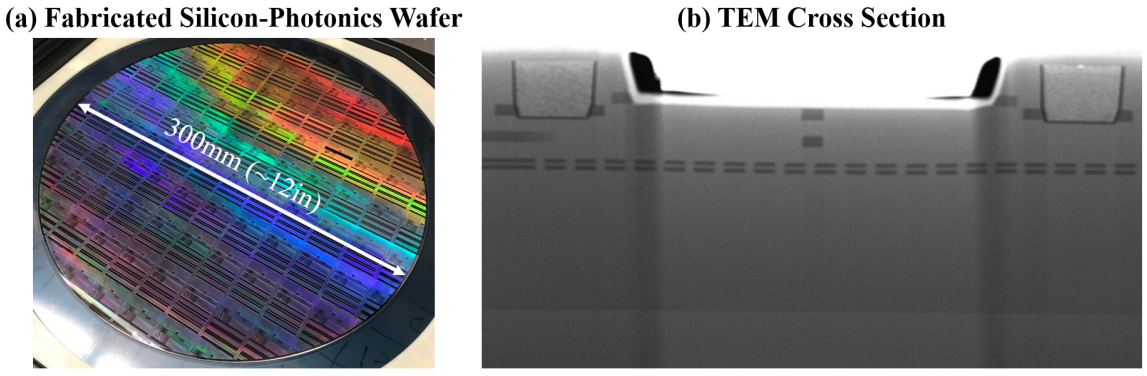

Figure 2.2: (a) Photograph of a fabricated 300-mm-diameter silicon-photonics wafer. (b) Transmission-electron-microscopy cross-sectional image showing the fabricated layers (TEM image taken by SUNY Poly).

etched to define the edge of each chip and create a smooth facet for fiber edge coupling to the chip after dicing.

A photograph of an example final fabricated wafer is shown in Fig. 2.2a and a transmission-electron-microscopy cross-sectional image showing the fabricated layers is shown in Fig. 2.2b.

2.2 Wafer-Scale Transfer Process to Unique Substrates

The field of silicon photonics has advanced rapidly due to wafer-scale fabrication, with silicon-photonics platforms and fabrication processes being demonstrated at both infrared [63,64] and visible [1,17,65] wavelengths. However, these demonstrations have focused on fabrication processes on silicon substrates that result in rigid and opaque photonic wafers and chips, which limit the application space. There are many application areas that would benefit from transparent or flexible silicon-photonics wafers, such as pliable or augmented-reality displays and wearable healthcare monitors that conform to the body [66,67].

In this work, we develop a novel 300-mm wafer-scale CMOS-compatible platform and fabrication process for transferring photonic layers to unique substrates to enable transparent and flexible silicon-photonics wafers. The silicon-photonics platform and CMOS-compatible 300-mm wafer-scale silicon-photonics fabrication process were developed at the State University of New York Polytechnic Institute's (SUNY Poly) Albany NanoTech Complex.

A simplified outline of the fabrication steps for transferring photonics layers to a unique substrate are shown in Fig. 2.3. The general fabrication process consists of 5 steps. First, the photonic and electronic layers are fabricated on a 300-mm-diameter silicon handle wafer covered with a 2-μm-thick silicon-dioxide (SiO_2) layer, as depicted in Fig. 2.3a. This photonic and electronic fabrication process is discussed in Sec. 2.1. Second, a silicon handle wafer is temporarily adhesive bonded to the top of the SiO_2 layer, as depicted in Fig. 2.3b. Third, the wafer is flipped over, and the original silicon layer is thinned down, as shown in Fig. 2.3c. Fourth, a unique substrate is bonded

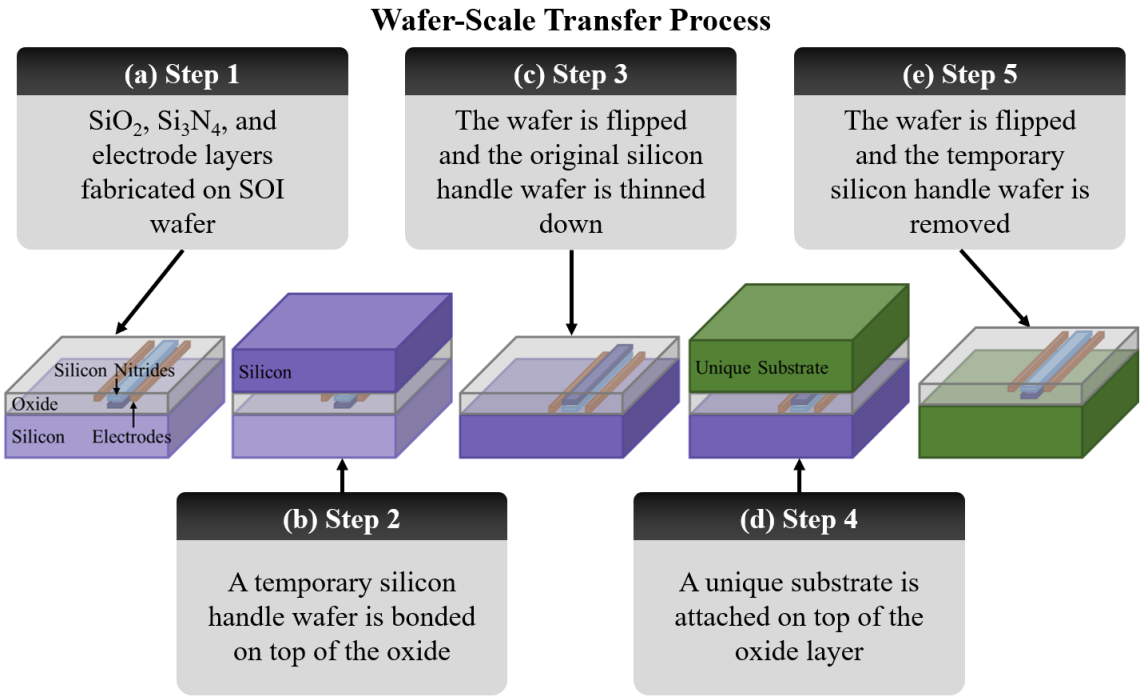

Figure 2.3: Simplified outline of fabrication steps to transfer photonics layers to a unique substrate.

to the top of the silicon-dioxide layer, as shown in Fig. 2.3d. Finally, the wafer is flipped back over, and the temporary silicon handle wafer is removed, as depicted in Fig. 2.3e.

2.2.1 Transparent Wafer-Scale Silicon-Photonics Fabrication

To enable fabrication of the VIPER display (discussed in Sec. 1.3), a first-of-its-kind custom wafer-scale fabrication process that transfers the photonics layers from a traditional opaque silicon substrate (Fig. 2.2a) to a transparent glass wafer was developed.

The transfer process outlined in Fig. 2.3 is used to fabricate a transparent silicon-photonics wafer, where the unique substrate is a glass wafer. A resulting fabricated transparent silicon-photonics wafer is shown in Fig. 2.4a. A photograph of a gel pack with a traditional silicon-photonics chip (with a traditional silicon handle wafer) and a transparent silicon-photonics chip (with the unique glass wafer backplane) is shown in Fig. 2.4b. This fabrication process enables a highly discreet and transparent

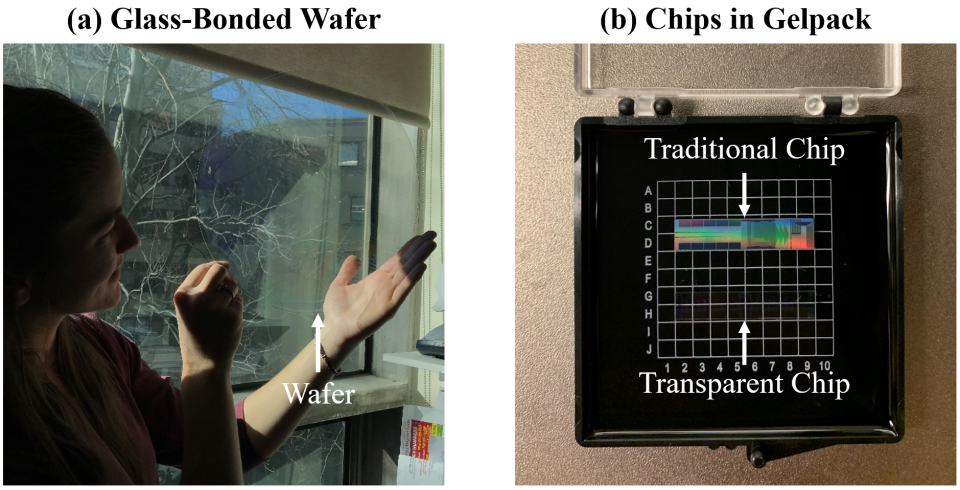

Figure 2.4: Photographs showing (a) a 300-mm-diameter glass-bonded VIPER wafer and (b) a traditional opaque photonic chip and a transparent glass-bonded VIPER chip in a gel pack.

augmented-reality system. This transparent platform enables the VIPER chip to sit directly in front of the user's eye, as shown in Fig. 1.7, to enable a direct-view near-eye display approach, as shown in Fig. 1.8.

2.2.2 Flexible Wafer-Scale Silicon-Photonics Fabrication

The transfer process outlined in Fig. 2.3 is then used to fabricate a flexible silicon-photonics wafer, where the unique substrate is flexible. A simplified outline of the fabrication steps for transferring photonics layers to a flexible substrate are shown in Fig. 2.5.

Photographs of a fabricated flexible silicon-photonics wafer are shown in Fig. 2.6.

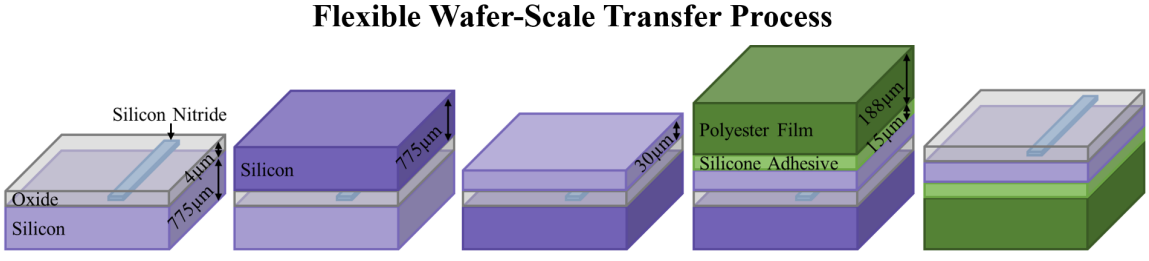

Figure 2.5: Simplified outline of fabrication steps to transfer photonics layers to a flexible substrate.

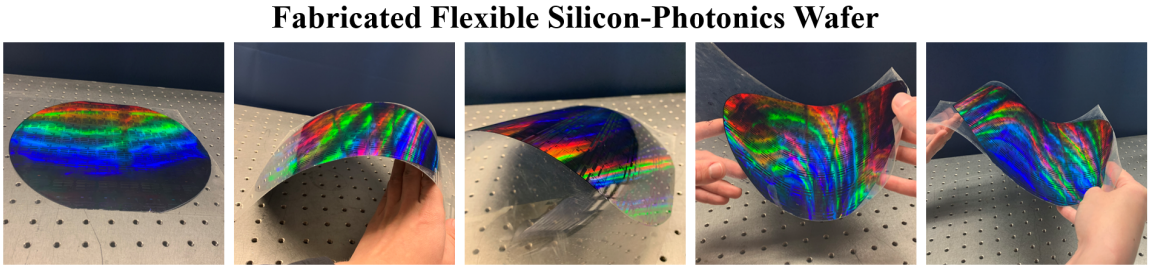

Figure 2.6: Photographs of a fabricated flexible silicon-photonics wafer, lying flat, bent convexly, bent concavely, and bent in a wave.

Photographs of the dicing tool and process for dicing the fabricated flexible silicon-photonics wafer to individual flexible photonic chips are shown in Fig. 2.7.

To experimentally characterize the flexible photonic chips, the output from a 632.8-nm-wavelength helium-neon laser was coupled on chip via a tapered fiber-to-chip edge coupler and the output light was coupled off chip via another edge coupler to a fiber that was routed to a power meter, as shown in Fig. 2.8a. The coupling loss of these tapered fiber-to-chip edge couplers was empirically determined to be approximately 8 dB/facet, which was limited by the facet roughness introduced during the dicing process.

Waveguide loss was experimentally characterized using paperclip loss test struc-

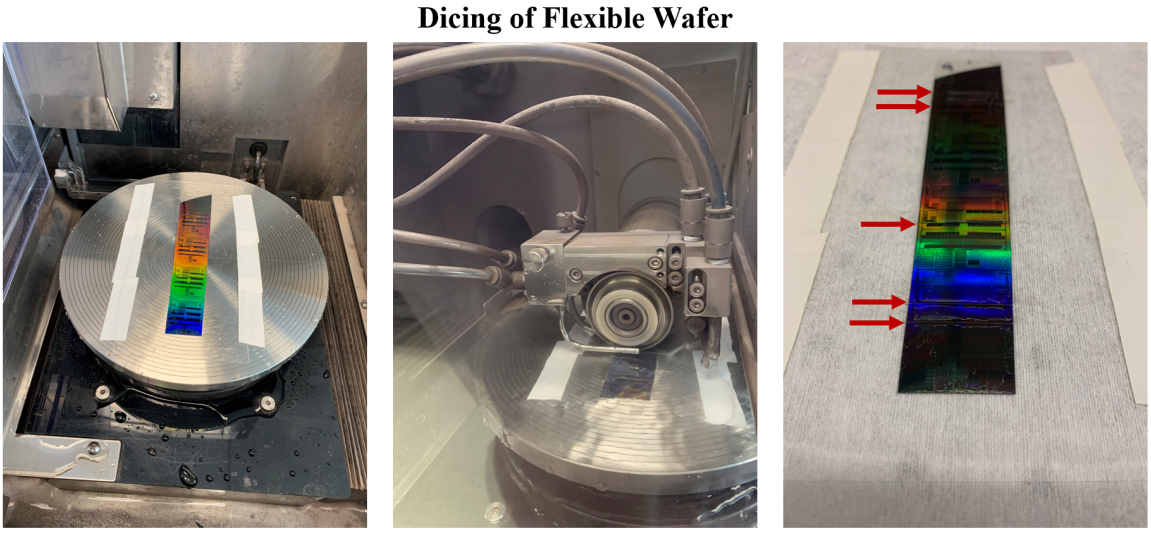

Figure 2.7: Photographs of a section of a fabricated flexible silicon-photonics wafer undergoing dicing into individual flexible photonic chips, highlighting the resulting dicing cuts.

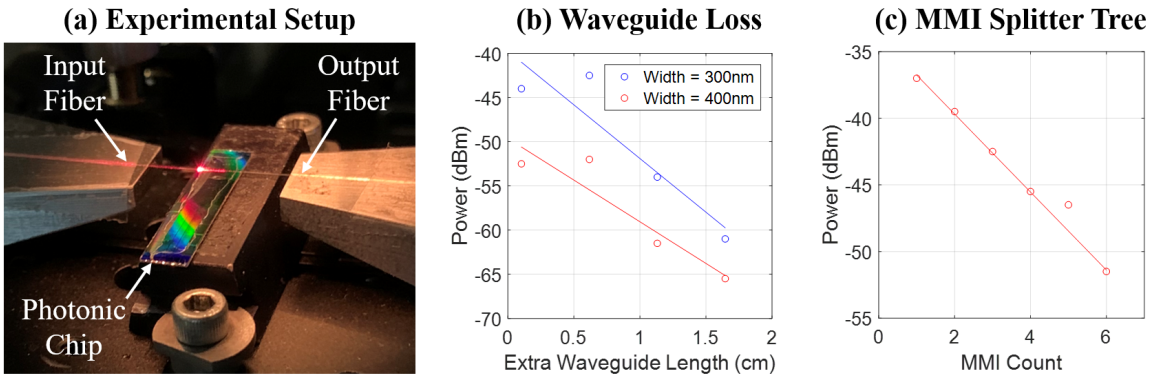

Figure 2.8: (a) Photograph of the experimental setup. (b) Waveguide loss for two different waveguide widths, measured using paperclip test structures. (c) Measured power through a multi-mode interferometer splitter tree.

tures with four varying waveguide lengths and two waveguide widths. The measured propagation losses for 300-nm-wide and 400-nm-wide waveguides were 12.1 dB/cm and 9.4 dB/cm, respectively, as shown in Fig. 2.8b. Note that a waveguide in this platform fabricated on a traditional silicon-photonics wafer has propagation losses of approximately 6 dB/cm. The higher measured losses for the flexible photonic chip can be attributed to the waveguide fabrication process, which did not include processing for line-edge-roughness optimization, which helps reduce propagation loss.

To demonstrate a more complex device and characterize chip-scale fabrication variation, a six-stage splitter tree consisting of 1x2 multi-mode interferometer (MMI) splitters was experimentally measured, and the splitting ratio for a single MMI was calculated to be -2.9 dB, as shown in Fig. 2.8c, closely matching the ratio expected from simulation.

We then performed bend durability testing on the fabricated flexible photonic chips to test how well the chips withstand being bent at set angles. Photographs of a flexible photonic chip undergoing this bend durability testing is shown in Fig. 2.9, showing that we hold down one end of the photonic chip against a cylinder and then we apply pressure to the other end of the photonic chip to bend it around the cylinder. We use five cylinders of various diameters to test various bending angles, as shown in Fig. 2.10.

We perform the bend durability testing for the five cylinders on a fabricated

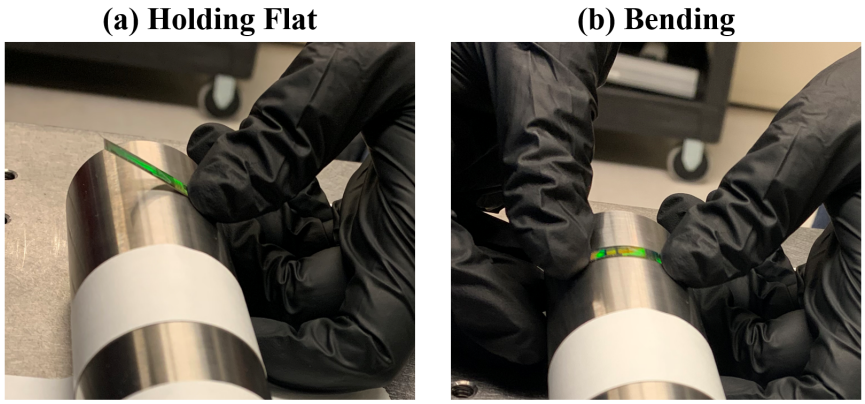

Figure 2.9: Photographs of a flexible photonic chip undergoing bend durability testing, showing the chip (a) held flat against and (b) bent around a cylinder.

flexible photonic chip. Results of optical power coupled through the chip after it is bent up to 500 times around each of the five cylinders of various diameters are shown in Fig. 2.11. The chip maintains good optical performance up to being bent 2000 times down to a bend diameter of 0.5". Only when the chip is bent down to an aggressive diameter of 0.25" does the optical performance significantly degrade.

We developed a 300-mm wafer-scale CMOS-compatible flexible platform and fabrication process, and experimentally demonstrated key functionality at visible wavelengths, including chip coupling, waveguide routing, passive devices, and bend durability testing. This work paves the way for future demonstrations in flexible silicon

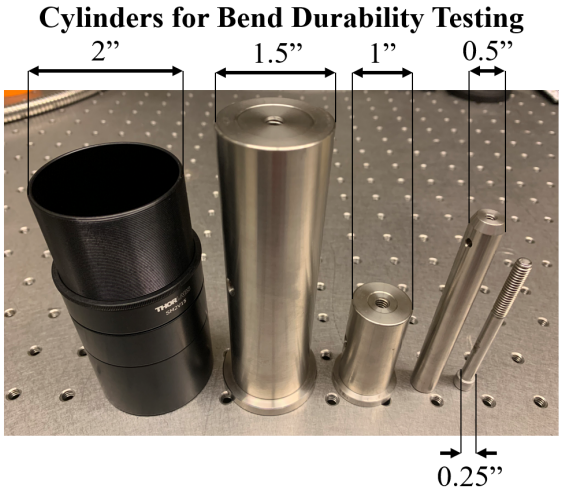

Figure 2.10: Photograph of five cylinders of various diameters used for bend durability testing. Diameters ranging from 0.25" to 2".

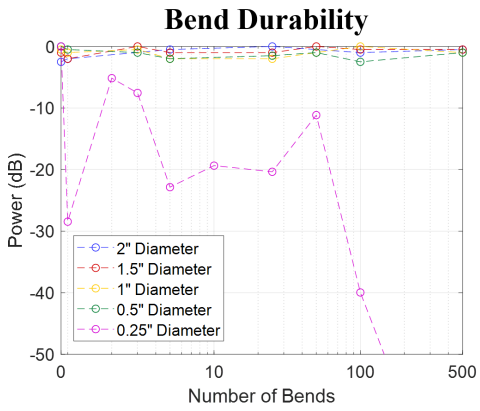

Figure 2.11: Results showing normalized optical power through a flexible chip after it undergoes up to 500 bends for each cylinder, of diameters ranging from 0.25" to 2".

photonics and opens the door to expanded applications, including wearable healthcare monitors that conform to the body and pliable displays [66, 67].

2.3 Conclusion

In this chapter, we developed a visible-light silicon-photonics platform and wafer-scale fabrication process. Then, we developed a wafer-scale transfer process to transfer photonic layers from rigid and opaque silicon handle wafers to unique substrates. Next, we developed a transparent platform and wafer-scale fabrication process. We demonstrated fabricated transparent silicon-photonics wafers and chips. Finally, we developed a wafer-scale flexible platform and wafer-scale fabrication process. We demonstrated fabricated flexible silicon-photonics wafers and chips, and performed optical characterization and bend durability studies. This platform and wafer-scale fabrication process for photonics wafers that are transparent or flexible opens the door for the field of silicon photonics to new application areas.

Chapter 3

Large-Scale Passive VIPER Display

As a first proof-of-concept demonstration, a large-scale passive version of the VIPER display was designed, fabricated, and experimentally demonstrated. In Sec. 3.1, the passive pixel-based architecture is developed and described. The overall architecture of the 2D grid of pixels is described, as well as the architecture of a single passive pixel, which is the building block for the display. In Sec. 3.2, the encoding procedure for determining absolute phase, amplitude, and phase gradient for each pixel in the passive VIPER display is described. In Sec. 3.3, a large-scale passive VIPER display is fabricated and experimentally demonstrated to emit a static image of a wire-frame cube.

The following work was done in collaboration with Manan Raval (MIT), Thomas Dyer (SUNY Polytechnic), Christopher Baiocco (SUNY Polytechnic), Michael R. Watts (MIT), and Jelena Notaros (MIT). This work has been published in [1].

3.1 Passive VIPER Display Architecture

The passive VIPER display is based on a 2D grid of coherent visible-light integrated optical phased arrays that act as the pixels in the display. A top-view schematic of the passive VIPER display is shown in Fig. 3.1.

At the input of the system, an on-chip inverse-taper edge coupler couples light from an off-chip laser into an on-chip single-mode silicon-nitride waveguide. A 5-

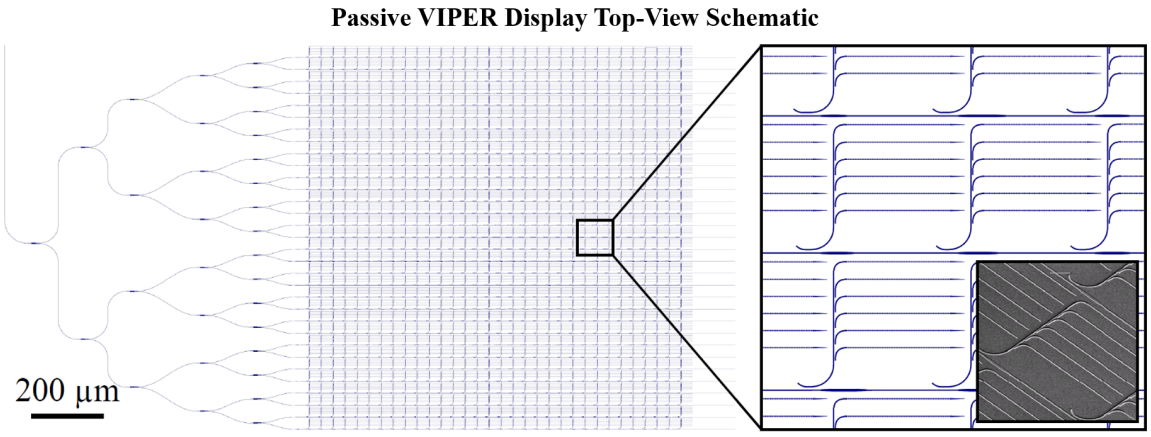

Figure 3.1: Schematic of the passive VIPER display with 32×32 pixels, 32 μm pixel pitch, 6 antennas per a pixel, and 4 μm antenna pitch (with SEM shown in inset).

stage multi-mode-interference splitter tree evenly distributes the input power from the single input waveguide to 32 rows. These rows have a final pitch of 32 μm. Along each row, 32 compact optical-phased-array-based pixels are cascaded with a pixel pitch of 32 μm for a total of 1024 pixels in the display.

A top-view schematic of a single passive VIPER optical-phased-array-based pixel is shown in Fig. 3.2. Each pixel consists of (1) a phase taper structure [54] on the row waveguide to encode the *absolute phase* of the light emitted by each pixel, (2) an evanescent tap to couple light from the row waveguide to the pixel bus based on the desired pixel *amplitude* encoding, and (3) evanescent taps with increasing

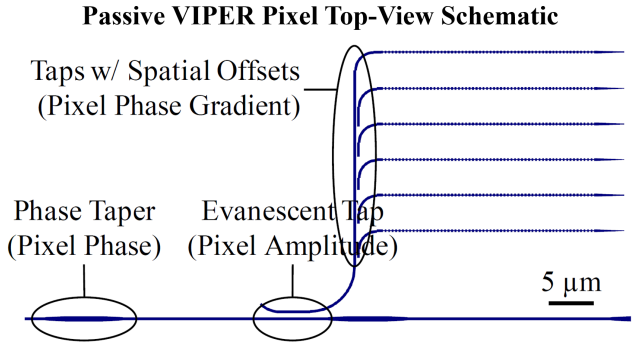

Figure 3.2: Schematic of a single optical-phased-array-based pixel of the passive VIPER display showing the phase taper for pixel absolute phase encoding, evanescent tap for pixel amplitude encoding, and pixel-to-antenna taps with varying spatial offsets for pixel phase gradient encoding.

coupling lengths to uniformly distribute light from the pixel bus to 6 grating-based antennas [68] with spatial offsets [2] to enable a linear *phase gradient* encoding for each pixel.

3.2 Passive VIPER Display Encoding

To generate an example virtual image of a wire-frame cube using the passive VIPER display, a holographic encoding procedure was used to determine the absolute phase, amplitude, and phase gradient encodings for each pixel. In general, to generate a holographic image using a display, the amplitude and phase distributions necessary for generating the desired image on the retinal plane must be reproduced in the plane of the display.

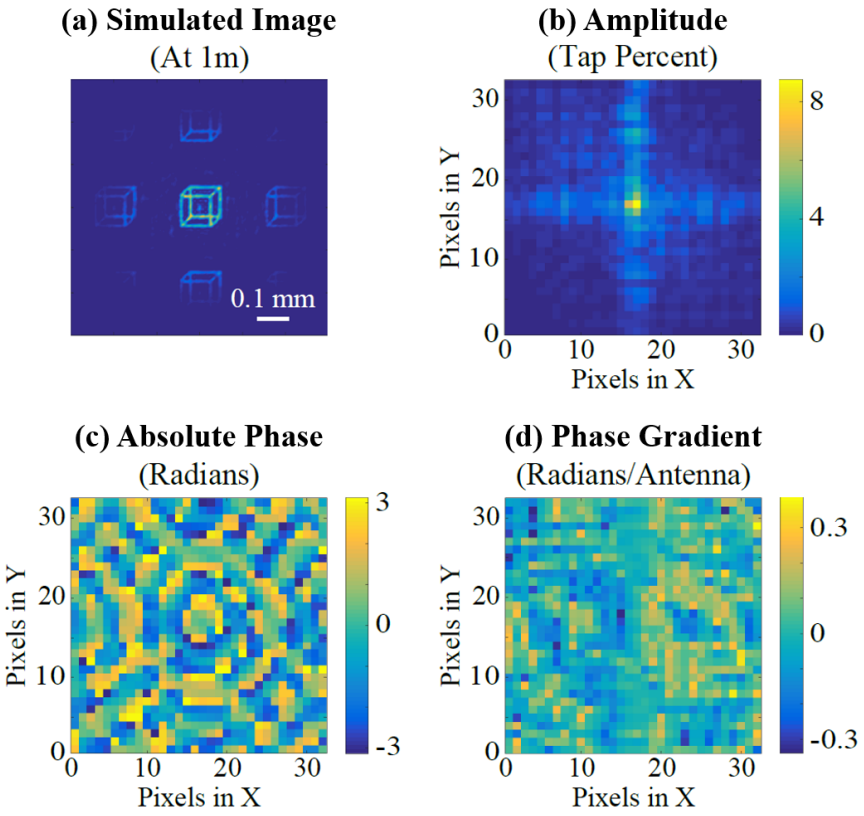

Figure 3.3: (a) Simulation of the virtual image projected by the passive VIPER display and corresponding (b) amplitude, (c) absolute phase, and (d) phase gradient encodings, assuming a 632.8-nm operating wavelength, 1-m virtual object distance, 20-mm human-eye focal length, and 12-mm eye relief.

Specifically, for the VIPER display, these phase and amplitude distributions were closely approximated by discretizing the distributions into local one-dimensional phase gradients with arbitrary amplitudes and absolute phases corresponding to the size of the pixels in the display. These discretized distributions were then iteratively optimized using the Gerchberg-Saxton algorithm [55, 69, 70] to accurately generate the desired virtual holographic image. The resulting image and corresponding amplitude, absolute phase, and phase gradient encodings – simulated assuming a 632.8-nm operating wavelength, 1-m virtual-object distance, 12-mm eye relief, and 20-mm human-eye focal length – are shown in Figs. 3.3a–d. Further details on the implemented algorithm are provided in [1, 71].

3.3 Passive VIPER Display Experimental Setup and Results

This large-scale passive VIPER display was then fabricated in a custom 300-mm-diameter wafer-scale silicon-photonics process at the SUNY Poly Albany NanoTech Complex. This developed process is based on silicon-nitride waveguides, since silicon nitride has a low absorption coefficient within the visible spectrum and is CMOS compatible. The platform for the passive VIPER display consists of a single silicon-nitride waveguiding layer with a silicon-dioxide cladding and a dicing trench for fiber coupling, which were fabricated using a combination of plasma-enhanced-chemical-vapor-deposition, chemical-mechanical-planarization, 193-nm-immersion-lithography, and dry-etching processes (as discussed in detail in Sec. 2.1). A micrograph of a fabricated large-scale passive VIPER display is shown in Fig. 3.4. The micrograph shows the MMI splitter tree network and the 1024 optical-phased-array-based pixels.

To characterize the fabricated passive VIPER display, a 632.8-nm-wavelength helium-neon laser was coupled onto the chip and an optical imaging system, consisting of a 20-mm-focal-length lens and a visible-light camera, was used to emulate the functionality of the human eye (photographs of the fabricated chip and experi-

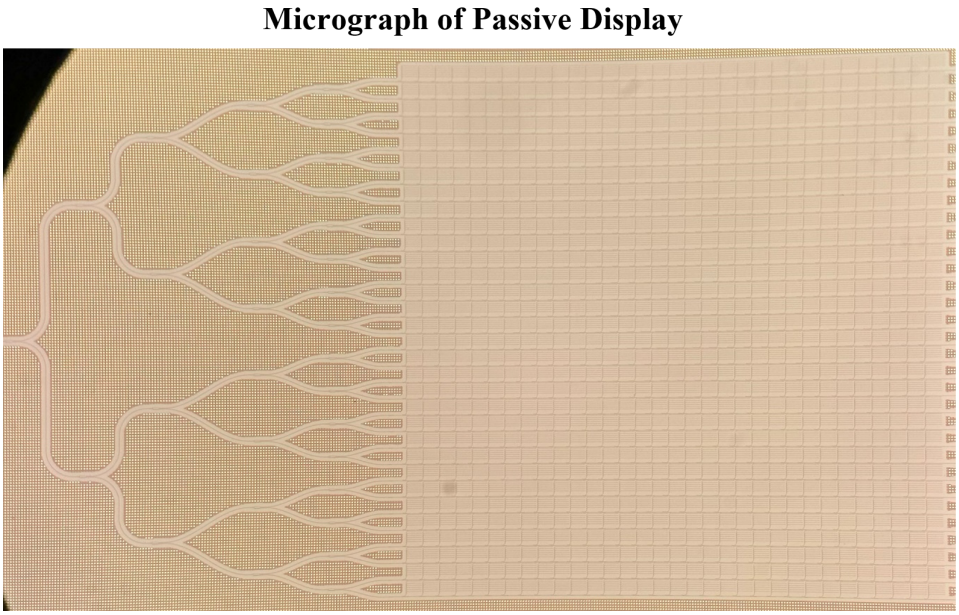

Figure 3.4: Micrograph of a fabricated passive VIPER display, showing input waveguide, MMI splitter tree network, and 1024 optical-phased-array-based pixels.

mental setup are shown in Figs. 3.5a–b).

As expected, the display generates the desired wire-frame image at a single focal plane with a virtual object distance around 1 m and an emulated eye relief around 12 mm, as shown in Fig. 3.6.

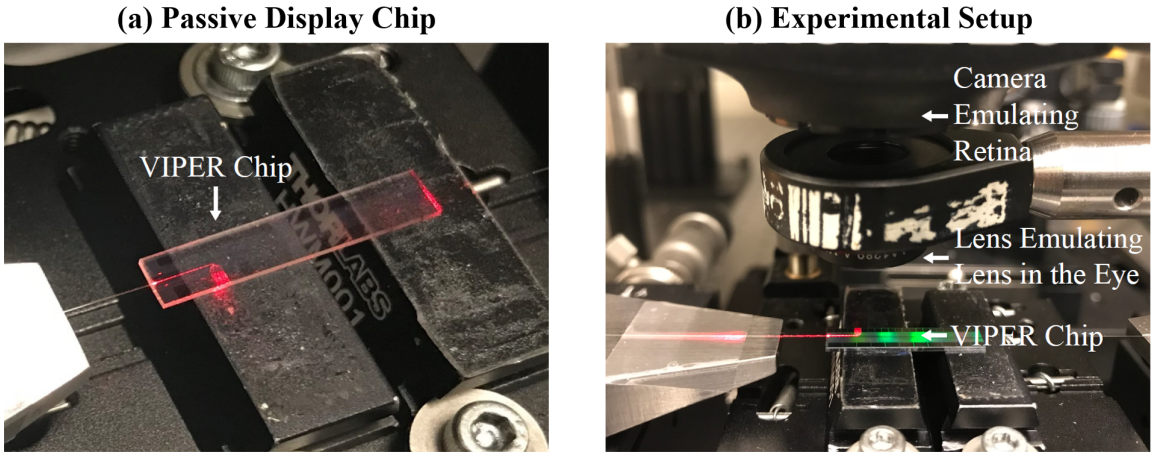

Figure 3.5: Photograph of (a) the transparent VIPER display chip and (b) the experimental characterization setup showing the input optical fiber, photonic chip, lens emulating the lens in the eye, and camera emulating the retina.

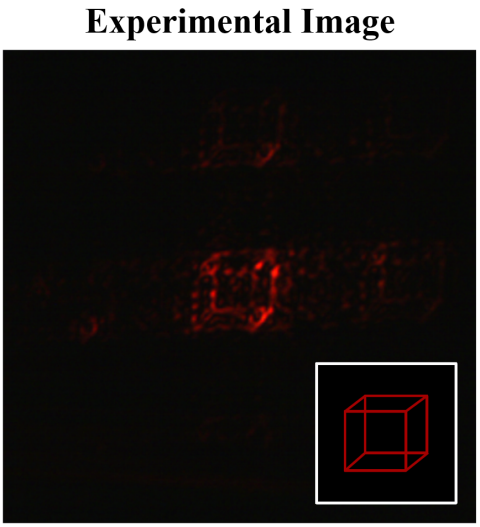

Figure 3.6: Experimental measurement of the virtual image of a wire-framed cube projected by the passive VIPER display with an approximately 1-m virtual-object distance, 20-mm-focal-length lens, and 12-mm eye relief (with expected image shown in inset).

3.4 Conclusion

This large-scale passive VIPER display demonstration represents an important step towards developing the full VIPER display, successfully confirming the optical-phased-array-based approach, the holographic encoding methodology, and the transparent wafer-scale fabrication process.

Chapter 4

Liquid-Crystal Theory, Integration, and Packaging

In Ch. 3, a large-scale passive VIPER display was demonstrated; however, for a practical augmented-reality display, it must be able to generate changing images, or videos. To achieve this, the passive components used in the passive display need to be replaced with actively tunable modulators. We achieve this with integrated liquid-crystal-based modulators.

In this chapter, we motivate why we integrate liquid crystal into the silicon-photonics platform in Sec. 4.1. Then, we provide some relevant background theory on liquid-crystal media in Sec. 4.2. Next, we describe how the liquid-crystal media operates within our integrated platform in Sec. 4.3. Finally, we outline the packaging process for integrating the liquid-crystal media into our silicon-photonics platform, describing the process steps and highlighting useful techniques for evaluating the success of the packaging process, in Sec. 4.4.

The following work was done in collaboration with Manan Raval (MIT), Andres G. Coleto (MIT), Thomas Dyer (SUNY Polytechnic), Christopher Baiocco (SUNY Polytechnic), Michael R. Watts (MIT), and Jelena Notaros (MIT). This work has been published in [61, 72, 73].

4.1 Motivation for Liquid-Crystal Integration

Traditionally, silicon has been used as the waveguiding medium in integrated photonics, since it is the foundation of mature CMOS fabrication processes, it enables high index contrast for compact devices, and it is relatively easy to modulate; however, silicon absorbs visible wavelengths. As such, visible-light integrated systems have generally been based on silicon-nitride waveguides, since silicon nitride has a low absorption coefficient within the visible spectrum and is CMOS compatible. Although silicon nitride has the benefit of transparency in the visible wavelength range, it has a low thermo-optic coefficient and does not exhibit significant electro-optic properties, which has made integrated phase modulation at visible wavelengths a challenge. Typical silicon-nitride phase modulators based on heaters are on the order of hundreds of microns to several millimeters long and use excessive power [59, 74–77], which places unreasonable constraints on many systems and applications. As such, compact and low-power integrated silicon-nitride modulators are an important advancement for the field.

As a solution to the challenge of compact and low-power integrated visible-light modulation, nematic liquid crystal (LC), with strong birefringence at optical wavelengths, can be integrated into photonic platforms and used to manipulate the mode in photonic waveguides to induce a tunable phase shift or amplitude modulation. Integrated liquid-crystal-based devices, including rectangular-waveguide phase shifters [78, 79], slot-waveguide phase shifters [80, 81], and ring resonators [82–89], have been explored (Fig. 4.1). However, these prior liquid-crystal-device demonstrations have been largely limited to silicon waveguides and operation within the infrared wavelength range. Here, we integrated liquid crystal into our visible-light silicon-nitride-based silicon-photonics platform to enable compact and efficient modulators.

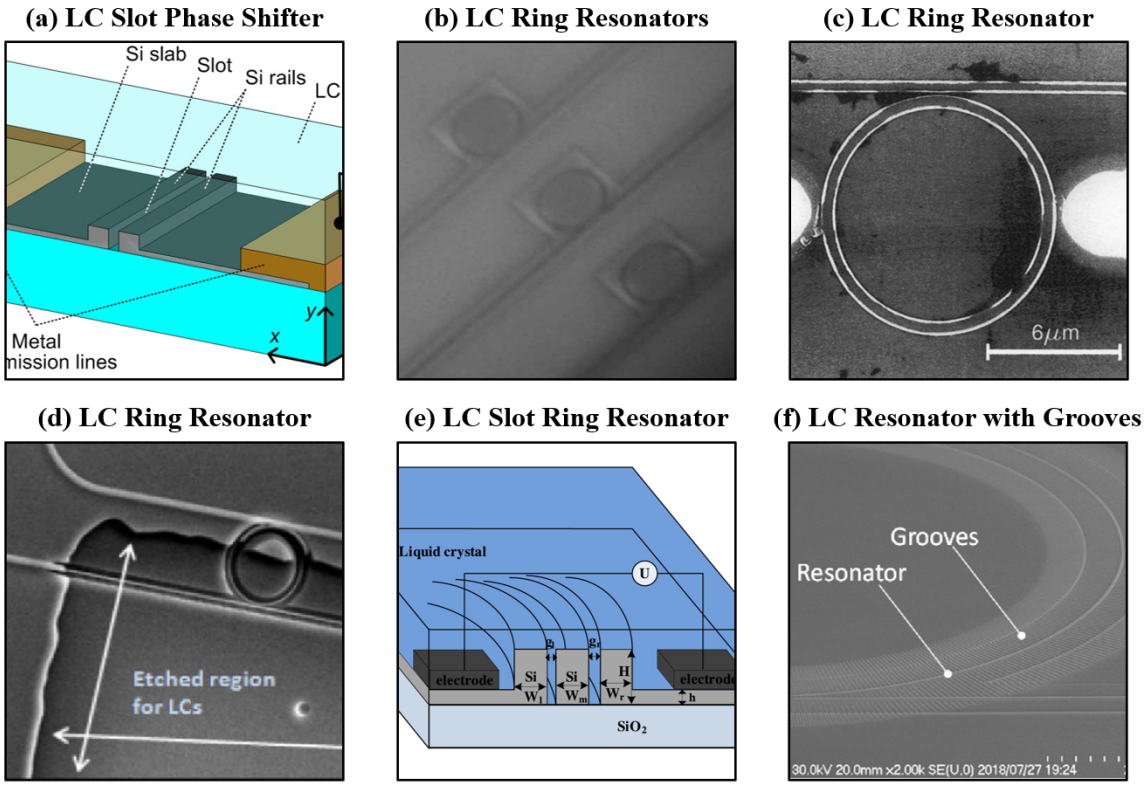

Figure 4.1: (a) Liquid-crystal-based slot-waveguide phase shifter (figure from [81]). (b–d) Liquid-crystal-clad ring resonators (figures from [83,86,87]). (e) Liquid-crystal-based double-slot ring resonator (figure from [89]). (f) Liquid-crystal-based ring resonator with alignment grooves (figure from [79]).

4.2 Liquid-Crystal Background Theory and Operation

Liquid crystal has many unique properties [90–95], which makes it of interest for integrated visible-light devices. One such property is that liquid crystal has an anisotropic index of refraction. This anisotropy is due to the fact that a liquid-crystal molecule has an ordinary and an extraordinary axis, as shown in Fig. 4.2a, and there is a strong birefringence between these two axes in the visible wavelength range. Light propagating in a direction parallel to the liquid-crystal director (shown in Fig. 4.2a) sees the ordinary index of refraction, n_o, while light propagating perpendicular to the liquid-crystal director sees the extraordinary index of refraction, n_e.

The birefringent property of liquid crystal allows for the manipulation of propa-

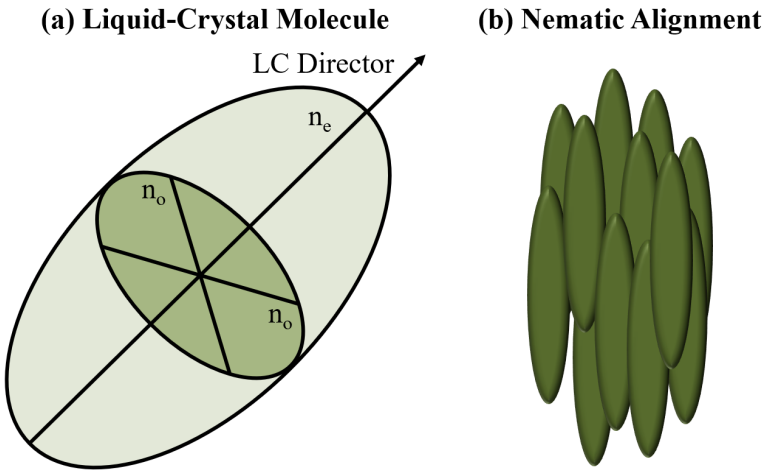

Figure 4.2: (a) Ordinary and extraordinary axes of a liquid-crystal molecule. (b) 1-dimensional alignment of nematic liquid-crystal molecules.

gating light; however, the orientation of the liquid-crystal director with respect to the propagation direction of the light must be known in order to achieve the desired results. A second unique property that allows for the director orientation to be known, is that, although liquid crystal is indeed a liquid, the molecules can be aligned in a crystalline fashion [96]. In a nematic liquid crystal, the molecules align in one dimension, in the direction parallel to the directors, as shown in Fig. 4.2b. Furthermore, in the presence of an alignment structure, such as a rubbed polyimide layer, the liquid-crystal molecules mechanically anchor to the alignment layer. Hence, the alignment of the liquid-crystal directors can be intentionally set to a desired direction.

Furthermore, not only can the liquid-crystal director be anchored in an initial direction via a mechanical alignment layer and the nematic property of the molecules themselves, but the molecules can be dynamically rotated. This rotation can be achieved via a third unique property, which is that liquid-crystal molecules align to an external electric field. Fig. 4.3a shows the liquid-crystal molecules initially anchored via a mechanical alignment layer, when no external electric field is applied across the region. Fig. 4.3b shows the liquid-crystal molecules beginning to align to an applied electric field, once the field strength is increased past a threshold to be great enough to overcome the mechanical anchoring strength. Fig. 4.3c shows the liquid-crystal molecules fully aligned to an external electric field (note that the molecules close to

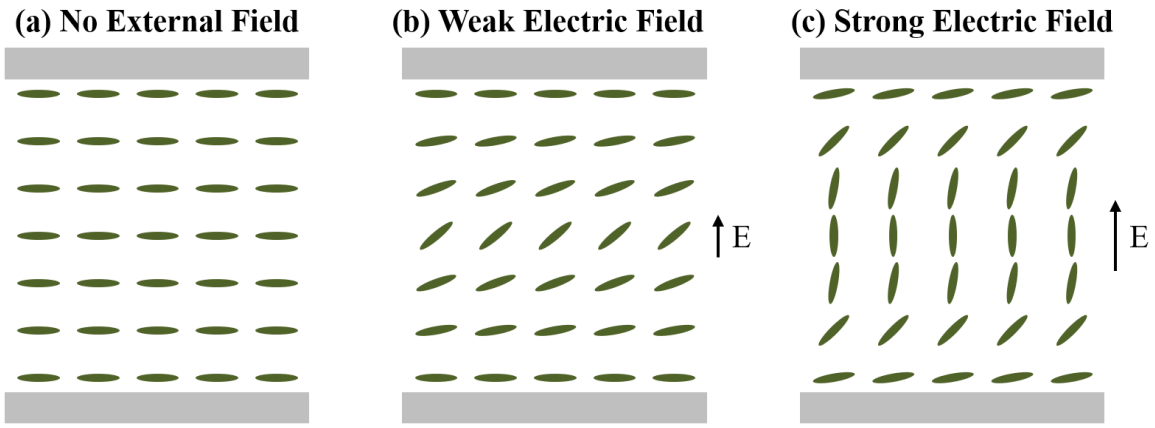

Figure 4.3: Liquid-crystal molecule alignment with (a) no external electric field, (b) an external electric field exceeding the required threshold to overcome the mechanical anchoring strength, and (c) an external electric field strong enough to completely rotate the molecules.

the alignment layer remain more strongly anchored than molecules farther away). When the external electric field is removed, the molecules revert back to their initial anchored state. In this way, the liquid-crystal molecules can be dynamically rotated to take advantage of the birefringence and vary the index of refraction with respect to light propagating in a set direction.

4.3 Liquid-Crystal Integration

The useful properties of liquid crystal can be leveraged in an integrated-photonics platform. In this platform, a silicon-nitride waveguide is recessed in a silicon-dioxide cladding, which confines and guides the light on the chip. As shown in Fig. 4.4a, the fundamental mode in the waveguide is fairly well confined in the silicon nitride. Then, a trench is made into the silicon-dioxide cladding above the waveguide and the trench is filled with liquid crystal. Now, the silicon-nitride waveguide is still recessed within a silicon-dioxide cladding, but a liquid-crystal region sits on top of the waveguide, as shown in Fig. 4.4b–d. The mode in the waveguide is impacted by the liquid crystal and the mode is slightly pulled up into the liquid-crystal region. Furthermore, the mode in the waveguide varies based on the refractive index of the liquid-crystal region. The mode varies in two ways; the effective index of the mode changes and the mode

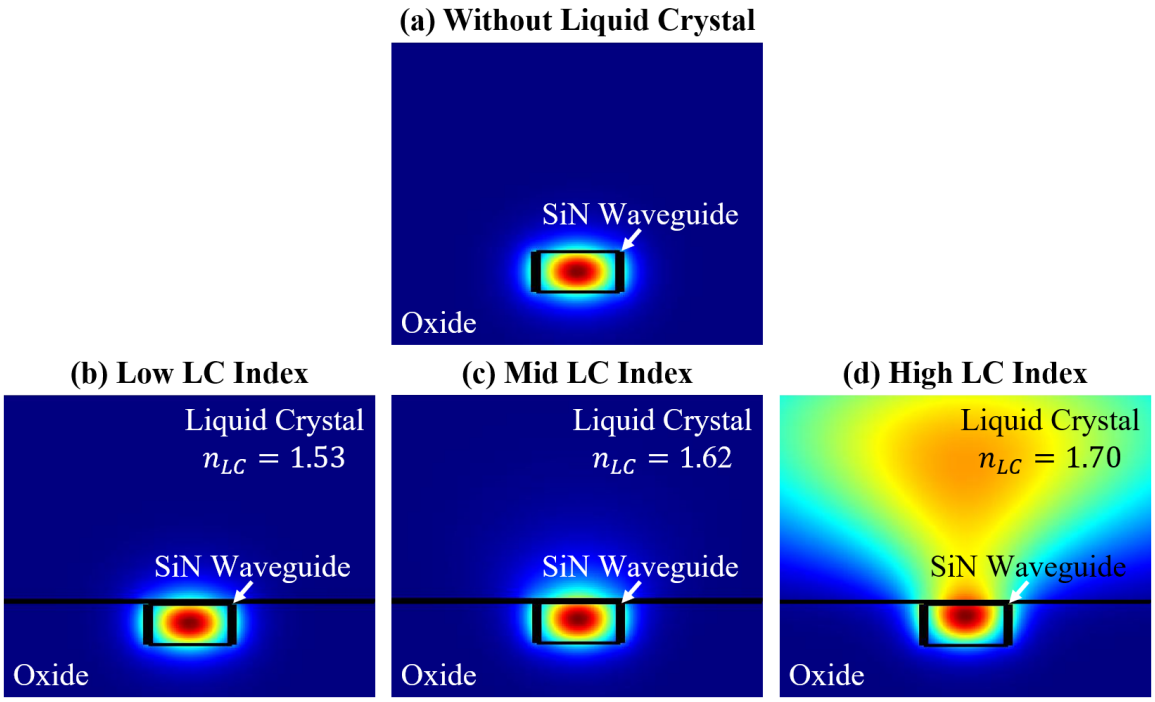

Figure 4.4: Fundamental mode of a silicon-nitride waveguide recessed within a silicon-dioxide cladding (a) with no liquid crystal and (b) with a liquid-crystal region of refractive index $n_{LC} = 1.53$, (c) $n_{LC} = 1.62$, and (d) $n_{LC} = 1.70$.

shape gets pulled up farther into the liquid-crystal region as the effective index of the liquid crystal is increased, as shown in Fig. 4.4b–d. The liquid crystal used here is 5CB, which has an ordinary refractive index of 1.53 and an extraordinary refractive index of 1.7 [97,98]. However, because the mode becomes less confined as the liquid-crystal index increases, the loss also increases, so the refractive index is limited to maintain a practical amount of loss.

As stated above, the liquid-crystal molecules align to an external electric field. In this integrated platform, an electric field is applied across the liquid-crystal region via metal electrodes on each side of the trench, as shown in Fig. 4.5a. A voltage is applied across these integrated electrodes to induce an electric field across the liquid-crystal region. The electrodes run alongside the entire length of the liquid-crystal-filled trench, as shown in Fig. 4.5b, to uniformly vary the refractive index throughout the entire length. Note that the electric field varies vertically throughout the liquid-crystal region; however, the region of interest that largely affects modulation is directly above

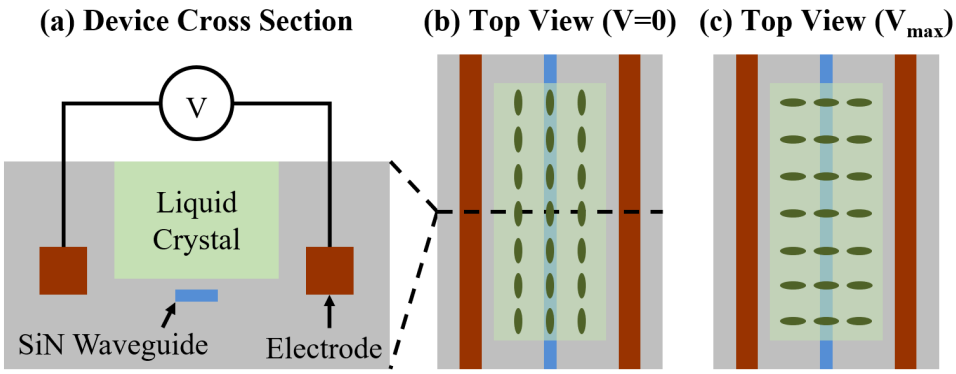

Figure 4.5: (a) Simplified cross-sectional diagram of liquid crystal integrated into our silicon-photonics platform, showing the silicon-nitride waveguide recessed within silicon dioxide below a liquid-crystal-filled trench with integrated electrodes on each side (not to scale). (b) Simplified top-view schematic of the modulation region when no voltage is applied across the liquid-crystal region, resulting in parallel alignment of the liquid-crystal molecules with respect to the waveguide (not to scale). (c) Simplified top-view schematic of the modulation region when the maximum voltage is applied across the liquid-crystal region, cresulting in complete rotation of the liquid-crystal molecules and perpendicular alignment of the molecules with respect to the waveguide (not to scale).

the waveguide.

4.4 Liquid-Crystal Packaging

The devices were fabricated in a CMOS-compatible 300-mm wafer-scale silicon-photonics process at the State University of New York Polytechnic Institute's (SUNY Poly) Albany NanoTech Complex. The silicon-photonics platform and fabrication process are described in Ch. 2.

Then, further chip-scale fabrication and packaging are done in house at the MIT fabrication facilities as back-end steps. An overview of the in-house fabrication and packaging process is shown in Fig. 4.6. The initial cross section of the chip received from CNSE consists of a silicon-nitride (SiN) waveguide recessed within a silicon-dioxide cladding, with an empty trench above the waveguide (which is achieved via a second SiN etch stop layer), as well as electrodes on either side of the empty trench. A more detailed description of the in-house fabrication and packaging process is given

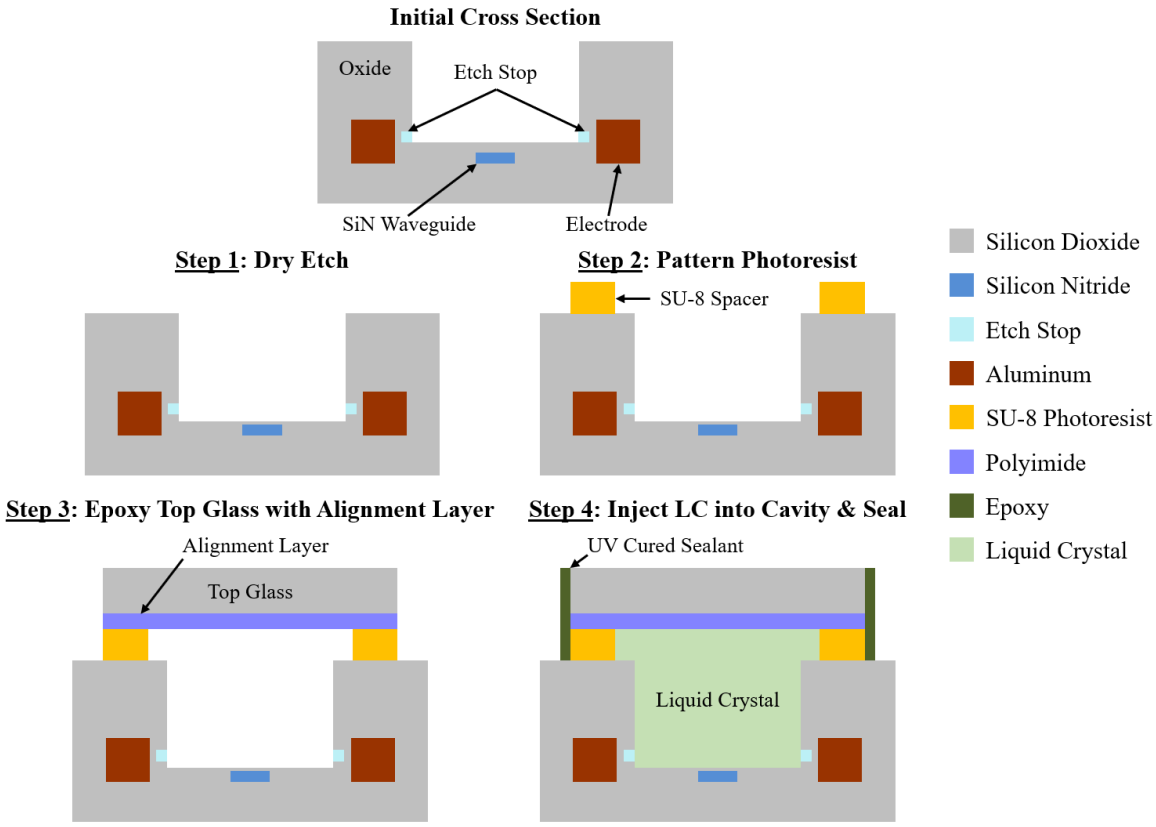

Figure 4.6: Cross-sectional diagram of the liquid-crystal packaging process. The initial cross section consists of the SiN waveguide, empty trench, and electrodes. Step 1: dry etch to bring trench closer to waveguide. Step 2: pattern SU-8 photoresist spacer layer. Step 3: epoxy top glass chip with alignment layer on top of spacer layer. Step 4: inject liquid crystal into cavity and seal with UV-cured epoxy.

below; however, a brief overview of the process consists of four steps, as shown in Fig. 4.6. The first step is to perform a dry etch to bring the trench closer to the waveguide. The second step is to pattern an SU-8 photoresist spacer layer. The third step is to epoxy a glass chip with an alignment layer on top of the SU-8 spacer layer. The fourth step is to inject the LC into the formed cavity and seal the cavity with UV-cured epoxy. More details are provided below.

4.4.1 Reactive-Ion Etching

The first in-house fabrication step (Step 1 in Fig. 4.6) is to perform a reactive-ion etch, which is a type of dry etch [99, 100]. This is done to reduce the thickness of the oxide layer in between the waveguide and the bottom of the trench. Initially, the

trench is 60 nm above the SiN waveguide. The thinness of this oxide gap is limited in the wafer-scale fabrication by how close the two SiN layers (the waveguide layer and the etch stop layer) can be successfully patterned. Hence, this oxide gap is further reduced in-house on the chip scale via a reactive-ion etch. This is an important step, because lowering the bottom of the trench brings the liquid-crystal region closer to the top of the waveguide. This maximizes the interaction of the mode in the waveguide with the liquid crystal, allowing for more compact devices. (The significance of this heightened interaction is explained in more detail in Sec. 5.1.)

The resulting thickness of the oxide gap is very important, because the device performance is significantly impacted by the gap thickness. Hence, it is imperative to precisely characterize the etch rate of the implemented process. This is achieved by etching four different chips with four incrementally increasing etch durations, then taking cross-section images to infer the resulting oxide gap thickness for each of the four chips, from which the etch rate can be calculated. However, due to typical wafer-scale fabrication variation, the initial oxide gap thickness can vary across the wafer. Hence, it is necessary to not only measure the resulting gap thickness after etching, but also the initial gap thickness before etching. Transmission electron microscopy (TEM) cross-section images are taken of the four chips in two locations (TEM images taken by SUNY Poly). The initial oxide gap thickness is measured from a location on each chip that is not exposed to the reactive-ion etch, as highlighted in Fig. 4.7. The initial oxide gap thickness varies across these four chips by > 10 nm, which demonstrates the importance of taking the initial gap thickness into account when calculating the etch rate.

Transmission electron microscopy cross-section images of the four chips are taken in a second location, at the site of a trench, to measure the resulting oxide thickness after etching, as shown in Fig. 4.8. The chips are etched with a recipe using 3 sccm of O_2 and 30 sccm of CF_4 at 30 mT pressure with 100 W applied radio-frequency power. The four chips are etched for four, five, six, and seven minutes, respectively. The first two chips are only etched into the oxide gap layer, so they can be used to calculate the etch rate of oxide, while the last two chips are etched partially into the SiN waveguide,

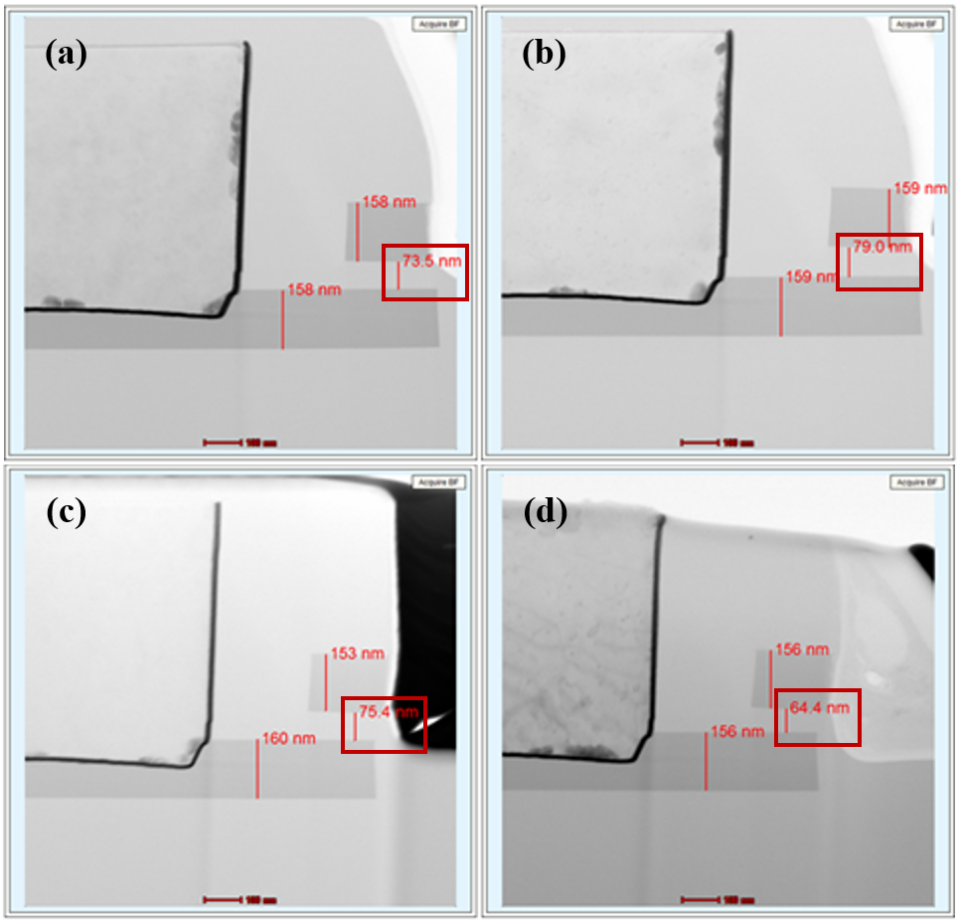

Figure 4.7: Transmission electron microscopy (TEM) cross-section images on a section of the chip that is not exposed to the reactive-ion etch, highlighting original oxide gap thickness between the SiN waveguide layer and SiN etch stop layer on four different chips prior to (a) four minutes, (b) five minutes, (c) six minutes, and (d) seven minutes of reactive-ion etching. (TEM images taken by SUNY Poly.)

so they can be used to calculate the etch rate of SiN. The selectivity of this etch recipe is evident in Fig. 4.8d, where the SiN waveguide is seen to be etched significantly more than the oxide cladding surrounding it. Taking into account the initial gap thicknesses of the four chips (from Fig. 4.7), the etch rate of oxide is approximately 25 nm/min and the etch rate of SiN is approximately 54 nm/min. This etch rate characterization allows for precise chip processing.

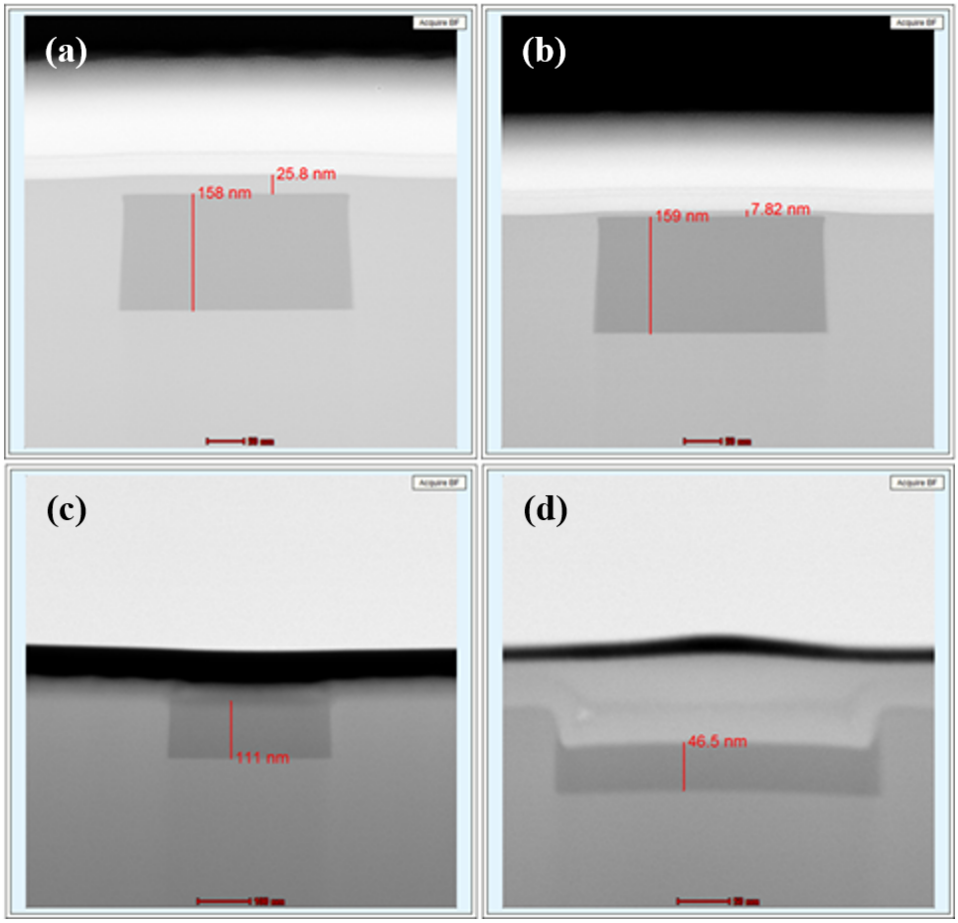

Figure 4.8: Transmission electron microscopy (TEM) cross-section images of SiN waveguide within oxide cladding after (a) four minutes, (b) five minutes, (c) six minutes, and (d) seven minutes of reactive-ion etching. (TEM images taken by SUNY Poly.)

4.4.2 Waveguide Reveal

The reactive-ion etch allows for the oxide gap between the waveguide and the liquid-crystal trench to be minimized. However, a step which further increases the interaction between the waveguide mode and the liquid crystal is to reveal the waveguide to the trench, as shown in Fig. 4.9. The significance of revealing the waveguide to the liquid-crystal trench is described in Sec. 5.1.

Initially, this waveguide reveal process was intended to be performed in house at the MIT facilities via a wet-etch process using hydrofluoric acid. However, it was discovered that, since the wet etch is isotropic (meaning it etches at the same rate in

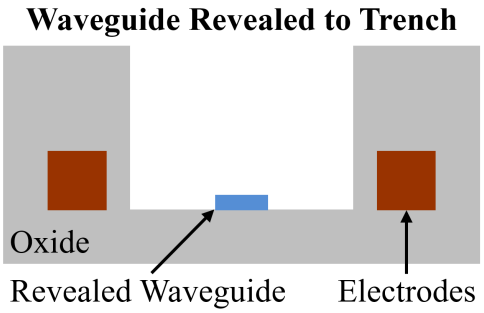

Figure 4.9: Diagram of the initial cross section with the waveguide revealed to the trench.

every direction, rather than just straight down) [101, 102], the waveguide is reshaped by the wet etch from its desired rectangle profile to a trapezoidal shape. Furthermore, the hydrofluoric-acid etch was discovered to not be selective enough to the silicon dioxide over the silicon nitride, which results in a reduction in the waveguide height. The approximate resulting waveguide shape and size reduction after the wet etch are shown in Fig. 4.10.

As a result of the in-house wet etch proving ineffective at revealing the waveguide, a waveguide reveal process was developed by SUNY Poly. This process successfully reveals the waveguide to the trench, while maintaining the integrity of the original waveguide shape and dimensions. A scanning-electron-microscopy (SEM) in-line image of the waveguide revealed to the trench is shown in Fig. 4.11 (SEM image taken by SUNY Poly). Overall, there are two different SUNY Poly fabrication processes. One process results in an embedded waveguide with a silicon-dioxide gap between the

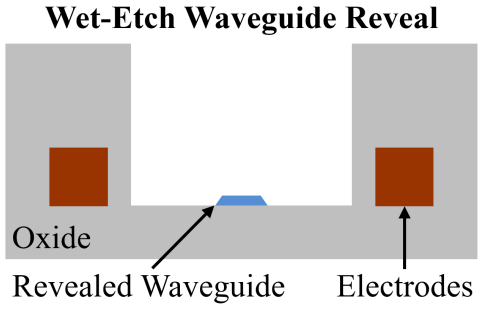

Figure 4.10: Diagram of the cross section of the revealed waveguide after the hydrofluoric-acid wet etch, showing the undesired trapezoidal waveguide shape and reduced dimensions.

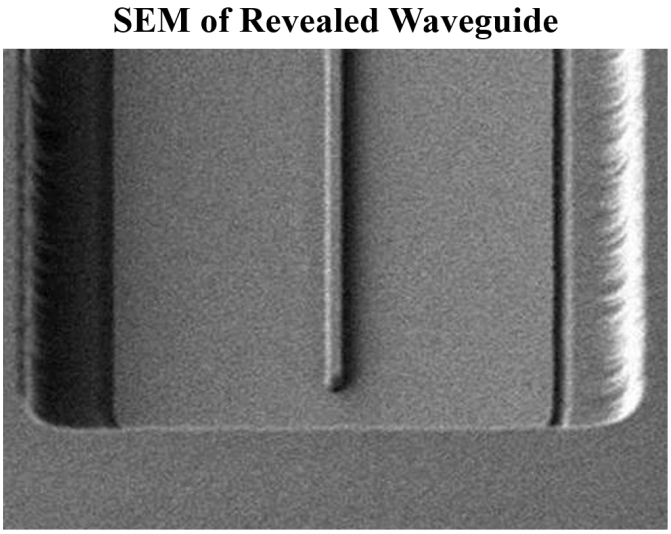

Figure 4.11: Scanning-electron-microscopy (SEM) image of the waveguide revealed in the trench (SEM image taken by SUNY Poly).

waveguide and the trench, which is then thinned down via an in-house reactive-ion etch at MIT, and a second process results in a fully revealed waveguide which does not need to go through the in-house etch.

4.4.3 Photolithography

The second in-house fabrication step (Step 2 in Fig. 4.6) is to pattern an SU-8 photoresist layer on top of the photonic chip. This photoresist layer acts as a spacer to offset the top glass chip from the surface of the photonic chip, such that a cavity is formed into which the liquid crystal will be injected. The SU-8 is not patterned as a continuous strip around the chip; instead, there is one input gap at one end of the chip and two output gaps at the other end of the chip, as shown in Fig. 4.12.

The photolithography process used to pattern the photoresist spacer layer varies based on the type of photoresist used, the substrate onto which it is patterned, the type of mask used, and the specific fabrication tools used during the process. Hence, the proper photolithography recipe had to be developed to ensure a precise, uniform, and repeatable process. SU-8 photoresist is used because it is permanent and the layer thickness can be controlled and varied fairly easily. The photolithography process for SU-8 photoresist consists of coating, soft bake, UV exposure, post-exposure bake, and

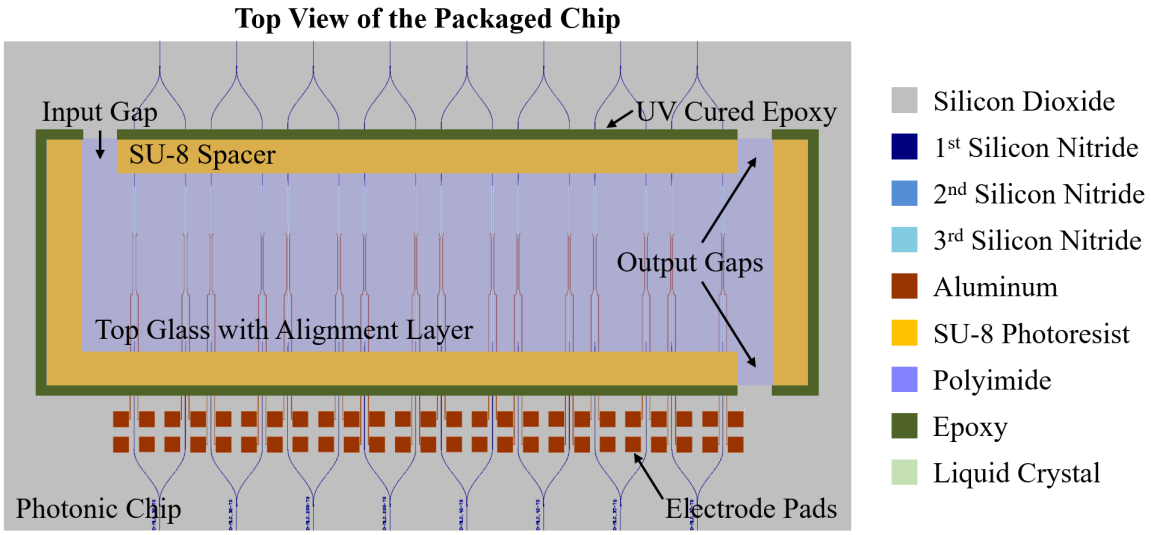

Figure 4.12: Simplified top view diagram of the packaging process after Step 3, showing input and output gaps in the SU-8 spacer layer to allow for liquid-crystal injection and uniform filling, top glass alignment chip placement, and UV-cured epoxy sealant.

development.

The coating speed and duration determines the thickness of the photoresist layer. The desired photoresist thickness is 600 nm, so SU-8 2000.5 photoresist is coated at 2000 rpm for 30 sec, with a ramp up of 10 sec from an initial speed of 500 rpm. These coating specifications were taken from the SU-8 2000 data sheet. To achieve consistent results, the soft bake duration was significantly increased from the recommended duration, to 4 min at 100 °C, via a hot plate with a silicon wafer underneath the chip to ensure uniform heat distribution.

Since SU-8 is a negative photoresist, the UV exposure step causes molecular cross linking and, hence, the areas that are exposed will remain intact after the chip is developed. The exposure duration depends heavily on the type of mask used and the output energy of the tool being used. The exposure duration had to be varied until the proper conditions were found. As shown in Fig. 4.13a, if the chip is under exposed, the resulting photoresist layer will not be of uniform thickness and the photoresist will be undesirably removed from some locations, resulting in improper photoresist patterning and structures. As shown in Fig. 4.13c, if the chip is over exposed, the resist will not be removed properly in regions where it should be removed completely,

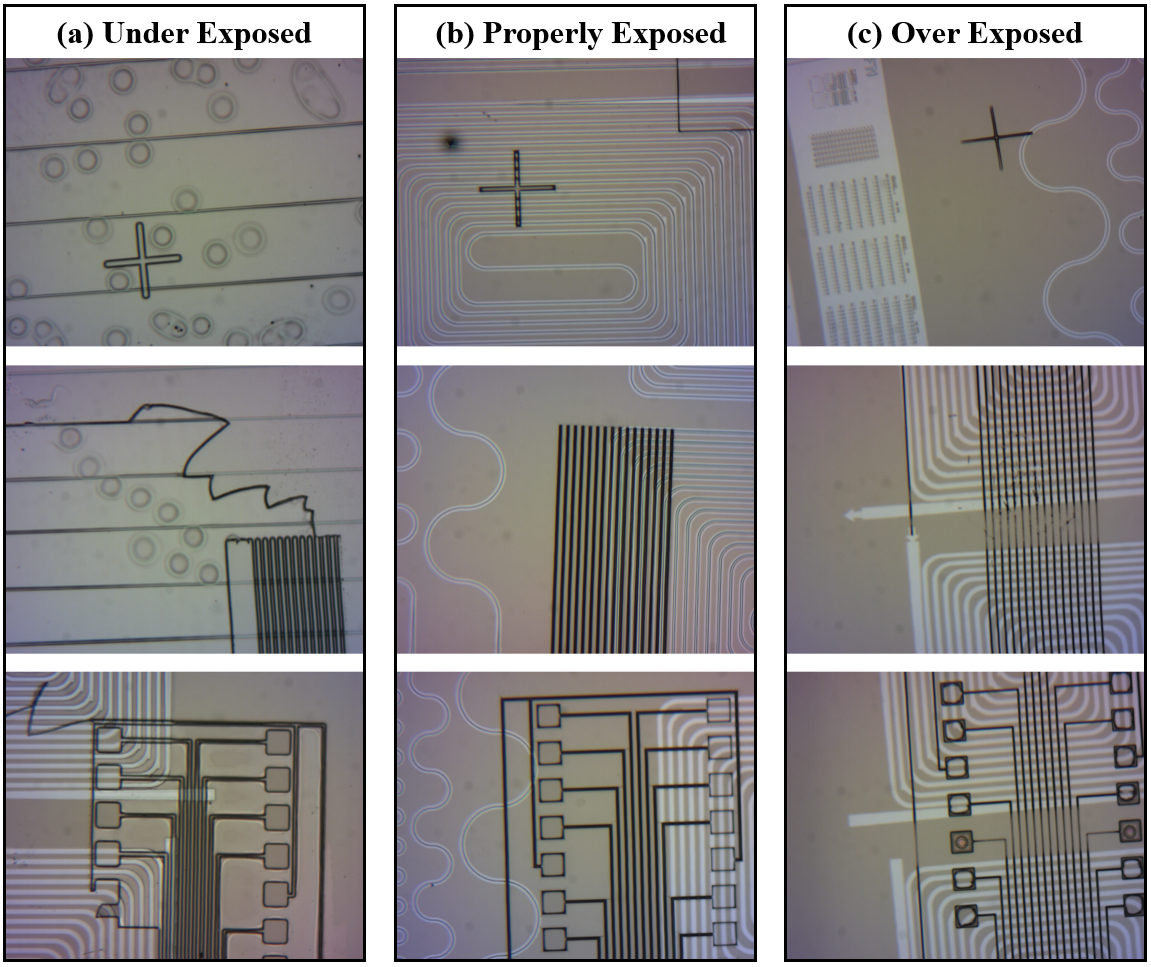

Figure 4.13: Resulting resist pattern due to chip being (a) under exposed, (b) properly exposed, and (c) over exposed.

which may also result in the photoresist structures having non-perpendicular walls or edges. In contrast, a properly exposed chip will result in high-resolution structures with nearly-perpendicular walls and uniform thickness, as shown in Fig. 4.13b. Similar to the soft bake, the post-exposure-bake duration was increased as well to 4 min at 100 °C, to ensure consistency.

During the development step, the photoresist that was not cross linked during exposure will be dissolved by the solvent. If the chip is overdeveloped, even the photoresist that was cross linked during the exposure step will begin to dissolve, as shown in Fig. 4.14. This causes the resulting photoresist layer to become damaged and the thickness becomes very inconsistent. For development using the solvent propylene

Figure 4.14: Resulting photoresist pattern due to over-development.

glycol monomethyl ether acetate, 1 min was found to achieve consistent results.

The above photolithography recipe targeted a final photoresist thickness of 600 nm. The thickness of the resulting photoresist was measured using a Veeco Dektak 150 Surface Profilometer stylus metrology measurement. The thickness across a 400-µm-wide photoresist structure was found to be approximately 620 nm, as shown in Fig. 4.15.

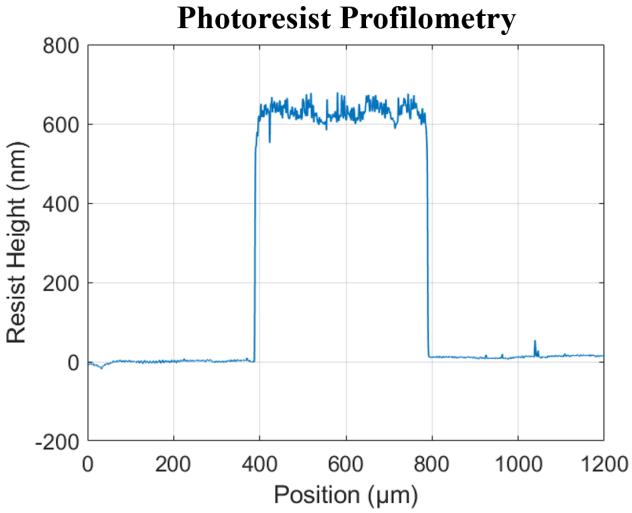

Figure 4.15: Profilometry of resulting SU-8 resist using a Veeco Dektak 150 Surface Profilometer, showing resist thickness and width.

4.4.4 Liquid-Crystal Injection

The final set of in-house fabrication steps (Steps 3 and 4 in Fig. 4.6) is to epoxy a glass chip on top of the SU-8 spacer layer, inject the liquid crystal into the formed cavity, and seal the cavity. A glass chip, which has an organic polyimide alignment layer on the bottom of it is placed on top of the SU-8 photoresist spacer layer, as shown in Fig. 4.16a. The glass chip is obtained from Instec and is diced in-house at MIT to the appropriate size. The polyimide alignment layer mechanically anchors the liquid-crystal molecules when no external electric field is applied across the liquid-crystal region. The alignment layer anchors the liquid-crystal molecules at the surface of the alignment layer (towards the top of the formed cavity) and the alignment propagates down through the liquid-crystal region to the bottom of the trench. Once the glass alignment chip is properly placed and aligned on top of the SU-8 photoresist spacer layer, the two chips are carefully transferred to a clamp, as shown in Fig. 4.16b. The clamp applies light pressure and ensures that all edges of the two chips are uniformly touching. Then, Norland optical adhesive, a UV-cured epoxy, is used to epoxy the alignment chip to the photonic chip, as shown in Fig. 4.12. The input and output gaps in the SU-8 spacer layer remain open with no epoxy covering them, to allow for the liquid crystal to be injected into the cavity.

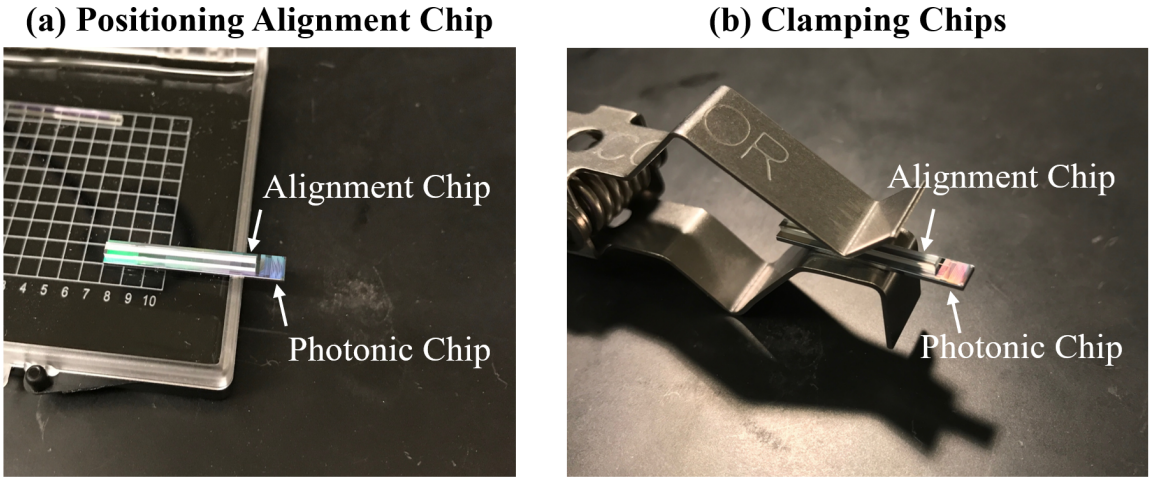

Figure 4.16: Photograph of a glass chip (containing alignment layer) on top of a photonic chip (a) during chip alignment process and (b) transferred to a clamp to provide light pressure during the epoxy process.

At this point, a cavity has been formed between the photonic chip and the glass alignment chip. 5CB liquid crystal is then injected into this formed cavity through the input gap on one end of the chip. The chip is then placed into a dessicator with ambient vacuum, to pull the air out of the cavity via the two output gaps on the other end of the chip. The liquid crystal flows into the cavity via capillary action. Once the liquid crystal fills up the entire cavity, the input and output gaps are sealed with the UV-cured epoxy. Filling the chip with liquid crystal in a vacuum chamber helps ensure that no air bubbles remain in the cavity or trenches.

4.5 Liquid-Crystal-Packaging Evaluation Techniques

Here, we demonstrate evaluation techniques for analyzing LC misalignment using both standard and polarizing microscopes. Then, we develop a procedure to improve packaged LC alignment by transitioning the LC between temperature-dependent phases. Finally, we demonstrate the significant effects that LC misalignment and UV exposure can have on device performance.

First, we established a technique for evaluating the success of the LC packaging process using a polarizing microscope. Specifically, we used the polarizing microscope to evaluate if the LC properly filled into the cavity and uniformly anchored to the alignment layer. In general, a polarizing microscope can be used to image a birefringent sample with a polarized light source impingent on the sample and a polarization-selective analyzer after the sample [79]. Here, we design the polarizing microscope such that the polarization of the incident light is parallel to the expected LC alignment direction, the incident light travels through the LC-filled cavity of the packaged chip, reflects off the bottom of the LC region, and the reflected light travels through a polarization analyzer that is oriented perpendicular to the LC alignment direction, as shown in Fig. 4.17.

If the LC is aligned properly, the incident light will undergo no polarization rotation, and the analyzer will block the reflected light, resulting in a dark image. However, if the LC molecules are misaligned, the polarization of the incident light

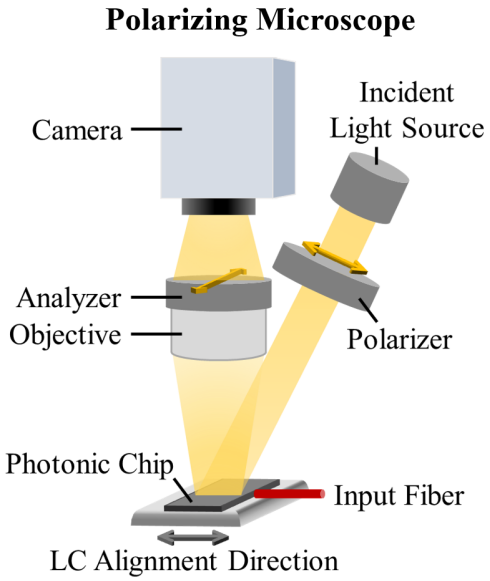

Figure 4.17: Simplified diagram of the polarizing microscope used to evaluate liquid-crystal alignment (not to scale).

will change as it travels through the LC-filled cavity, and the analyzer will no longer block all the reflected light, resulting in a bright image. Examples of a poorly filled cavity, where the LC molecules are misaligned, and a properly filled cavity, where the LC molecules are uniformly aligned, are shown in Fig. 4.18.

Next, we developed a heat-based technique to reorient the LC molecules in a packaged chip, since non-uniform LC misalignment can significantly degrade device

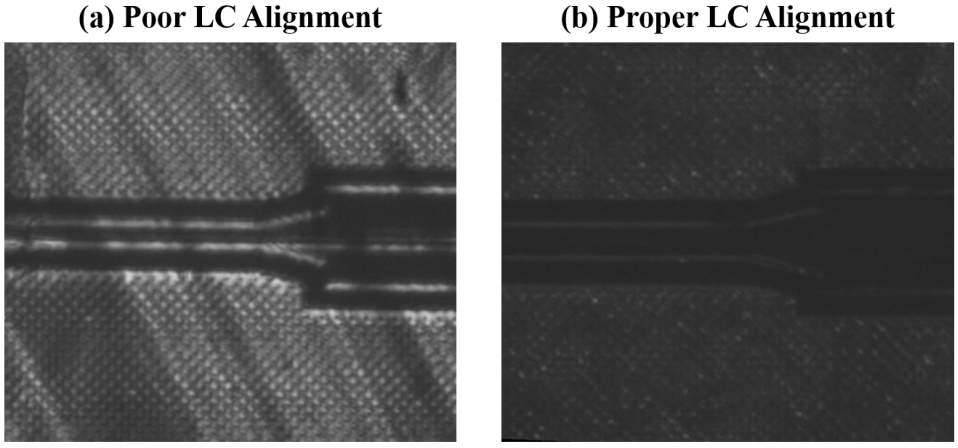

Figure 4.18: Micrographs taken using the polarizing microscope demonstrating (a) poor liquid-crystal alignment and (b) proper liquid-crystal alignment after packaging.

performance. We achieve this LC molecule reorientation by transitioning the LC between temperature-dependent phases. 5CB liquid-crystal material transitions from crystalline to nematic states at 18°C and from nematic to isotropic states at 35°C. We heat the chip to bring the LC to its isotropic state and then slowly cool it back down to its nematic state, which allows for the LC molecules to properly and uniformly anchor to the alignment layer. Before heating, the LC region is visibly misaligned, as shown in Fig. 4.19a. During heating, the LC transitions to the isotropic state, making the LC region optically clear, as shown in Fig. 4.19b. After the chip is cooled down, the LC returns to its nematic state and the molecules properly anchor to the alignment layer, resulting in an optically-clear LC region, as shown in Fig. 4.19c.

To demonstrate the importance of proper alignment of the LC molecules and the impact of this heat-based reorientation technique, we experimentally characterized an integrated LC-based phase modulator in a Mach-Zehnder-interferometer (MZI) test structure (introduced in detail in Ch. 5) on a packaged chip. We couple a 632.8-nm off-chip laser into the MZI, vary the peak voltage of a 10-kHz square wave on one arm of the MZI, and measure the power output of the MZI. Initially, the LC was poorly filled into this cavity, resulting in the output power remaining constant with applied voltage, implying that no phase modulation is occurring. Then, we used the heat-based reorientation technique to improve the LC molecule alignment and retested the MZI, successfully confirming the expected amount of phase modulation.

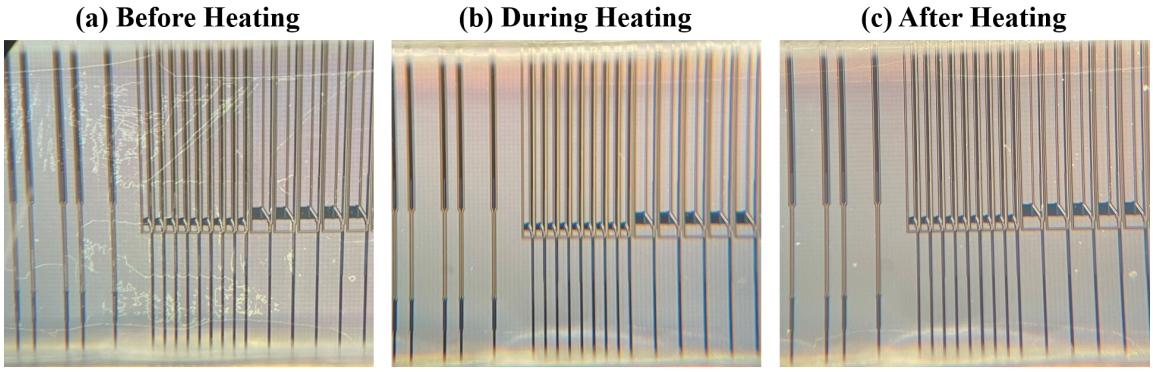

Figure 4.19: Micrographs taken using a standard microscope of the packaged LC region (a) before heating, (b) during heating, and (c) after heating and cooling back down.

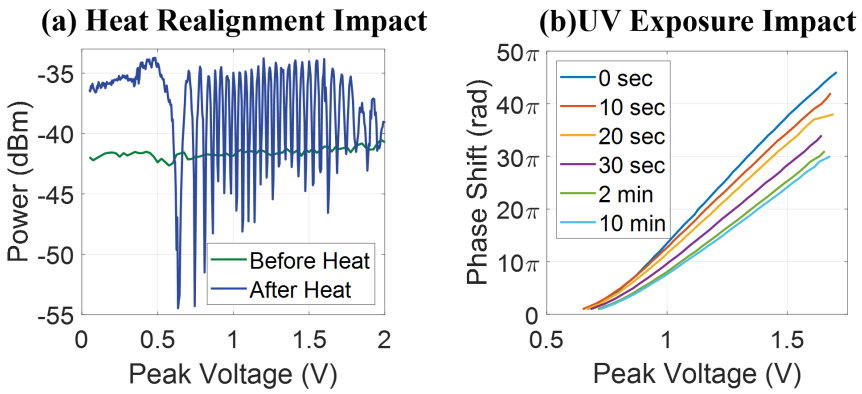

Figure 4.20: (a) Experimental results showing output power of an integrated LC-based phase modulator in an MZI test structure versus peak voltage applied to one arm of the MZI before (green) and after (blue) heating. (b) Experimental results showing phase shift of an integrated LC-based phase modulator as a function of peak voltage for varying UV exposure times.

Results of modulation before and after heating are shown in Fig. 4.20a, highlighting the significant impact that LC alignment and reorientation via heating can have on device performance.

Finally, we explored the effect of UV exposure on integrated LC-based modulators. This is an important consideration since some steps in the packaging process use UV-cured epoxy. Specifically, we characterize performance of the integrated LC-based phase modulator in the MZI test structure under increasing UV exposure. We expose the chip to 365-nm-wavelength light of intensity 2.5Wcm^{-2} for increasing durations, up to 10 minutes. As shown in Fig. 4.20b, the UV exposure results in significant degradation in the device performance. This result confirms that precautions must be taken during packaging steps that require UV exposure.

4.6 Conclusion

In this chapter, liquid-crystal theory, including birefringence, nematic molecular alignment, anchoring via a mechanical alignment layer, and molecular rotation via an external electric field were introduced. As discussed, these properties can be leveraged in an integrated-photonics platform via integrating a liquid-crystal-filled trench above a silicon-nitride waveguide to take advantage of the birefringence and by plac-

ing electrodes on each side of this trench to actively tune the refractive index of the liquid-crystal region. Furthermore, the in-house chip-scale back-end fabrication and liquid-crystal packaging process for integrated liquid-crystal into our silicon-photonics platform was described. Finally, we discussed important considerations and evaluation techniques for successful LC packaging. This work facilitates wide-spread use and higher-yield integration of LC into silicon-photonics platforms, enabling compact and power-efficient on-chip modulation.

Chapter 5

Integrated Visible-Light Liquid-Crystal-Based Phase Modulators

In this chapter, integrated liquid-crystal-based phase modulators operating at visible wavelengths are developed and experimentally demonstrated. A visible-light silicon-nitride-based 300-mm-wafer foundry platform and a liquid-crystal integration process were developed to leverage the birefringence of liquid crystal to actively tune the effective index of a section of silicon-nitride waveguide and induce a phase shift over its length. In Sec. 5.1, we develop and theoretically describe the integrated visible-light liquid-crystal-based phased modulator. In Sec. 5.2 we fabricate and experimentally demonstrate these phase modulators. The device was experimentally shown to achieve a 41π phase shift within ± 2.4 V for a 500-μm-long modulator, which means that a 2π phase shifter would need to be only 24.4 μm long. This liquid-crystal-based device can achieve greater modulation with a smaller physical footprint and lower power consumption than conventional heater-based devices (discussed in Sec. 4.1). It is a compact and low-power solution to the challenge of integrated phase modulation in silicon nitride and paves the way for future low-power small-form-factor integrated systems at visible wavelengths.

The following work was done in collaboration with Manan Raval (MIT), Thomas

Dyer (SUNY Polytechnic), Christopher Baiocco (SUNY Polytechnic), Michael R. Watts (MIT), and Jelena Notaros (MIT). This work has been published in [61, 72].

5.1 Integrated Visible-Light Liquid-Crystal-Based Phase-Modulator Theory and Design

To enable compact integrated visible-light phase modulation, liquid crystal is integrated into a silicon-photonics platform to implement an integrated liquid-crystal-based phase modulator. A simplified final cross-sectional diagram of the modulator, after the fabrication and packaging process outlined in Sec. 4.4, is depicted in Fig. 5.1. The modulator is based on a silicon-nitride waveguide that is recessed within a silicon-dioxide cladding. A trench is etched into the silicon-dioxide cladding above the waveguide and the trench is filled with liquid crystal. Metal electrodes are integrated on each side of the liquid-crystal-filled trench. Since the liquid-crystal region is directly above the silicon-nitride waveguide, the mode of the light that propagates through the waveguide is pulled up slightly into the liquid-crystal region (as shown in Fig. 4.4b). Hence, the effective refractive index of the waveguide is influenced by the refractive index of the liquid-crystal region. For example, if the index of the liquid

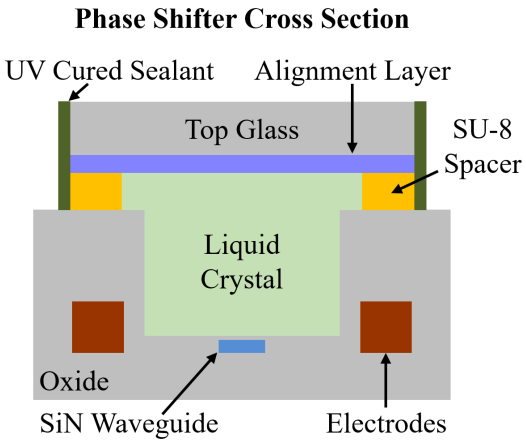

Figure 5.1: Simplified cross-sectional diagram of the liquid-crystal-based phase modulator consisting of a silicon-nitride waveguide recessed within silicon dioxide below a liquid-crystal-filled trench with integrated electrodes on each side (not to scale).

crystal is increased, the mode becomes more concentrated in the liquid-crystal region (as shown in Fig. 4.4c) and the effective index of the mode increases.

As discussed in Sec. 4.2, the refractive index of the liquid-crystal medium depends on the orientation of the liquid-crystal molecules with respect to the direction of light propagation in the waveguide. To determine the initial orientation of the liquid-crystal molecules, a mechanical alignment layer is used to ensure that the molecules are initially aligned parallel to the waveguide, as shown in Fig. 5.1. The alignment layer anchors nearby molecules and the alignment propagates through the entire region since nematic liquid crystal self aligns in one dimension.

To take advantage of the birefringence of the liquid crystal and vary the effective index of the mode in the silicon-nitride waveguide, the liquid-crystal molecules must be rotated with respect to the waveguide. This rotation can be achieved by applying a voltage across the liquid-crystal region, since liquid-crystal molecules align to an external electric field. To apply this external electric field, integrated metal electrodes are patterned on each side of the trench, as depicted in Fig. 5.1. These electrodes run alongside the entire length of the liquid-crystal-filled trench to uniformly vary the refractive index throughout the modulator, as shown in Fig. 4.5b–c. As the voltage applied across the integrated electrodes increases past an initial threshold voltage that is large enough to overcome the mechanical anchoring of the alignment layer, the molecules rotate to align to the electric field until they are finally oriented perpendicular to the waveguide at a maximum voltage, as shown in Fig. 4.5c. As the liquid-crystal molecules rotate from their initial state to their final state, the refractive index of the liquid-crystal medium changes from the minimum to the maximum index of the liquid crystal. As this refractive index increases, the effective index of the waveguide mode also increases and, hence, a phase shift is induced along the length of the modulator. As the voltage across the liquid-crystal region is decreased and the external electric field is reduced, the molecules rotate back to their initial anchored orientation.

The phase shift achieved by this proposed integrated liquid-crystal-based phase modulator was simulated using a numerical mode solver (Lumerical MODE). These

simulations assumed using 5CB liquid crystal, which has a nominal refractive index range of 1.53 to 1.7 at a wavelength of 632.8 nm [97, 98]; however, the simulations were limited to a maximum liquid-crystal index of 1.62, since the waveguide mode is poorly confined past this value.

The loss as a function of liquid-crystal refractive index is shown in Fig. 5.2 and, consequently, for this simulated cross section, the liquid-crystal refractive index should be limited to 1.62 to maintain low loss. Note that this simulated loss is only taking into account the dissipation into the electrodes. It does not take into account material loss in the waveguide, cladding, and liquid crystal, or surface roughness of the waveguide. These parameters are expected to have an impact on the loss, and are affected by multiple factors, such as waveguide and trench dimensions, and liquid-crystal refractive index.

Simulation results of the effective index of the fundamental transverse-electric mode as a function of the liquid-crystal refractive-index range are shown in Fig. 5.3a. As the liquid-crystal refractive index is increased, the effective index of the mode in the waveguide also increases. Hence, the birefringence of the liquid crystal results in a change in effective index, Δn, of the fundamental mode in the waveguide. This change in effective index can be used to calculate the expected phase shift for a given

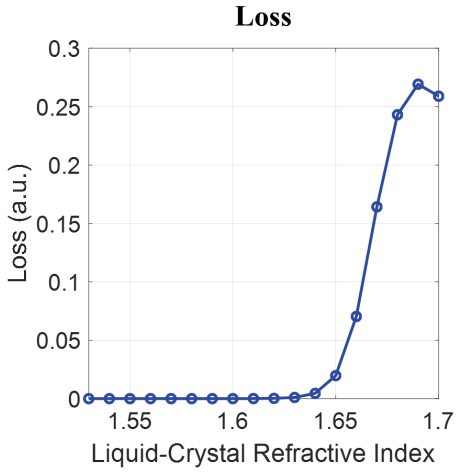

Figure 5.2: Simulated loss versus liquid-crystal refractive index, showing the significance of limiting the implemented liquid-crystal refractive-index range to a maximum value that maintains manageable loss.

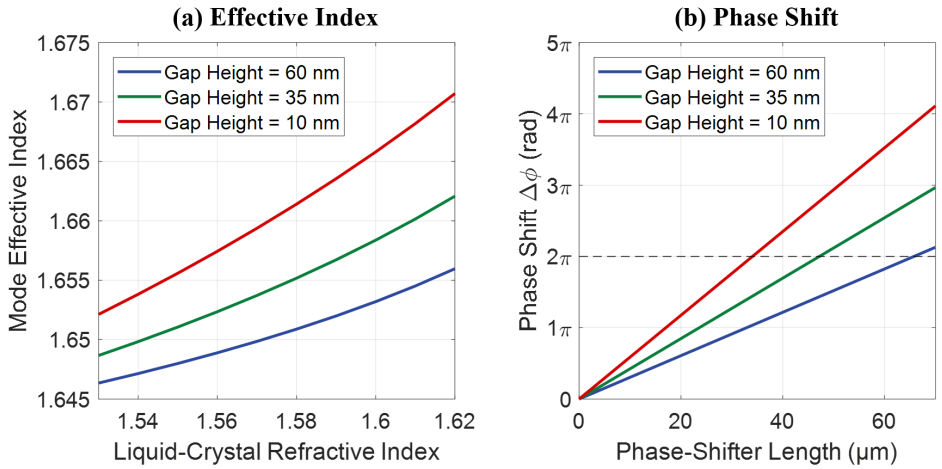

Figure 5.3: (a) Simulation results showing the change in the effective refractive index of the fundamental transverse-electric mode supported by the liquid-crystal-based phase modulator as the liquid-crystal refractive index is tuned for three different silicon-dioxide gap heights (the height of the silicon-dioxide gap in between the top of the silicon-nitride waveguide and the bottom of the liquid-crystal-filled trench). (b) Simulated resulting phase shift as a function of phase-shifter length for three different silicon-dioxide gap heights. The change in effective index and the amount of phase shift increase as the gap height is decreased.

shifter length using

$$\Delta\phi = \frac{2\pi L \Delta n}{\lambda_o}, \tag{5.1}$$

where $\Delta\phi$ is the phase shift, L is the length of the phase shifter, Δn is the change in effective index of the fundamental mode in the waveguide, and λ_o is the free-space wavelength. The calculated phase shift as a function of phase-shifter length is shown in Fig. 5.3b.

There are many variables that affect how the waveguide mode effective index is impacted by the liquid-crystal region and hence, the amount of phase shift that is possible for a given shifter length. One such variable that impacts the device performance is the thickness of the layer of silicon dioxide in between the waveguide and the bottom of the liquid-crystal-filled trench. The simulation results in Fig. 5.3 demonstrate the impact that the height of the silicon-dioxide gap in between the top of the silicon-nitride waveguide and the bottom of the liquid-crystal-filled trench has on the effective index of the waveguide mode and the resulting device performance. If the silicon-dioxide gap is thinner, the mode in the waveguide interacts more with

the liquid crystal and, hence, there is a greater variation in the effective index of the waveguide mode. This can be seen in simulation results of the mode profile for a thick versus thin oxide gap shown in Fig. 5.4. As can be seen in Fig. 5.4a, when there is a thicker silicon-dioxide gap between the waveguide and the liquid-crystal region, the mode is only slightly pulled up into the liquid-crystal region and, hence, is impacted less by the liquid-crystal medium. On the other hand, if the silicon-dioxide gap is thinned down the optical mode gets pulled up farther into the liquid-crystal region, as shown in Fig. 5.4b, and is impacted more strongly by the liquid-crystal medium.

Since the thinner gap enables greater variation of the waveguide mode effective index, it allows for a greater amount of phase shift for a given shifter length. Here, we explore silicon-dioxide gap thicknesses of 10 nm to 60 nm, since the devices are initially fabricated with a silicon-dioxide thickness of 60 nm, which is then etched down to 10 nm (the implemented etching process is described in Sec. 4.4.1). For example, a nominal silicon-dioxide gap thickness of 60 nm results in a change in effective index of $\Delta n = 0.01$, which would require a 66-μm-long shifter length to achieve a 2π phase shift. If the thickness of the silicon-dioxide gap between the waveguide and the liquid-crystal region is reduced to 10 nm, the waveguide mode interacts more strongly with the liquid crystal and, hence, there is a larger change in effective index of $\Delta n = 0.02$. This larger change in effective index means that a 2π phase shift can be achieved in a much shorter shifter length of only 34 μm. This highlights the importance of

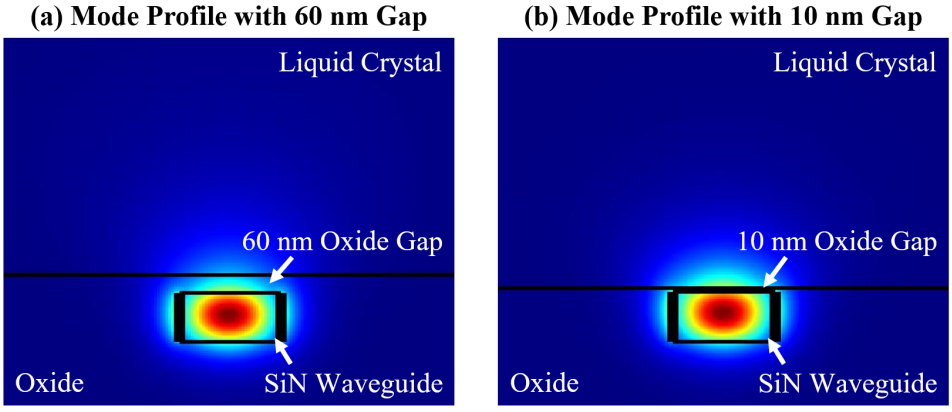

Figure 5.4: Simulation results showing the mode profile of the fundamental mode with a silicon-dioxide thickness of (a) 60 nm and (b) 10 nm.

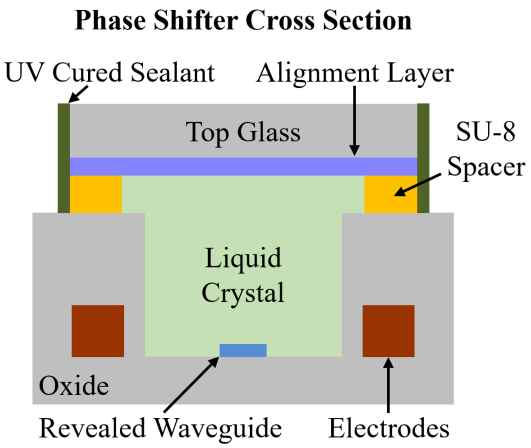

Figure 5.5: Simplified cross-sectional diagram of the liquid-crystal-based phase modulator with the waveguide revealed to the liquid-crystal region (not to scale).

reducing the thickness of the silicon-dioxide gap that separates the waveguide from the liquid-crystal region; doing so enables a significantly more compact modulator.

Another way to further improve the performance of the phase modulator is to reveal the waveguide to the liquid-crystal region. The liquid-crystal-filled trench can be etched down all the way to the bottom of the waveguide, to reveal the top and sides of the waveguide to the liquid crystal, as shown in Fig. 5.5. Now, the waveguide is exposed to the liquid crystal on three sides, rather than just on top. This means that more of the waveguide mode will interact with the liquid-crystal region, as shown in Fig. 5.6.

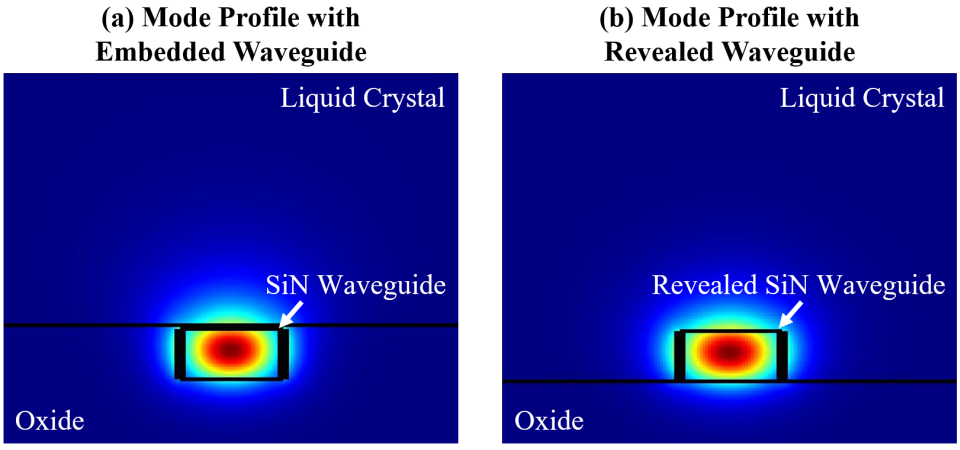

Figure 5.6: Simulation results showing the mode profile of the fundamental mode with (a) an embedded waveguide and (b) a revealed waveguide.

Similar to the discussion on silicon-dioxide gap thickness above, if the silicon-dioxide surrounding the waveguide is etched even farther down to expose the top and sides of the waveguide, then the optical mode is situated more within the liquid-crystal region and, hence, the effective refractive index of the mode will be impacted more by the variation in liquid-crystal index. As shown in Fig. 5.7a, the effective refractive index of the waveguide mode is increased, because the liquid crystal has a higher refractive index than the silicon-dioxide cladding; however, more importantly, the range of the effective index, Δn_{eff}, increases as well, which can be seen through the greater slope of the waveguide mode effective index versus liquid-crystal index for the revealed waveguide. This greater range in the waveguide mode effective index results in more possible phase shift for a set shifter length. As shown in Fig. 5.7b, the revealed waveguide achieves a greater amount of phase shift.

For example, the original embedded waveguide requires a 34-μm-long shifter region to achieve 2π phase shift, while a revealed waveguide requires only a 22.2-μm-long phase shifter. Hence, the revealed waveguide allows for a more compact phase shifter.

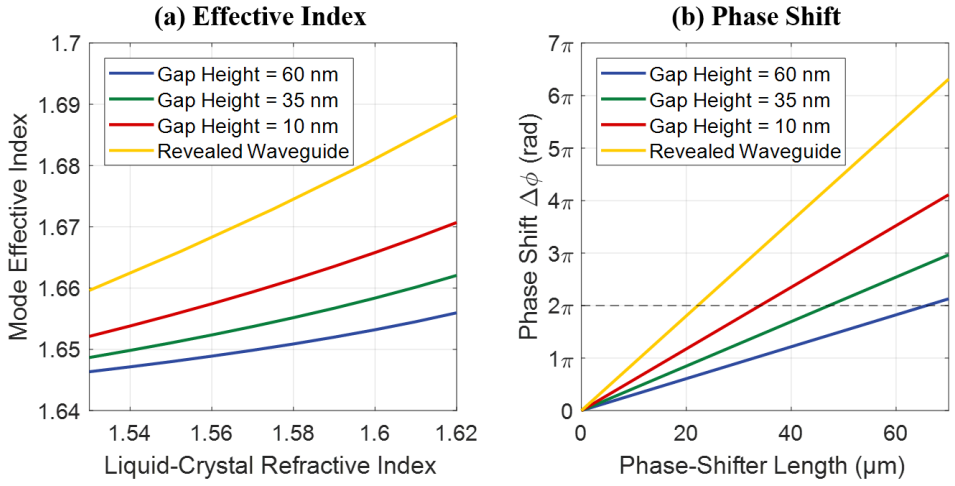

Figure 5.7: (a) Simulation results showing the change in the effective refractive index of the fundamental transverse-electric mode supported by the liquid-crystal-based phase modulator as the liquid-crystal refractive index is tuned for three different silicon-dioxide gap heights and for a revealed waveguide. (b) Simulated resulting phase shift as a function of phase-shifter length for three different silicon-dioxide gap heights and for a revealed waveguide. The change in effective index and the amount of phase shift increase as the gap height is decreased.

Note that these devices were designed for operation with the fundamental transverse-electric (TE) mode, since it is the mode most commonly used in integrated-photonics applications; however, they could also be designed for operation with a transverse-magnetic (TM) mode. A TM design would need to take into consideration that the majority of the electric field of a TM mode is oriented vertically in the waveguide. Therefore, for efficient TM operation, either the initial liquid-crystal alignment direction would need to be altered or the integrated electrodes would need to be positioned vertically along the liquid-crystal region to maximize the impact of the liquid-crystal birefringence on the electric field of the TM mode.

5.2 Integrated Visible-Light Liquid-Crystal-Based Phase-Modulator Experimental Setup and Results

The devices were fabricated in a CMOS-compatible 300-mm wafer-scale silicon-photonics process at the State University of New York Polytechnic Institute's (SUNY Poly) Albany NanoTech Complex (platform and fabrication process described in Ch. 2). The initial cross section of the device, as received from SUNY Poly, consisted of two silicon-nitride (SiN) waveguide layers recessed within a silicon-dioxide cladding, with an empty trench above the top waveguide and electrodes on each side of the empty trench. Further chip-scale fabrication and packaging were done in house at the Massachusetts Institute of Technology (MIT) fabrication facilities as back-end steps (liquid-crystal packaging process described in Sec. 4.4).

To experimentally characterize the device performance, the liquid-crystal phase shifter was fabricated in an integrated Mach-Zehnder interferometer (MZI) test structure, as depicted in Fig. 5.8. A 632.8-nm-wavelength Helium-Neon (He-Ne) laser was coupled onto the chip from an off-chip optical fiber into the bottom silicon-nitride waveguide via an input edge coupler. A 1x2 multi-mode interference (MMI) splitter was used to transition from a single waveguide to the two separate arms of the MZI. A liquid-crystal phase modulator was placed in each arm of the MZI to balance

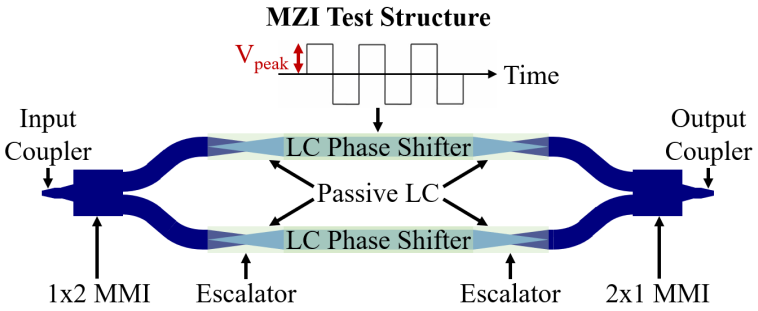

Figure 5.8: Top-view diagram of the integrated Mach-Zehnder interferometer test structure and modulation scheme (not to scale).

the two branches of the MZI. Before each phase shifter, an adiabatic escalator was used to vertically transition from the bottom silicon-nitride waveguide to the upper silicon-nitride waveguide (which is directly below the liquid-crystal-filled trench) and another adiabatic escalator was used to transition after each phase modulator from the upper waveguide to the lower waveguide. The layer transition was achieved by slowly tapering down the width of the initial waveguide while simultaneously tapering up the width of the final waveguide [103]. These escalator layer transitions were used since transitioning directly into a liquid-crystal region via a single waveguide results in significant loss across the silicon-dioxide-to-liquid-crystal interface. The escalator layer transitions allow the light to gradually enter and exit the liquid-crystal region and hence limit the loss and reflections due to the abrupt change in refractive index. Simulation results comparing the transmission using a direct-interface transition versus a vertical-transition escalator of various lengths are shown in Fig. 5.9. Here, we used 100-μm-long escalator devices to couple the light between the vertically stacked silicon-nitride waveguides, to minimize loss. Finally, a 2x1 MMI coupler was used to combine the two arms of the MZI back into a single waveguide and a second edge coupler was used to couple the light from the chip to an output optical fiber, which was connected to an optical power meter.

Simultaneously, an electrical signal was applied to the MZI test structure to provide active modulation. The liquid-crystal phase modulator in each arm of the MZI has two integrated electrodes running alongside the liquid-crystal-filled trench (as

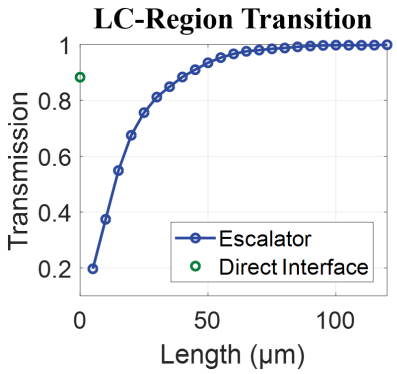

Figure 5.9: Simulation results showing transition into the LC region using either a dual-waveguide vertical-transition escalator or a single-waveguide direct interface.

shown in Fig. 5.1). These integrated electrodes route to metal pads that are located outside of the liquid-crystal-filled cavity (as shown in Fig. 4.12). A multi-pin probe was touched down on these metal pads, and the probe was connected to a function generator to apply a 10-kHz square wave with no offset voltage (the average was 0 V) across the electrodes of the phase modulator in the top arm of the MZI, as shown in Fig. 5.8. This carrier voltage waveform scheme was used to prevent ion drift in the liquid crystal, which could cause an ionic charge layer to build up on the edges of the liquid-crystal region and damage the device [79, 80, 82, 84]. No signal was applied across the phase modulator in the bottom arm of the MZI; the liquid-crystal molecules in this modulator were maintained in the initial orientation set by the mechanical alignment layer. The peak voltage of the 10-kHz square wave was then varied to tune the magnitude of the electric field across the liquid-crystal region of the phase modulator in the top arm of the MZI. As the peak voltage is increased, the refractive index of the liquid-crystal region increases, which induces a phase shift in the top arm of the MZI relative to the bottom arm. Experimentally, this results in variation of the optical power measured at the output of the MZI and, therefore, the relative phase shift can be calculated by measuring this change in output power. A diagram of the experimental setup is outlined in Fig. 5.10 and a photograph of the experimental setup is shown in Fig. 5.11.

A photograph of the packaged chip, with the input and output fibers coupling light on and off the chip and the multi-pin probe connecting to the integrated electrodes,

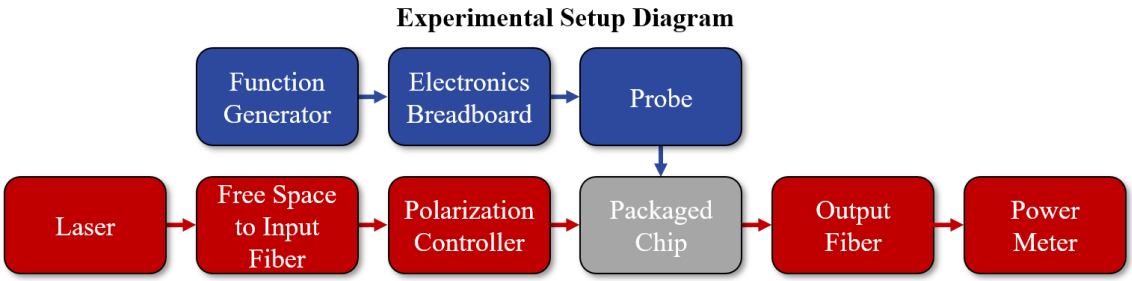

Figure 5.10: Diagram of the experimental setup, showing the optical path in red and the electrical path in blue.

is shown in Fig. 5.12.

Experimental results showing the optical power at the output of the MZI as the peak voltage applied to the phase shifter in the top arm of the MZI is varied are shown in Fig. 5.13. Since each dip in the output power occurs when the two arms of the MZI are out of phase, there is a 2π phase shift between each dip. By counting the number of dips, this 500-μm-long device with a silicon-dioxide gap thickness of 10 nm is found to achieve 36π phase shift within ±3 V (dips beyond this point are not counted due to degradation of the extinction ratio, which is attributed to loss as the

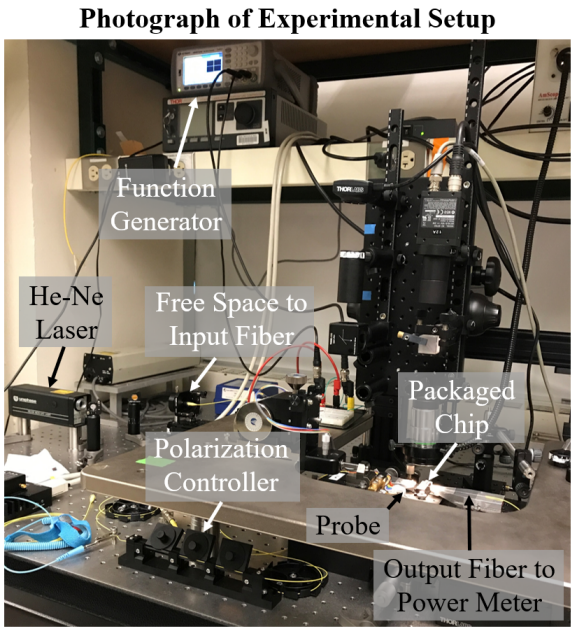

Figure 5.11: Photograph of the experimental setup, highlighting the major components.

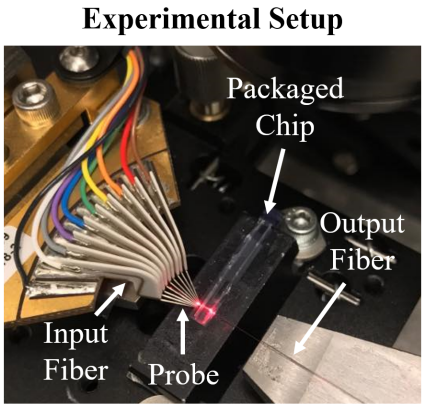

Figure 5.12: Photograph of the packaged chip on the experimental setup, showing input and output fibers coupling light on and off of the chip and a multi-pin probe connected to the integrated electrodes on the chip.

liquid-crystal refractive index is driven too high). Therefore, this phase modulator needs to be only 28 μm long to achieve a 2π phase shift.

Multiple liquid-crystal phase shifters with varying waveguide widths and liquid-crystal-filled-trench widths were also fabricated in similar integrated MZI test structures and experimentally characterized using the setup described above.

The measured phase shifts induced by the fabricated devices with various waveguide widths are shown in Fig. 5.14a. For a narrower waveguide width, the electromagnetic mode is less confined in the waveguide. This signifies that more of the mode interacts with the liquid-crystal region and is impacted more strongly by a change in liquid-crystal refractive index. Hence – as seen in Fig. 5.14a – a greater amount

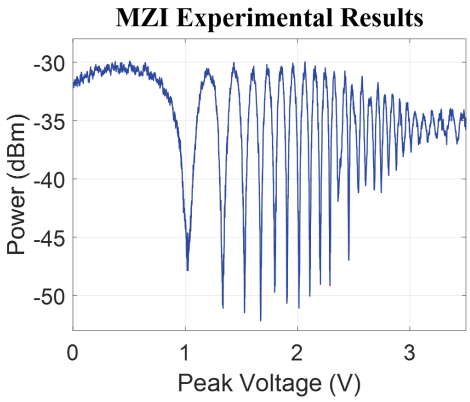

Figure 5.13: Experimentally measured power at the output of the MZI with a 10-kHz square wave of varying peak voltage applied across one arm of the MZI.

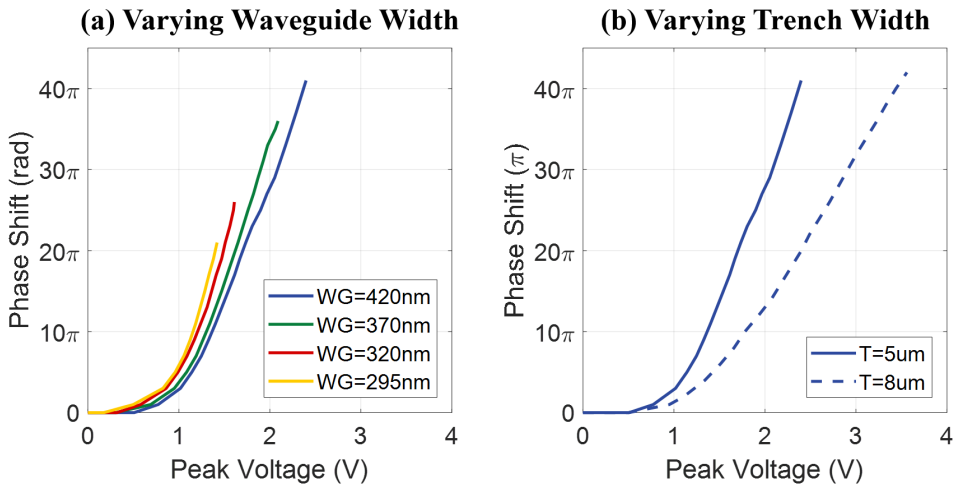

Figure 5.14: Experimentally measured phase shift as a function of applied peak voltage, inferred from MZI power measurements, for (a) four different waveguide widths and (b) two different liquid-crystal-filled-trench widths.

of phase shift is achieved within a small voltage range. However, since the electromagnetic mode is less confined and interacts with the trench sidewalls, it is also more lossy, which means that less phase shift can be achieved overall before a substantial amount of loss occurs. Hence, a larger waveguide width can achieve more overall phase shift, although a greater maximum peak voltage is required. For example, a 500-μm-long modulator with a narrow waveguide width of 295 nm achieves a 21π phase shift within ± 1.4 V; this means that a phase shifter with a waveguide width of 295 nm would need to be 47.6 μm long to achieve 2π phase shift. On the other hand, a 500-μm-long modulator with a wider waveguide width of 420 nm achieves a greater phase shift within a larger voltage range, namely 41π phase shift within ± 2.4 V; hence, a phase shifter with a waveguide width of 420 nm would need to be only 24.4 μm long to achieve 2π phase shift.

The measured phase shifts induced by the fabricated devices with two different liquid-crystal-filled-trench widths are shown in Fig. 5.14b. A narrower trench width results in less distance between the two integrated electrodes, which results in a stronger electric field for a set voltage. Hence, for a narrower trench width, a certain phase shift can be achieved within a smaller voltage range, as shown in Fig. 5.14b. If the trench width is increased and the integrated electrodes are spaced farther apart,

it takes a greater voltage to achieve a desired phase shift. For example, in the case of the 500-μm-long modulator with a waveguide width of 420 nm mentioned above, a 41π phase shift is achieved within ±2.4 V with a trench width of 5 μm; whereas, the same device with a 8-μm-wide trench requires ±3.5 V to achieve that same phase shift.

Note that the relationship between the phase shift and the applied voltage is nonlinear since the effective index of the waveguide mode varies slightly nonlinearly with respect to the liquid-crystal refractive index (as shown in Fig. 5.3a), the liquid-crystal refractive index varies nonlinearly with the applied voltage, and there is a threshold voltage that must be exceeded to ensure that the electric field applied across the liquid-crystal region is strong enough to overcome the mechanical anchoring strength of the alignment layer.

5.3 Conclusion

In this work, an integrated liquid-crystal-based phase modulator operating at visible wavelengths was developed and experimentally demonstrated. A visible-light silicon-nitride-based 300-mm-wafer foundry platform and a liquid-crystal integration process were developed and combined to leverage the birefringence of liquid crystal to actively tune the effective index of a silicon-nitride waveguide and induce a phase shift over the device length. The device was experimentally shown to achieve a 41π phase shift within ±2.4 V for a 500-μm-long modulator, which means that a 2π phase shifter would need to be only 24.4 μm long. When compared to traditional silicon-nitride phase modulators based on heaters, which are on the order of hundreds of microns to several millimeters long, this liquid-crystal-based device is one to two orders of magnitude shorter [59, 60]. This device is a compact and low-power solution to the challenge of integrated phase modulation in silicon nitride. This work paves the way for future low-power small-form-factor integrated systems at visible wavelengths for important application areas, such as dynamic displays and projection systems [1, 2], underwater optical communications and LiDAR sensors [8], and optogenetics

[15, 16, 19].

In the future, this work could be expanded upon to further improve the performance of the demonstrated integrated visible-light liquid-crystal-based phase modulator. For example, the optical simulations presented in this work could be expanded upon to include liquid-crystal material dynamics to explore the impact of the device cross section on the threshold voltage and driving voltage range and to investigate how different electrical driving schemes impact device performance. Furthermore, the response time and bandwidth of the device could be explored, and the device cross section, driving scheme, and liquid-crystal compound could be optimized to enable high-speed modulation (liquid-crystal cells commonly operate with response times varying from a hundred milliseconds [104] to several milliseconds with modified cell geometries and driving schemes [79,80,105–107], and there have even been demonstrations with response times reduced down to tens of nanoseconds using twisted-nematic liquid-crystal cells [108]). Additionally, the operating frequency of the device could be extended from the current red wavelength to green and blue wavelengths, especially given that 5CB liquid crystal has an even stronger birefringence at these shorter wavelengths. Finally, the current chip-scale liquid-crystal packaging process could be transferred to a wafer-scale foundry process to further improve the scalability of the device.

Chapter 6

Integrated Liquid-Crystal-Based Variable-Tap Amplitude Modulators

Integrated liquid-crystal-based demonstrations to date have largely focused on operation at infrared wavelengths [79–82,86,87]. As discussed in Ch. 5, we demonstrated the first visible-light liquid-crystal-based phase modulators [61,72]. Although amplitude modulation was achieved by directly integrating these liquid-crystal-based phase shifters into a Mach-Zehnder-interferometer configuration [61,72], this type of configuration has a large form factor since it requires a splitter at both the input and output of the device, phase shifters in each arm of the interferometer, and transitions connecting the liquid-crystal region to the splitters. While a long amplitude modulator may be acceptable for some systems and applications, many systems require compact amplitude modulators, such as integrated optical phased arrays that require dense integration for high fill factors [1,109].

In this chapter, we propose and experimentally demonstrate the first integrated visible-light liquid-crystal-based variable-tap amplitude modulators. These devices leverage the birefringence of liquid-crystal medium to actively tune the coupling coefficient between two waveguides and, hence, vary the amplitude of light coupled between these waveguides. First, in Sec. 6.1, we propose and develop the theory behind these integrated liquid-crystal-based variable-tap devices. Next, we outline the design procedure for how we determine the optimal waveguide widths and coupler

lengths of these devices to maximize amplitude modulation, with discussion regarding a tradeoff during the design process between achievable amplitude modulation and insertion loss. Then, in Sec. 6.2, we demonstrate experimental results of an example fabricated device that achieves strong amplitude modulation with a tradeoff of higher insertion loss, showing amplitude modulation with 15.4-dB tap-port extinction and 36% thru-to-tap-port switching within ±3.1 V for a 14.7-μm-long device, as well as a complementary example fabricated device that maintains low insertion loss with a slightly lower port switching of 13% for an 8-μm-long device, both at a 637-nm operating wavelength. These small-form-factor variable-tap devices provide a compact and low-power solution to integrated visible-light amplitude modulation and will enable high-density integrated visible-light systems in the future.

The following work was done in collaboration with Andres Garcia Coleto (MIT), Manan Raval (MIT), Thomas Dyer (SUNY Polytechnic), Christopher Baiocco (SUNY Polytechnic), and Jelena Notaros (MIT). This work has been published in [110].

6.1 Integrated Liquid-Crystal-Based Variable-Tap Amplitude Modulator Theory and Design

The liquid-crystal-based variable-tap amplitude modulators consist of two vertically-stacked 160-nm-thick silicon-nitride waveguides separated by 250 nm of silicon dioxide, 10 nm below a trench filled with liquid-crystal medium, with integrated metal electrodes on each side of the liquid-crystal-filled trench, as shown in Figs. 6.1. Light is coupled from a bus waveguide, directly beneath the liquid-crystal region, to a tap waveguide situated below the bus waveguide.

The amplitude of the light coupled into the tap waveguide depends on the coupling coefficient (affected by the mode overlap and difference in propagation constants) between the two waveguides. Since the bus waveguide is situated directly underneath the liquid-crystal-filled trench, the confinement and propagation constant of the bus waveguide mode are highly dependent on the refractive index of

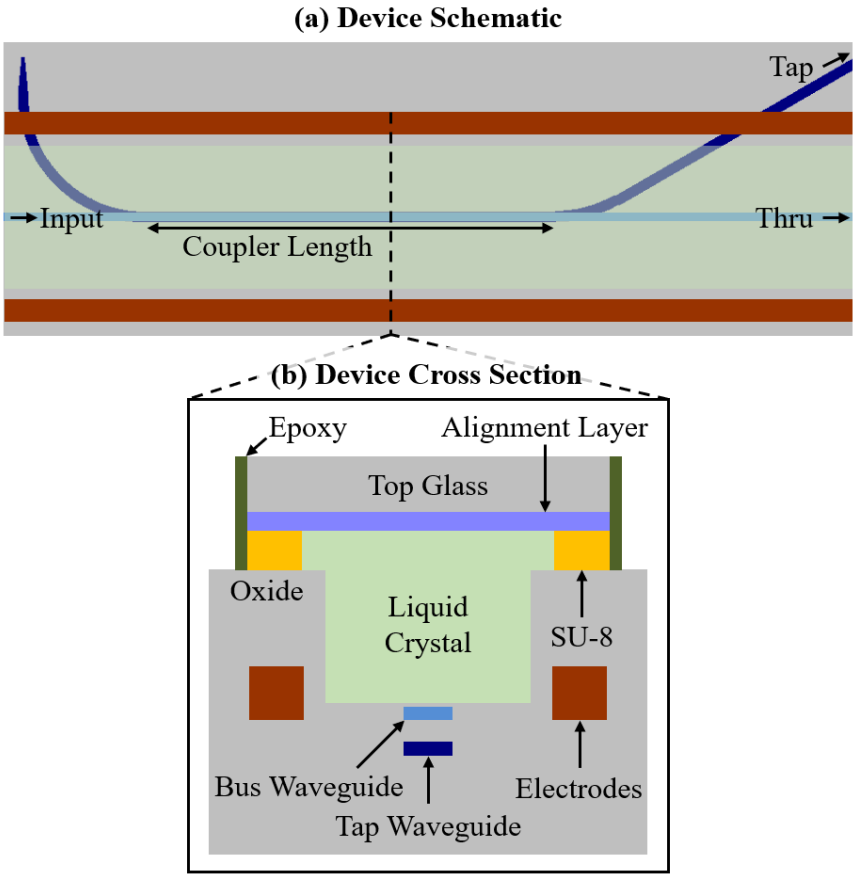

Figure 6.1: (a) Simplified top-view schematic of an integrated liquid-crystal-based variable-tap amplitude modulator (not to scale). (b) Simplified cross-sectional diagram of the liquid-crystal-packaged coupling region of the device, showing two vertically-stacked silicon-nitride waveguiding layers within silicon-dioxide cladding, electrodes, liquid-crystal-filled trench, SU-8 spacers, top glass with an alignment layer, and epoxy (not to scale).

the liquid-crystal medium. The liquid-crystal medium used here is 5CB (4'-Pentyl-4-biphenylcarbonitrile), which is a common commercially available liquid-crystal medium with ordinary and extraordinary refractive indices of 1.53 and 1.7, respectively, at the design wavelength of 637 nm. The liquid-crystal index can be tuned within this range by applying an electric field across the liquid-crystal region via the integrated electrodes [61]. As the liquid-crystal index increases, the mode in the bus waveguide becomes less confined and is pulled up into the liquid-crystal region, as shown in Fig. 6.2. For these variable-tap devices, we assume that the maximum refractive index is limited to 1.58 and 1.6 for a bus waveguide width of 320 nm and 420 nm,

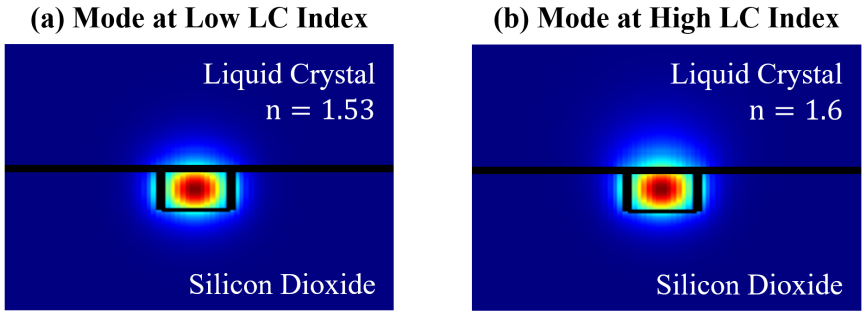

Figure 6.2: Simulated bus waveguide mode profiles at (a) the low liquid-crystal index of 1.53 and (b) the high liquid-crystal index of 1.6.

respectively, since the waveguide mode becomes poorly confined if the liquid-crystal refractive index is driven too high [61]. As we tune the liquid-crystal refractive index, the mode overlap and difference in propagation constants between the two waveguides change, resulting in amplitude modulation of the light coupled to the tap waveguide.

To ensure optimal amplitude modulation, the bus waveguide width, tap waveguide width, and coupler length must be chosen properly during the design process. As the first step in this design process, we select a bus waveguide width. As an example, we select a 320-nm-wide bus waveguide for this discussion. Second, we choose the coupler length such that no light is coupled into the tap waveguide at the high liquid-crystal refractive index (to take advantage of the mode in the bus waveguide pulling up into the liquid-crystal medium at the higher index). To determine the appropriate coupler length, we simulate the transmission to the tap port versus coupler length at the high liquid-crystal refractive index for a variety of tap waveguide widths. As an example, we show simulation results of the transmission to the tap port versus coupler length for a 320-nm-wide bus waveguide and three different tap waveguide widths in Fig. 6.3a. For instance, for a bus waveguide width of 320 nm and a tap waveguide width of 400 nm, the optimal coupler length is determined to be 14.7 μm. We follow this simulation procedure to determine the appropriate coupler length for a variety of tap waveguide widths, as shown in Fig. 6.3b.

Third, we choose the tap waveguide width to maximize amplitude modulation. To determine the optimal tap waveguide width, for each tap waveguide width and corresponding optimal coupler length, we simulate the transmission to the tap port

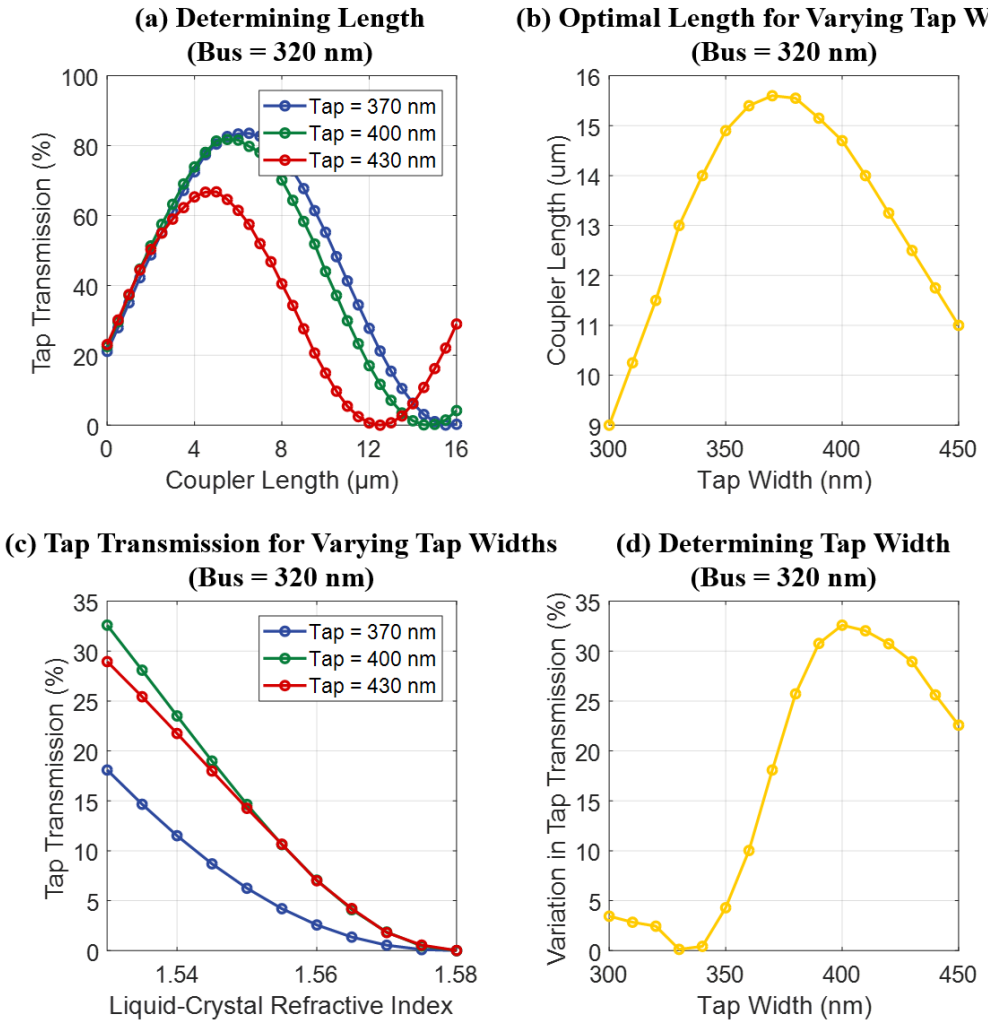

Figure 6.3: Simulation results for the integrated liquid-crystal-based variable-tap amplitude modulators, outlining the design procedure. (a) Tap transmission as a function of coupler length for a bus waveguide width of 320 nm and three tap waveguide widths at the high liquid-crystal refractive index of 1.58 (used to determine the optimal coupler length for each tap waveguide width). (b) Optimal coupler length as a function of tap waveguide width for a bus waveguide width of 320 nm. (c) Tap transmission as a function of liquid-crystal refractive index for a bus waveguide width of 320 nm and three tap waveguide widths. (d) Variation in tap transmission as a function of tap waveguide width for a bus waveguide width of 320 nm (used to choose the optimal tap waveguide width).

as a function of liquid-crystal refractive index. As an example, simulation results showing transmission to the tap port versus liquid-crystal refractive index for a 320-nm-wide bus waveguide, three different tap waveguide widths, and corresponding optimal coupler lengths are shown in Fig. 6.3c. For instance, for a bus waveguide

width of 320 nm, a tap waveguide width of 400 nm, and a coupler length of 14.7 μm, the transmission to the tap port varies from 33% to 0%. We follow this simulation procedure to determine the variation in coupling to the tap port for a variety of tap waveguide widths, as shown in Fig. 6.3d. These results are then used to choose the tap waveguide width that maximizes amplitude variation. For example, for a 320-nm-wide bus waveguide, a tap waveguide width of 400 nm achieves the most amplitude variation, with simulation results showing the transmission to the tap and thru ports as a function of liquid-crystal refractive index of this final optimal device design shown in Fig. 6.4a.

This device with a bus waveguide width of 320 nm can achieve strong thru-to-tap-port switching with a tradeoff of reduced mode confinement and, as a result, higher propagation loss. On the other hand, a device with a wider bus waveguide width has the advantage of supporting a more confined optical mode with lower propagation loss, with a tradeoff of less port switching. The same design procedure outlined above was then applied to design a complementary device with a wider bus waveguide width of 420 nm, which results in an optimal tap waveguide width and coupler length of 370 nm and 8 μm, respectively, with simulation results showing the transmission to the tap and thru ports as a function of liquid-crystal refractive index of this device shown

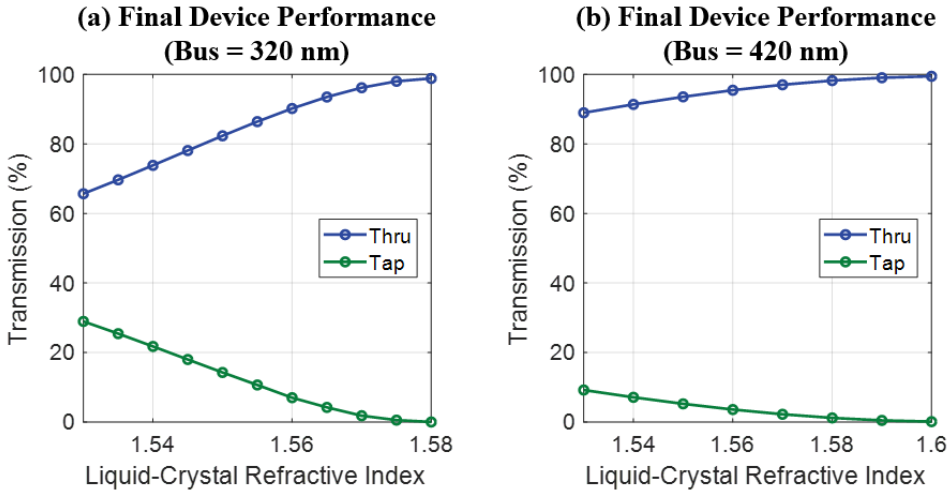

Figure 6.4: Transmission to the thru and tap ports as a function of liquid-crystal refractive index for the final optimal device design for a bus waveguide width of (a) 320 nm and (b) 420 nm.

in Fig. 6.4b, demonstrating transmission to the tap port varying from 9% to 0%.

6.2 Integrated Liquid-Crystal-Based Variable-Tap Amplitude Modulator Experimental Setup and Results

The integrated liquid-crystal-based variable-tap modulators were fabricated in a CMOS-compatible 300-mm wafer-scale silicon-photonics process at the State University of New York Polytechnic Institute's (SUNY Poly) Albany NanoTech Complex, as described in Sec. 2.1. The developed visible-light photonics platform consists of two 160-nm-thick silicon-nitride waveguiding layers separated by 250 nm of silicon dioxide, an 800-nm-deep and 5-μm-wide silicon-dioxide trench spaced 60 nm above the top waveguiding layer for holding the liquid crystal, an 820-nm-thick metal layer for electrical routing and contact pads, and a dicing trench to create a smooth chip facet for fiber edge coupling.

The fabricated photonic wafer then underwent a dicing process to obtain individual chips that, in turn, underwent a back-end fabrication process at MIT to package the chips with liquid crystal, as described in Sec. 4.4. In summary, this packaging process consists of four steps: (i) performing a dry etch to bring the bottom of the trench closer to the waveguide; (ii) patterning an SU-8 photoresist spacer layer; (iii) epoxying a glass chip with an alignment layer on top of the SU-8 spacer layer; and (iv) injecting liquid crystal into the formed cavity, to achieve a final cross section as shown in Fig. 6.1b. A micrograph of one of the fabricated variable-tap devices is shown in Fig. 6.5a. Further details on wafer fabrication and liquid-crystal packaging are provided in [61, 73].

To characterize the fabricated devices, a 637-nm-wavelength diode laser was coupled onto the chip, electronic probes were used to apply a 10-kHz square wave with a variable peak voltage across the electrodes, and the optical power out of the thru and tap output ports was monitored using a power meter. A photograph of the ex-

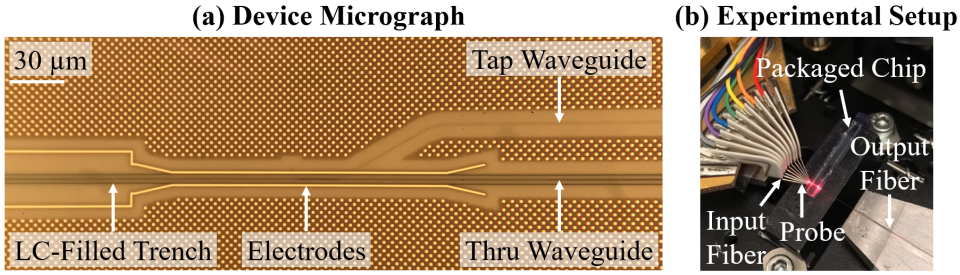

Figure 6.5: (a) Micrograph of a fabricated integrated liquid-crystal-based variable-tap amplitude modulator, showing the liquid-crystal-filled cavity and trench, integrated electrodes, and the tap and thru waveguides. (b) Photograph of the experimental setup, showing a liquid-crystal-packaged photonic chip, input and output optical fibers, and electrical probes.

perimental setup, showing the liquid-crystal-packaged chip, input and output fibers, and electrical probes, is shown in Fig. 6.5b. A top-view schematic of one of the fabricated on-chip test structures that are used to characterize our devices, highlighting key integrated components and the driving scheme, is shown in Fig. 6.6.

We experimentally demonstrate two example fabricated variable-tap devices, one device with a 320-nm bus waveguide width that can achieve strong thru-to-tap-port switching with a tradeoff of higher insertion loss, as well as a complementary device with a 420-nm bus waveguide width that maintains low insertion loss with slightly less port switching.

Experimentally measured results of the fabricated variable-tap device with a bus waveguide width of 320 nm are shown in Fig. 6.7. The percentage of power in both the thru and tap ports of the device normalized relative to the total power is shown

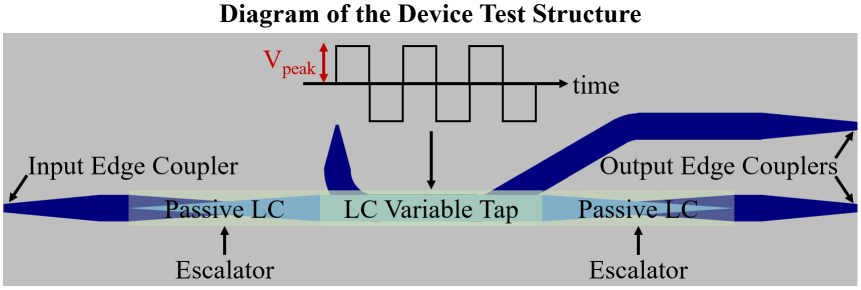

Figure 6.6: Simplified top-view diagram of the device test structure, depicting the input and output edge couplers, vertical-transition escalators, variable-tap amplitude modulator, and voltage driving scheme (not to scale).

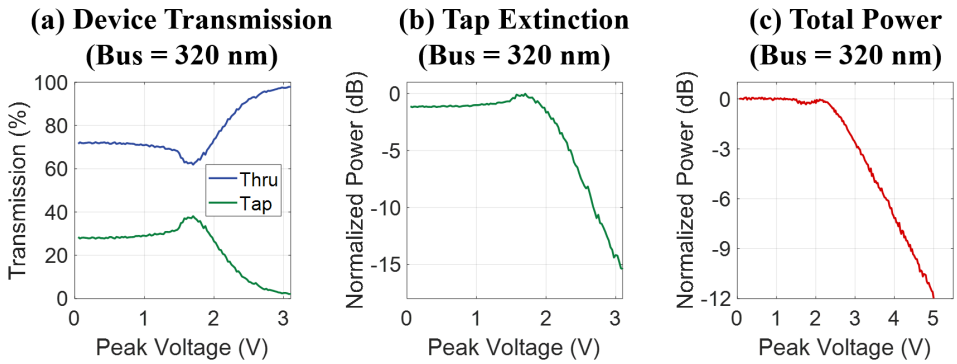

Figure 6.7: Experimental results for a fabricated device with a 320-nm-wide bus waveguide, showing (a) the normalized power in the tap and thru ports relative to the total power versus peak voltage of the 10-kHz square wave applied to the device, (b) the normalized power in the tap port versus peak voltage, highlighting the extinction ratio, and (c) the normalized total power in the thru and tap ports versus peak voltage.

in Fig. 6.7a, with an overall port switching of 36% from the tap to the thru port, which closely matches simulation results. The normalized measured power in the tap port is shown in Fig. 6.7b, demonstrating an extinction ratio of 15.4 dB. To characterize the insertion loss through the device, the total power in both the thru and tap ports is shown in Fig. 6.7c; given these results, we limit the maximum applied peak voltage to ±3.1 V when characterizing the device to bound the insertion loss to 3 dB. Overall, this 14.7-μm-long device can achieve amplitude modulation with 15.4-dB tap-port extinction and 36% thru-to-tap-port switching within only ±3.1 V; however, it undergoes up to 3-dB insertion loss by this point. For certain applications, achieving more modulation at the cost of higher loss is acceptable; however, for other applications the opposite is true, where low loss might be necessary, for which a variable-tap device that maintains lower loss could be useful.

To demonstrate this tradeoff, we also experimentally characterized the fabricated variable-tap device with a bus waveguide width of 420 nm, with experimentally measured results shown in Fig. 6.8. This 8-μm-long device can achieve amplitude modulation with 12.6-dB extinction in the tap power (Fig. 6.8b) and switching of 13% between the two ports (Fig. 6.8a) within ±10 V. Although the variation and extinction of the power in the tap port are less significant for this device, the insertion loss

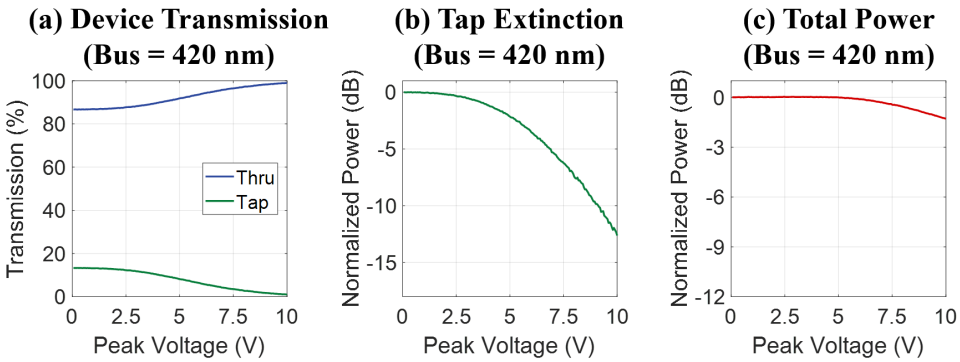

Figure 6.8: Experimental results for a fabricated device with a 420-nm-wide bus waveguide, showing (a) the normalized power in the tap and thru ports relative to the total power versus peak voltage of the 10-kHz square wave applied to the device, (b) the normalized power in the tap port versus peak voltage, highlighting the extinction ratio, and (c) the normalized total power in the thru and tap ports versus peak voltage.

is significantly lower, with only 1.3-dB loss within this voltage range (Fig. 6.8c). This demonstrates the tradeoff between achievable amplitude variation and insertion loss for these devices.

6.3 Conclusion

In this work, we proposed and experimentally demonstrated the first integrated visible-light liquid-crystal-based variable-tap amplitude modulators. These devices leverage the birefringence of liquid-crystal medium to actively tune the coupling coefficient between two waveguides and, hence, vary the amplitude of light coupled between these waveguides. First, we proposed and developed the theory behind these integrated liquid-crystal-based variable-tap devices. Next, we outlined the design procedure for how we determine the optimal waveguide widths and coupler lengths of these devices to maximize amplitude modulation, with discussion regarding a tradeoff during the design process between achievable amplitude modulation and insertion loss. Then, we summarized the fabrication and liquid-crystal packaging procedure for these devices. Finally, we demonstrated experimental results of an example fabricated device that achieves strong amplitude modulation with a tradeoff of higher

insertion loss, showing amplitude modulation with 15.4-dB tap-port extinction and 36% thru-to-tap-port switching within ±3.1 V for a 14.7-μm-long device, as well as a complementary example fabricated device that maintains low insertion loss with a slightly lower port switching of 13% for an 8-μm-long device, both at a 637-nm operating wavelength.

These small-form-factor variable-tap devices provide a compact and low-power solution to integrated visible-light amplitude modulation. They will enable future high-density integrated systems at visible wavelengths spanning a variety of applications, such as neural probes [15, 16, 19], displays [1, 2], underwater optical communications [9, 111], and trapped-ion systems [10, 11, 14].

Chapter 7

Liquid-Crystal-Based Cascaded Integrated Optical Phased Arrays

As described in Sec. 1.2, integrated optical phased arrays (OPAs) enable emission and non-mechanical steering of beams emitted from compact, millimeter-scale, fully integrated, planar, solid-state chips [1, 2, 42, 44, 46, 48, 49, 51–53, 56, 58, 112], providing advantages in form factor, simplified assembly, and integrated control over other beam-steering technologies, such as spatial light modulators. Over the years, they have been used in demonstrations for many impactful applications, such as light detection and ranging (LiDAR) and free-space optical data communications [42, 56]. However, due to these initial application areas, OPAs have mostly been limited to implementations at infrared wavelengths [42, 46, 48, 49, 51–53, 56, 58]. Visible-light integrated OPAs have been largely underdeveloped.

However, there are many potential wide-reaching applications that require visible-light operation, as discussed in Sec. 1.1. Recently, visible-light integrated OPAs have been demonstrated in silicon-nitride platforms [1, 2, 44, 112]; however, they have been mostly limited to passive systems that are not electrically tunable [1, 2, 44], which limits practical use for many applications. An active visible-light OPA was recently demonstrated; however, it utilized long and power-inefficient heater-based modulators [112]. These modulator disadvantages are due to the low thermo-optic coefficient of silicon nitride, which results in traditional heater-based silicon-nitride

modulators on the order of hundreds of microns to millimeters long [59,60]. As such, these heater-based modulators are insufficient for OPA systems, which require power-efficient modulators to enable scaling to large aperture sizes and compact modulators to enable intricate routing schemes and tight antenna pitches. To address these modulator limitations, we have shown the first integrated visible-light liquid-crystal-based (LC-based) modulators (described in Ch. 5 and Ch. 6), which provide a compact and power-efficient solution to visible-light modulation on a chip.

In this chapter, by leveraging these LC-based phase modulators, we demonstrate the first LC-based integrated OPA and use it to enable visible-light beam forming and steering. In Sec. 7.1, we develop an LC-based cascaded OPA architecture and design the corresponding necessary devices, including vertical-layer transitions, LC-based phase modulators, evanescent taps, and grating-based antennas. In Sec. 7.2, we fabricate this OPA system and use it to experimentally demonstrate beam steering at a 632.8-nm wavelength with a $0.4^\circ \times 1.6^\circ$ power full-width at half maximum and 7.2° beam-steering range within ± 3.4V.

The following work was done in collaboration with Manan Raval (MIT), Michael R. Watts (MIT), and Jelena Notaros (MIT). This work has been published in [109].

7.1 Liquid-Crystal-Based Cascaded-Integrated-Optical-Phased-Array Architecture

The integrated OPA consists of an LC-based cascaded-phase-shifter architecture that linearly controls the relative phase applied to an array of antennas, as shown in Fig. 7.1a.

At the input, an on-chip inverse-taper edge coupler couples light from an off-chip laser into an on-chip single-mode silicon-nitride waveguide. A 100-μm-long escalator device (an adiabatic layer-transition structure) then couples the input light from the single-mode waveguide into a vertically stacked silicon-nitride bus waveguide that is directly below an LC-filled trench (Fig. 7.1b). This vertical-transition escalator

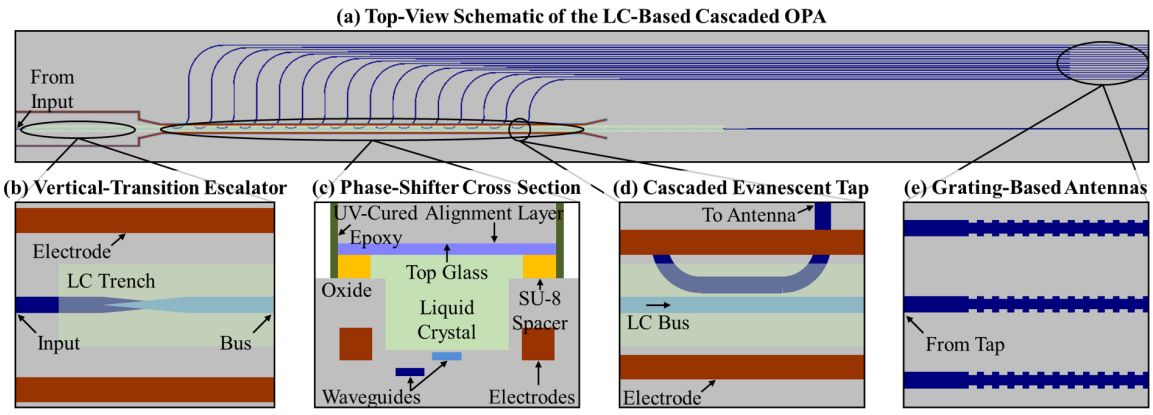

Figure 7.1: (a) Top-view simplified schematic of the LC-based cascaded OPA. (b) Top-view simplified schematic of the vertical-transition escalator from the bottom waveguide to the top waveguide directly underneath the LC region. (c) Cross-sectional simplified diagram of the phase shifter after the in-house post-processing packaging steps. (d) Top-view simplified schematic of a cascaded evanescent tap that couples light from the upper bus waveguide to the bottom tap waveguide. (e) Top-view schematic of the grating-based antennas. (Not to scale.)

is utilized to minimize loss when transitioning into the LC region, since a direct-interface transition would result in increased loss, as seen in simulation results shown in Fig. 5.9.

Next, evanescent tap couplers, placed with a pitch of 20 μm and with increasing coupling lengths, uniformly distribute the light from the bus waveguide to 16 vertically stacked and horizontally offset tap waveguides (Fig. 7.1d). This horizontal offset was implemented to minimize the effect of fabrication variation on coupling (with simulation results confirming minimal impact on device performance for ±10 nm variation in waveguide offset). Simulation results for an evanescent tap as a function of coupler length are shown in Fig. 7.2b, which we use to determine the required coupler lengths along the LC-based phase-shifting bus region to ensure uniform light is coupled to each of the 16 tap waveguides.

These tap waveguides then route to 16 grating-based 400-μm-long antennas with uniform perturbations and a 2-μm pitch to emit the light out of the surface of the chip (Fig. 7.1e). Simulation results of the scattering strength for a grating-based antenna as a function of perturbation width is shown in Fig. 7.2c. We choose a perturbation width of 57 nm, resulting in 98% of the light scattered by the end of the 400-μm-long

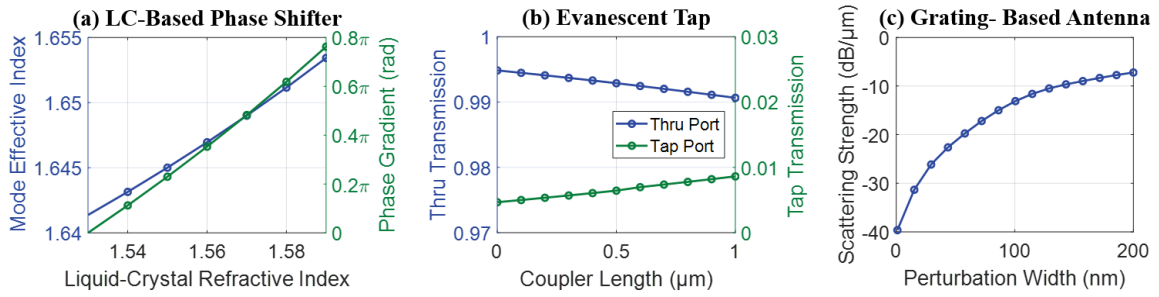

Figure 7.2: Simulation results showing (a) the optical mode effective index and the phase gradient applied across the antennas due to the LC-based phase shifter as a function of LC refractive index, (b) transmission into the thru (blue) and tap (green) ports of an evanescent tap as a function of coupler length, and (c) scattering strength of a grating-based antenna versus perturbation width.

antenna.

To enable one-dimensional far-field beam steering, the system utilizes the birefringence of LC medium to enable cascaded phase control to the array of antennas. As described in more detail in Sec. 4.2, in a nematic LC medium, the index of refraction varies based on the orientation of the LC molecules with respect to the propagation direction of the light. Furthermore, nematic LC molecules self-align to one another, and their directors align to an external electric field. Thus, by applying an electric field across the LC region to orient the molecules in the direction of the field, the index can be actively tuned, resulting in a linear phase shift to the antennas. To enable this functionality, the LC-based phase-shifting region consists of a silicon-nitride bus waveguide to weakly confine and guide the light, LC medium deposited into an oxide trench to enable strong interaction between the optical mode and the LC medium, metal electrodes on each side of the LC-filled trench for applying an electric field across the LC region, and a top glass chip with a mechanical alignment layer on the underside to anchor the LC molecules. A cross-sectional diagram of the phase-shifting region is shown in Fig. 7.1c and additional details on the LC phase shifter are discussed in Ch. 5. Simulation results of the optical mode effective index and phase gradient applied across the antennas as a function of the LC refractive index are shown in Fig. 7.2a. The LC medium used here is 5CB (4'-Pentyl-4-biphenylcarbonitrile), which is a common commercially available LC medium with ordinary and extraordi-

nary refractive indices of 1.53 and 1.7, respectively, at the design wavelength of 632.8 nm [97,98]; in this system, we assume that the maximum refractive index is limited to 1.59, since the waveguide mode becomes poorly confined past this point.

7.2 Liquid-Crystal-Based Cascaded-Integrated-Optical-Phased-Array Experimental Setup and Results

The LC-based cascaded integrated OPA was fabricated in a CMOS-compatible 300-mm wafer-scale silicon-photonics process at the State University of New York Polytechnic Institute's (SUNY Poly) Albany NanoTech Complex (described in Ch. 2). The final fabricated cross section of the system, as received from SUNY Poly, consists of two 160-nm-thick SiN waveguiding layers, separated by 250 nm of silicon dioxide, an 800-nm-deep and 5-μm-wide silicon-dioxide trench vertically spaced 60 nm above the top waveguiding layer, 820-nm-thick and 1-μm-wide metal electrodes on each side of the trench, and a smooth chip facet for edge coupling. We then diced the fabricated photonic wafer and performed a chip-scale LC-packaging process at MIT (described in Sec. 4.4). A photograph of the LC-packaged chip is shown in Fig. 7.3, with a micrograph of the fabricated OPA in the inset.

To experimentally characterize the fabricated integrated OPA, we coupled a 632.8-

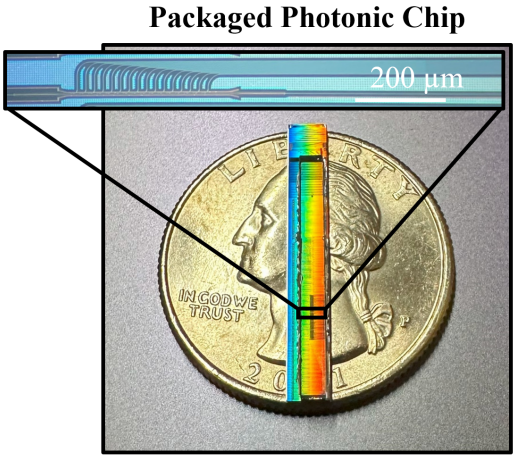

Figure 7.3: Photograph of a fabricated and LC-packaged photonic chip with a micrograph of the OPA in the inset.

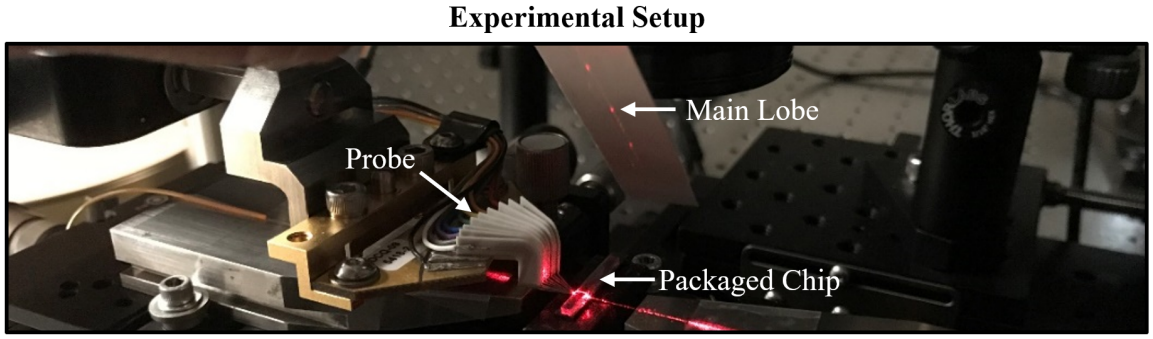

Figure 7.4: Photograph of the experimental setup, showing the packaged photonic chip and emitted radiation pattern.

nm-wavelength helium-neon laser onto the chip via an optical fiber. An optical system, comprised of an objective, a lens to perform a Fourier transform, and a camera, was used to image the far field of the OPA. A photograph of the experimental setup, showing the emitted radiation pattern on a piece of cardstock, is shown in Fig. 7.4.

The experimentally measured far-field radiation pattern is shown in Fig. 7.5. Experimentally measured cross-sectional cuts of the far-field main lobe, in both the antenna and array dimensions, are shown in Fig. 7.6a. As expected, the array forms a beam in the far field with a $0.4° \times 1.6°$ power full-width at half maximum, 8-dB side-lobe suppression, and second-order grating lobes at $\pm 18.8°$.

The propagation loss was experimentally measured using two suites of loss test structures and was found to be approximately 0.6 dB/mm for the nominal silicon-

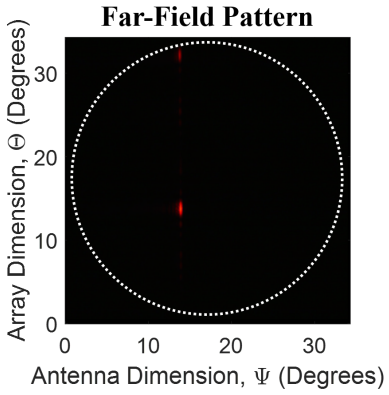

Figure 7.5: Experimentally measured far-field radiation pattern, showing the main lobe and a grating lobe.

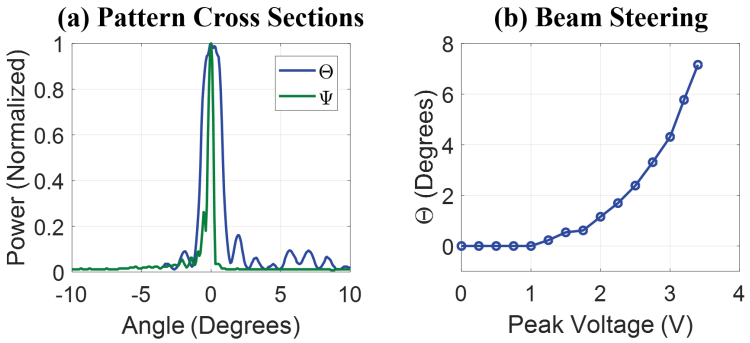

Figure 7.6: Experimentally measured (a) cross-sectional cuts of the far-field main lobe, in both the array (blue) and antenna (green) dimensions and (b) electrically controlled beam steering of the main lobe in the array dimension when a square wave with a varying peak voltage is applied across the LC-based phase shifter.

nitride waveguides and 1 dB/mm for the LC-based phase shifter. The overall insertion loss from the on-chip input waveguide to the main lobe emitted by the OPA is approximately 25 dB, which can be improved by utilizing strong evanescent taps instead of the weak taps used in this initial demonstration and by reducing the antenna pitch to decrease the power loss to the higher-order grating lobes.

Next, to demonstrate beam steering, we used electronic probes to contact the integrated electrodes. A 10-kHz square wave was applied across the electrodes of the LC phase shifter. We varied the peak voltage of this applied square wave to tune the phase gradient applied across the antennas and, hence, steer the formed beam in the array dimension, θ. As shown in Fig. 7.6b, the OPA system enables 7.2° of visible-light beam steering within ±3.4V.

7.3 Conclusion

This chapter presented the first proposal and demonstration of liquid-crystal-based integrated optical phased arrays. We developed a cascaded integrated OPA architecture with a compact and power-efficient LC-based phase-shifting region and used it to enable visible-light beam forming and steering. We demonstrated vital device design, including vertical-layer transitions, LC-based phase modulators, evanescent taps, and grating-based antennas. We fabricated this OPA system and used it to ex-

perimentally demonstrate beam steering at a 632.8-nm wavelength with a $0.4^\circ \times 1.6^\circ$ power full-width at half maximum and 7.2° beam-steering range within ± 3.4V.

In the future, this LC-based OPA could be scaled up to a larger aperture demonstration [44, 58], and could be implemented using other architecture configurations, such as a splitter-tree-based OPA architecture [42, 56] or a cascaded architecture with multiple electrodes distributed along the LC region for fine-tuned phase control [46, 48] (which could account for fluctuations in performance from fabrication variation, as discussed in [113, 114]). Furthermore, the LC-based phase-shifter cross section, driving scheme, and LC compound could be optimized to enable high-speed beam steering. Additionally, the operating frequency of the OPA could be extended from the current red wavelength to green and blue wavelengths.

This OPA system provides a promising solution to the challenge of integrated visible-light beam forming and steering, with many impactful far-reaching applications, including underwater wireless communications, displays, neural probes, trapped-ion systems, and 3D printers.

Chapter 8

Active VIPER Display

Next, the VIPER display was enhanced, from a passive display that generates a single predetermined holographic image (described in Ch. 3), to an active display that generates real-time-programmable holographic images and videos. Similar to the passive display, the active version of the VIPER display is based on a 2D grid of coherent visible-light integrated optical phased arrays that act as the pixels in the display; however, to enable this active display, an active version of the VIPER pixel with dynamic amplitude, absolute phase, and phase gradient encoding needed to be developed first.

In this chapter, the steps towards realizing the active VIPER display will be reviewed. First, a single active VIPER pixel, which is a key building block for the full VIPER display, will be developed and demonstrated in Sec. 8.1; this single active VIPER pixel is a culmination of the liquid-crystal-based modulators and systems described in Ch. 5–7. Next, using this active pixel as a building block, the architecture for the full active VIPER display is developed and used to demonstrate initial dynamic video display functionality in Sec. 8.2. Finally, the VIPER display is designed to be heterogeneously integrated with a custom thin-film-transistor electronics backplane in the future to enable future scaling to a large-scale video-hologram demonstration with multi-wavelength RGB functionality, which is outlined in Sec. 8.3.

The following work was done in collaboration with Manan Raval (MIT), Michael R. Watts (MIT), and Jelena Notaros (MIT).

8.1 Active Liquid-Crystal-Based Optical-Phased-Array Pixel

First, a key building block of the active VIPER display - a single active VIPER pixel - needed to be developed. The active VIPER pixel mimics the passive VIPER pixel described in Sec. 3.1 and shown in Fig. 3.2, with the exception that the active pixel consists of actively tunable modulators instead of passive components.

One challenge in implementing dynamic control of amplitude and phase for the active VIPER pixel is traditionally inefficient integrated visible-light modulators, due to material constraints of silicon nitride. As a solution, nematic liquid-crystal material, with a strong birefringence in the visible spectrum, is integrated into the VIPER platform and used to enable novel phase and amplitude modulators for dynamic encoding of the active VIPER pixel. The liquid-crystal integration and packaging is discussed in Ch. 4, the liquid-crystal-based phase modulators are described in Ch. 5, the liquid-crystal-based amplitude modulators are discussed in Ch. 6, and the liquid-crystal-based cascaded optical phased arrays are discussed in Ch. 7.

8.1.1 Optical-Phased-Array-Pixel Architecture

These liquid-crystal-based phase and amplitude modulators are utilized to enable the compact active VIPER pixel. As shown in Fig. 8.1, the pixel contains three individual liquid-crystal-based devices: (1) a liquid-crystal-based phase modulator on the row waveguide to modulate the *absolute phase* of the light emitted by each pixel, (2) a liquid-crystal-based variable tap to modulate the *amplitude* of light coupled from the row waveguide to each pixel bus, and (3) a liquid-crystal-based pixel bus with 8 compact cascaded pixel-bus-to-antenna taps to uniformly distribute light from the pixel bus to 8 grating-based antennas and to modulate the linear *phase gradient* of the light emitted by each pixel. As shown in Fig. 8.1, the three liquid-crystal-based devices share a common ground electrode to simplify electrical routing, while the three devices have individual signal electrodes to enable independent control.

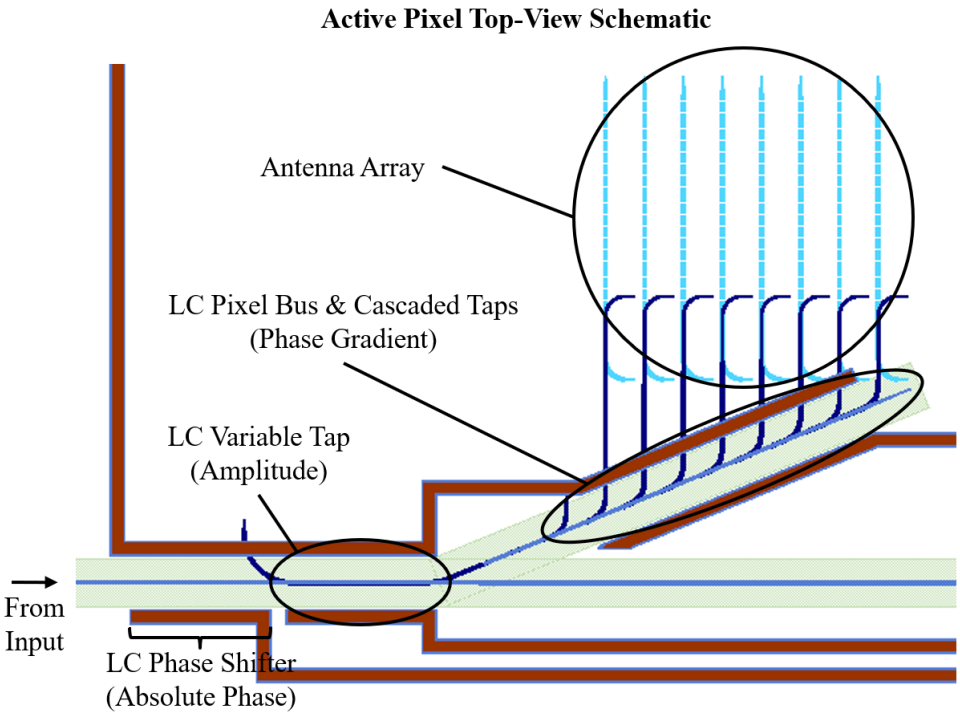

Figure 8.1: Schematic of a single optical-phased-array-based pixel of the active VIPER display showing major components, including the liquid-crystal-based phase modulator for pixel absolute phase encoding, liquid-crystal-based variable tap for pixel amplitude encoding, and liquid-crystal-based pixel bus with compact cascaded pixel-bus-to-antenna taps for pixel phase gradient encoding.

As shown in the cross-sectional diagram in Fig 8.2, the antennas are implemented in two vertically-stacked silicon-nitride layers to enable efficient unidirectional emission [68,115], such that the display emits only in the direction of the user's eye rather than outwards into the environment, and to enable compact overlapping of pixels in the display for a high fill factor.

8.1.2 Optical-Phased-Array-Pixel Experimental Setup and Results

The active VIPER pixel was fabricated at the SUNY Poly Albany NanoTech Complex (platform and fabrication process described in Ch. 2). The resulting chip, as fabricated in this custom 300-mm-diameter wafer-scale silicon-photonics process, consists of four silicon-nitride waveguiding layers recessed within silicon-dioxide cladding, a

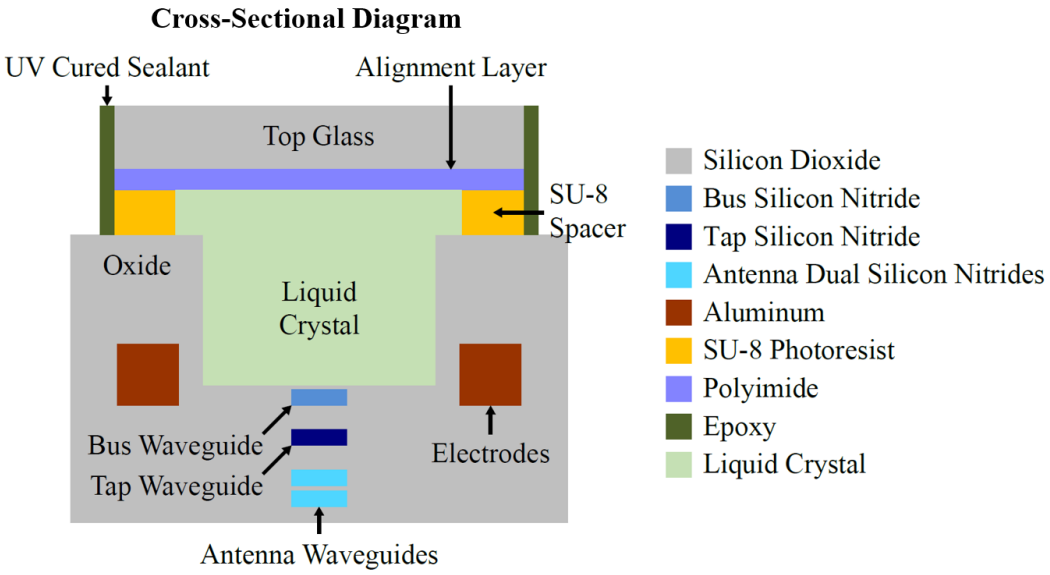

Figure 8.2: Simplified cross-sectional schematic of the active VIPER pixel consisting of two silicon-nitride "antenna" waveguides, a silicon-nitride "tap" waveguide, and a silicon-nitride "bus" waveguide recessed within silicon dioxide below a liquid-crystal-filled trench with integrated electrodes on each side (not to scale).

metal layer for electrical routing and contact pads, an empty trench layer for holding the liquid crystal, and a dicing trench for fiber coupling. Further chip-scale liquid-crystal packaging was done at the Massachusetts Institute of Technology fabrication facilities as back-end steps (described in Sec. 4.4). A micrograph of a fabricated active VIPER pixel is shown in Fig. 8.3. This micrograph shows the input bus waveguide, liquid-crystal-based phase modulator, liquid-crystal-based variable-tap amplitude modulator, liquid-crystal-based phase gradient with evanescent taps,

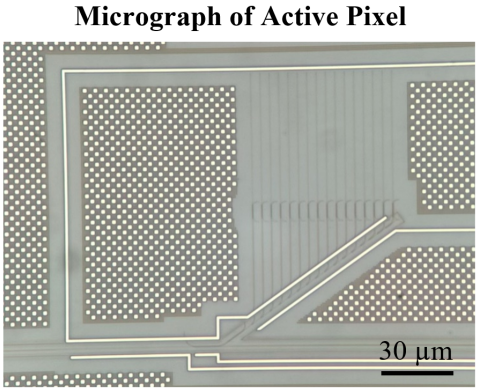

Figure 8.3: Micrograph of an example fabricated active VIPER pixel.

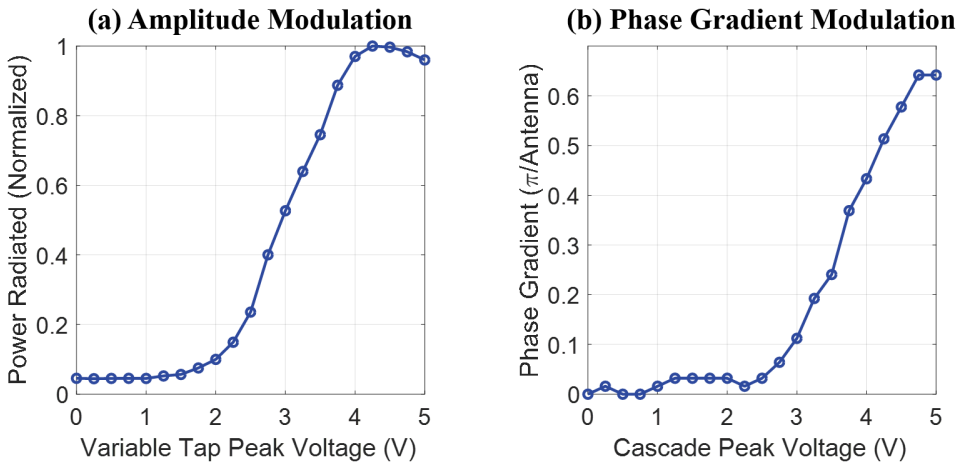

Figure 8.4: Experimental results for a single active VIPER pixel showing (a) normalized power radiated out of the pixel versus applied variable tap peak voltage and (b) pixel phase gradient shift versus applied cascade peak voltage.

layer transitions to the dual-silicon-nitride grating-based antennas, and electrodes for electrical routing.

To characterize the fabricated active VIPER pixel, electronic probes were used to apply a 10-kHz square wave with variable peak voltage to each of the active liquid-crystal-based components in the pixel. As shown in Fig. 8.4a–b, amplitude modulation from the "off" state to the "on" state with a contrast ratio of approximately 20:1 was achieved within ±4.5V in a 9-μm-long device, and phase gradient modulation of 0.65π per antenna was achieved within ±4.75V.

Near-field images of a single active pixel turned "off" (corresponding to a variable tap voltage of 0 V) and turned "on" (corresponding to a variable tap voltage of ±5 V), are shown in Fig. 8.5a and Fig. 8.5b, respectively.

This demonstration of a compact and efficient active VIPER pixel represents an important step towards developing the full VIPER display, successfully confirming the performance of the integrated liquid-crystal-based phase and amplitude modulators, the functionality of the active pixel, and the path towards scaling to the active display.

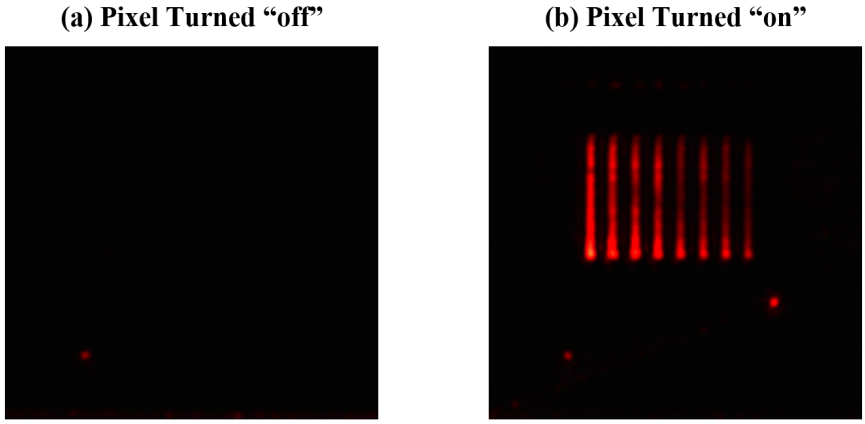

Figure 8.5: Experimental results for a single active VIPER pixel showing (a) the pixel turned “off”, corresponding to a peak voltage of 0 V and (b) the pixel turned “on”, corresponding to a peak voltage of 10 V.

8.2 Active VIPER Display

Next, by leveraging the active VIPER pixel discussed in Sec. 8.1, an active version of the VIPER display that generates real-time-programmable holographic images and videos was designed, and a proof-of-concept active 4x4 pixel display was fabricated and experimentally demonstrated.

8.2.1 Active VIPER Display Architecture

The active VIPER display is based on a 2D grid of actively-tunable coherent visible-light integrated optical phased arrays that act as the pixels in the display (i.e. the active VIPER pixels described in Sec. 8.1), as shown in Fig. 8.6, with a single pixel highlighted for clarity. At the input of the system, an on-chip inverse-taper edge coupler couples light from an off-chip laser into an on-chip single-mode silicon-nitride waveguide. A multi-mode-interference splitter tree with $\log_2$N stages evenly distributes the input power to N rows with a final row pitch of 32 μm. Along each row, N compact active VIPER pixels are cascaded with a pixel pitch of 32 μm for a total of N×N pixels arranged in a 2D grid with each pixel having dynamic amplitude, absolute phase, and phase gradient encoding. This cascaded architecture allows for independent pixel-to-pixel calibration. As shown in Fig. 8.6, the developed

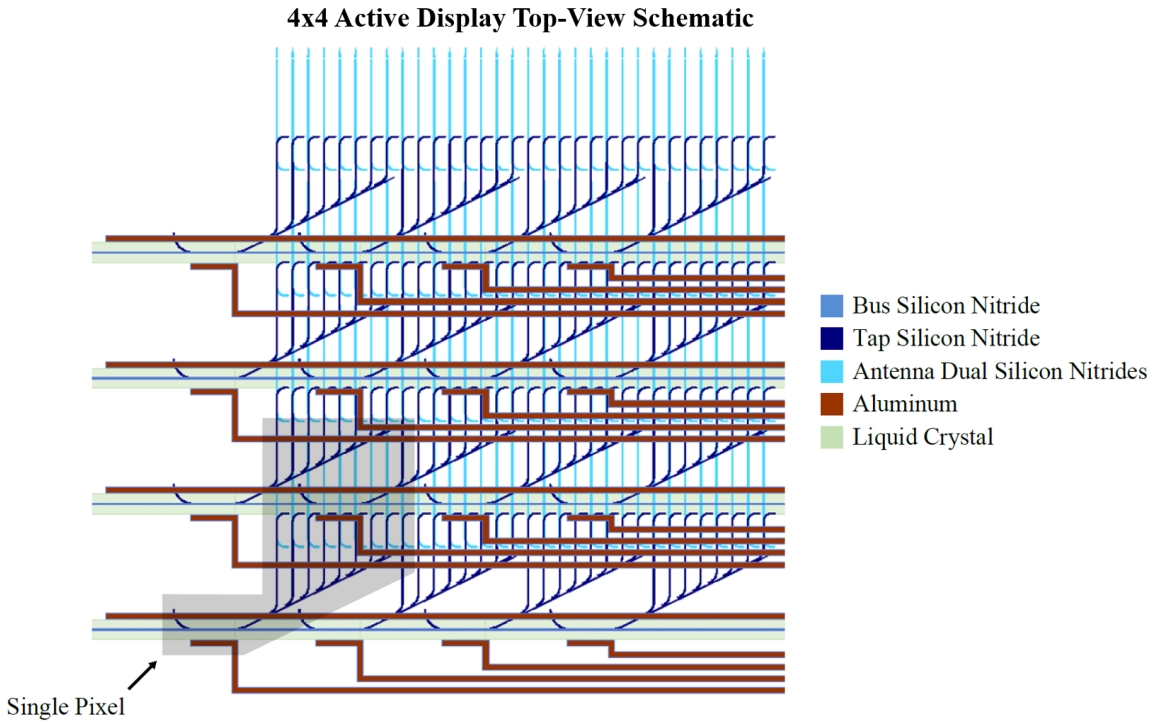

Figure 8.6: Partial schematic of the active VIPER display with 4×4 pixels, 32 μm pixel pitch, 8 antennas per a pixel, and 4 μm antenna pitch (with one pixel within the display highlighted in grey for clarity).

pixel architecture, compact modulators, and multi-layer platform allow for compact cascading and vertical overlapping of the pixels to enable a tight pitch and high fill factor for the display. For example, the antennas of the pixels in the 4^{th} (bottom) row are vertically underneath the modulators for the pixels in the 3^{rd} row.

8.2.2 Active VIPER Display Experimental Setup and Results

As an initial demonstration of the video functionality of the active VIPER display, a 4x4 pixel prototype of the active display was fabricated and packaged in the custom 300-mm-diameter wafer-scale silicon-photonics process developed for the active VIPER pixel. A micrograph of a fabricated 4x4 pixel display is shown in Fig. 8.7. A transmission-electron-microscopy cross-sectional image of a section of the active display is shown in Fig. 8.8, showing the bus waveguide layer, tap waveguide layer, dual-layer antennas, electrodes, and trench.

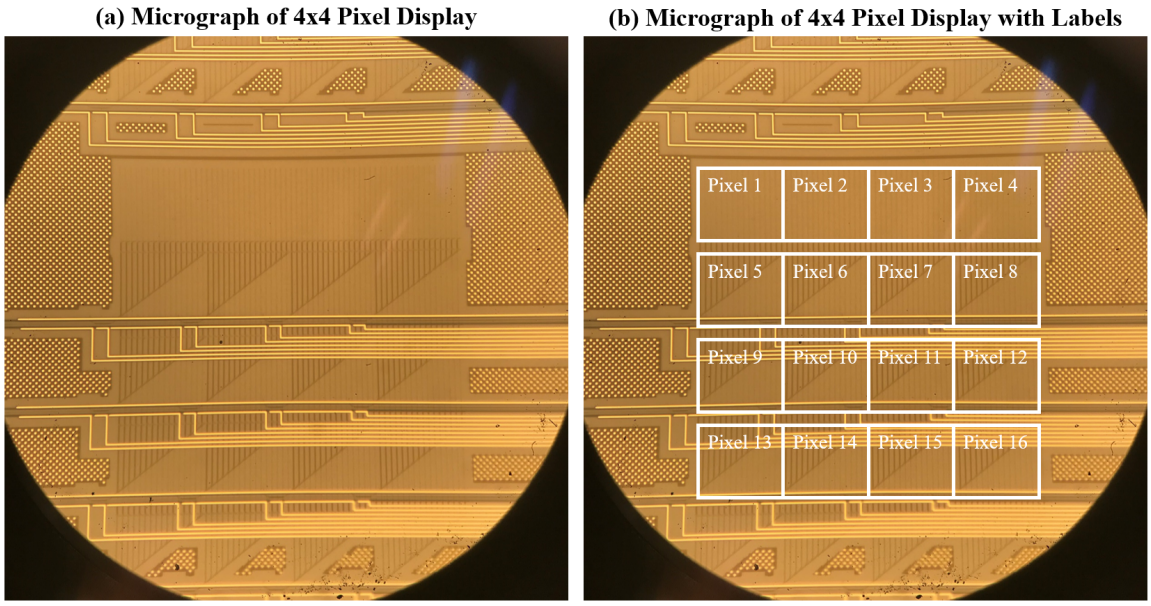

Figure 8.7: Micrograph of a fabricated 4x4 active VIPER display (a) without and (b) with pixels highlighted for clarity.

Electronic probes were then used to apply independently controllable voltages to each of the pixels in the display. The individual pixels in the display can be turned "on" or "off" independently. Fig. 8.9 shows images of the near field of the active display as we turn "on" and "off" select pixels in the top row of the display, demonstrating independent control of the pixels, (Fig. 8.9a highlights three pixels in the display for

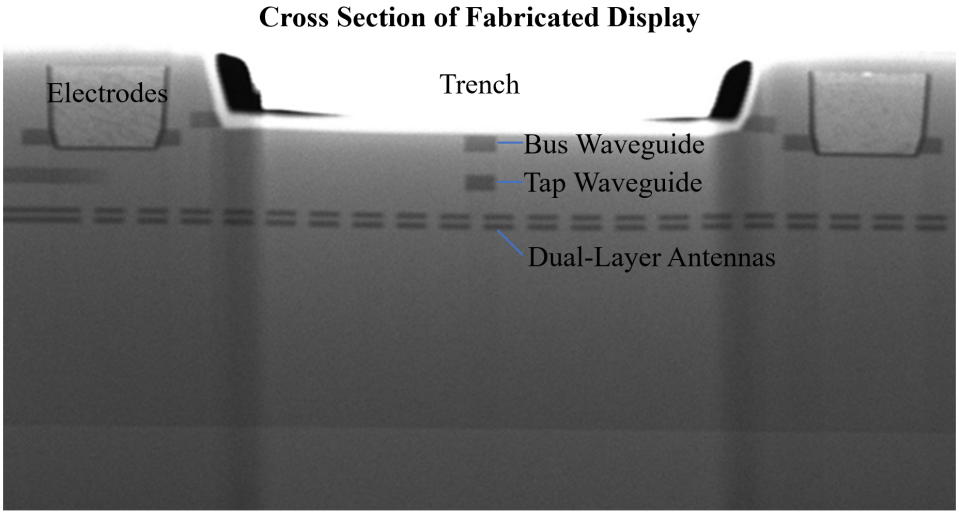

Figure 8.8: Transmission-electron-microscopy cross-sectional image of a section of the active display, with key components labeled (TEM image taken by SUNY Poly).

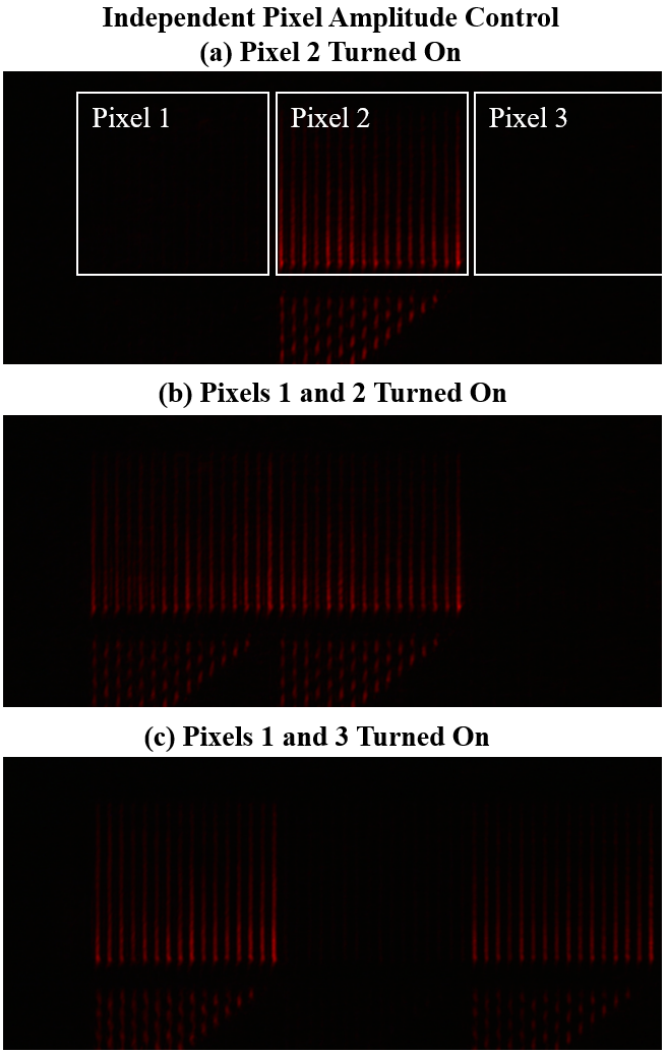

Figure 8.9: Experimentally measured near field of the first row in the active display as individual pixels are turned "on" and "off". (a) Pixel 2 turned "on", (b) pixels 1 and 2 turned "on", and (c) pixels 1 and 3 turned "on".

clarity).

Next, we use electronic probes to apply independent voltages to each of the pixels in the display to dynamically encode the display to spell out the letters in the word "LIGHT". An optical system was used to image the near field of the chip as the display switched between letters, as shown in Fig. 8.10.

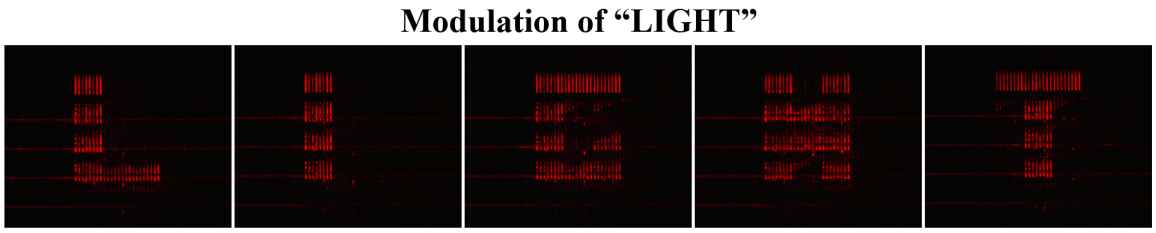

Figure 8.10: Experimental results showing five consecutive views of the near field of the active VIPER display as the display is encoded to spell out the letters in the word “LIGHT”.

8.3 Future Scaling

To support further scaling, the VIPER display was designed to be heterogeneously integrated with a custom thin-film-transistor electronics backplane in the future to enable integrated control of the display and scaling up to a large-scale video-hologram demonstration with increased number of pixels for greater resolution, as shown in Fig. 8.11a. Additionally, the VIPER display was designed to support scaling to multi-wavelength functionality for future RGB demonstrations, as shown in Fig. 8.11b.

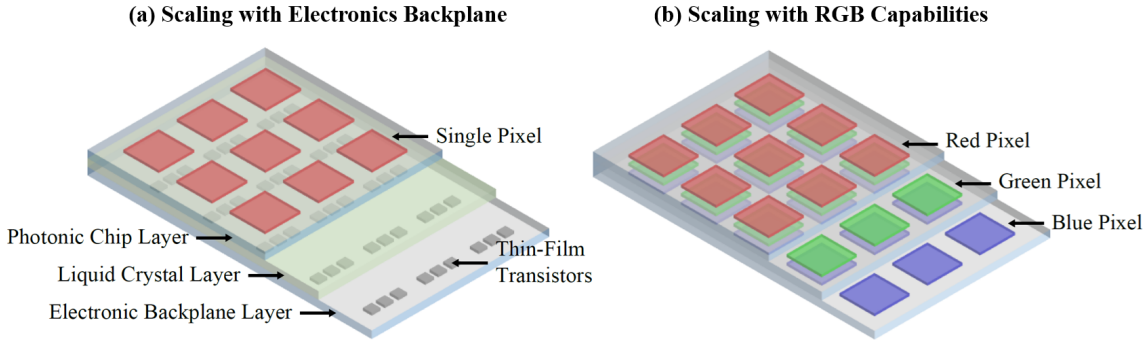

Figure 8.11: Simplified schematics showing the potential for scaling the VIPER display to (a) integrate with a thin-film-transistor electronics backplane and (b) operate as a multi-wavelength RGB display.

8.4 Conclusion

This initial prototype of an active VIPER display successfully confirms the active architecture with densely integrated and independently controllable pixels, the path towards further scaling to a large-scale active display with increased number of pix-

els and multi-wavelength functionality, and, in general, the overall VIPER display concept.

Chapter 9

Further Applications

In this chapter, applications beyond augmented reality are presented, including underwater optical communications, chip-based 3D printers, trapped-ion quantum systems, and integrated optical tweezers.

9.1 Underwater Wireless Optical Communications Using Integrated Optical Phased Arrays

The following work was done in collaboration with Daniel M. DeSantis (MIT), Michael Torres (MIT), and Jelena Notaros (MIT). This work has been published in [111].

9.1.1 Introduction to Underwater Wireless Optical Communications

Underwater wireless communications systems are a ubiquitous need in maritime applications such as submarine operations, underwater sensor networks, and unmanned underwater vehicle controls. However, conventional underwater communications are limited to acoustic and low-radio-frequency (RF) systems [5], which are severely hindered by low carrier-wave frequencies and, hence, cannot realize high-speed, low-latency data links. For this reason, extensive research has been thrust towards the implementation of optical systems for underwater wireless communications, which

enable orders of magnitude higher capacities than underwater acoustic and RF systems [6, 9]. However, current high-speed, dynamic, and unguided optical data links require the use of bulky mechanically aligned and steered lenses or mirrors [116], which are not well suited for harsh environments, such as those weathered by underwater wireless optical communications (UWOC) systems.

As an alternative to bulky optical systems, silicon-photonics-based integrated optical phased arrays (OPAs) have been demonstrated for free-space optical communications (FSOC) in air [42, 56, 57], where the OPA's electronically-tunable beam-steering capabilities mitigate the need for mechanically adjusted lenses. However, these demonstrations have been limited to infrared wavelengths, which are suitable for terrestrial FSOC, but not UWOC due to heavy absorption of infrared light through water. In contrast, for an OPA-based transmitter to be suitable for underwater applications, it must operate at a visible wavelength to fall within the transparency window of water, where absorption is a few orders of magnitude lower than at infrared wavelengths [9]. However, a visible-light integrated-OPA-based transmitter has yet to be shown.

Here, we show the first visible-light integrated-OPA-based FSOC transmitter and use it to demonstrate the first integrated-OPA-based UWOC link. We experimentally demonstrate a 1-Gbps on-off-keying (OOK) link through water and leverage the non-mechanical active beam-steering capabilities of this OPA architecture to establish an underwater point-to-multipoint link.

9.1.2 Underwater Wireless Optical Communications Experimental Setup and Results

The visible-light integrated OPA [109] was fabricated in a CMOS-compatible foundry process at the SUNY Polytechnic Institute and postprocessed at MIT. The OPA, described in detail in Ch. 7, consists of a silicon-nitride-based cascaded-phase-shifter architecture that linearly controls the relative phase applied to an array of antennas via electrically-tunable liquid-crystal (LC) birefringence [61]. An on-chip input edge cou-

pler couples light from an off-chip current-modulated 637-nm-wavelength diode laser into an on-chip silicon-nitride waveguide. A 100-μm-long adiabatic layer-transition structure then couples light into a bus waveguide. From the bus, evanescent tap couplers with a pitch of 20 μm and increasing coupling lengths uniformly distribute the light from the bus region to 16 grating-based 400-μm-long antennas with a 2-μm pitch. The OPA emits a beam with a $0.4° \times 1.6°$ power full width at half maximum, 8-dB sidelobe suppression, and second-order grating lobes at $\pm 18.8°$.

To enable a one-way simplex UWOC demonstration, digital data is superimposed onto an optical signal by modulation of the forward current through a laser diode, which results in an intensity-modulated optical signal that serves as an OOK digital signal. This modulated optical signal is coupled onto the photonic chip via an optical fiber, and the resulting beam formed by the OPA is emitted out of the surface of the chip. The beam propagates through free space, through a 75-cm-long glass tank filled with tap water, and again through free space, as depicted in Fig. 9.1. At the far end of the tank, avalanche photodetectors (APDs) are used to recover the information in the transmitted beam.

To characterize the link performance, we first use the integrated OPA passively (without beam steering) and recover the beam on the far side of the water-filled tank using a single 1-inch spherical lens and a high-speed APD. The recovered signal-to-

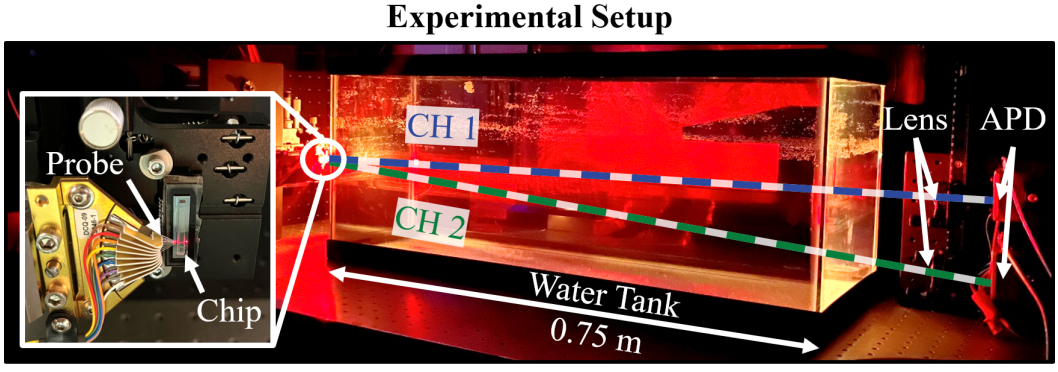

Figure 9.1: Photograph of the experimental setup for demonstrating an underwater optical communications link with a vertically mounted chip-based transmitter on the left side of a tank filled with tap water and a photodetector array on the right (inset showing photograph of photonic chip and probe).

noise ratio (SNR) is measured by sweeping the frequency of an RF signal generator that modulates the laser-diode current. At each frequency, both the RF power in the recovered signal and the noise floor of the detector are measured to calculate the SNR, depicted in Fig. 9.2a.

Next, we use a pattern generator to modulate the laser with an $N = 2^7 - 1$ pseudo-random binary sequence (PRBS) at 1 Gbps, where N is the number of bits in the PRBS. The OOK signal recovered from the APD was measured using an oscilloscope to generate an eye diagram, shown in Fig. 9.2b.

To demonstrate an actively tunable point-to-multipoint link, we apply a 10-kHz square-wave control voltage to the integrated electrodes on the photonic chip and – by varying the peak voltage – steer the beam emitted by the OPA [109] to an array of two separate APDs and matching lenses on the far side of the water-filled tank. These two APDs are vertically stacked, such that the first APD (CH1) is positioned boresight to the OPA (corresponding to a control voltage of 0 V) with the second APD (CH2) approximately 7 cm below the first (corresponding to a square wave peak voltage of approximately 2.5 V). The laser diode is modulated with a 100-MHz RF sinusoid and both APD voltages are captured with an oscilloscope, resulting in two spatially distinct wireless channels, as shown in Fig. 9.3a–b, with 19-dB and 22-dB channel-to-channel isolation for CH1 and CH2, respectively.

Finally, to demonstrate the utility of this modality, we replace the 100-MHz test

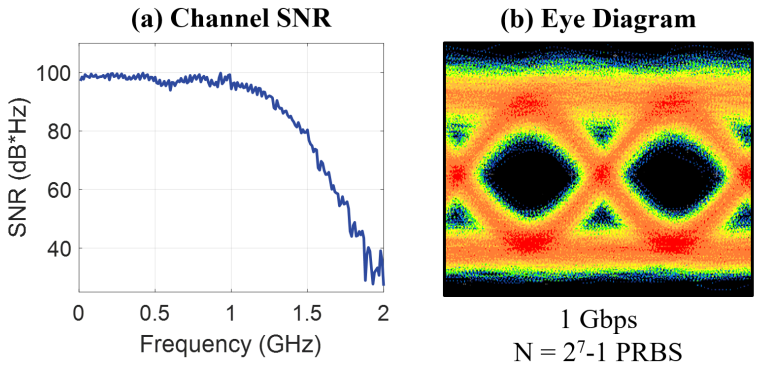

Figure 9.2: (a) Signal-to-noise ratio of the underwater wireless optical channel as a function of frequency. (b) Recovered digital eye diagram through the underwater wireless optical channel at 1 Gbps.

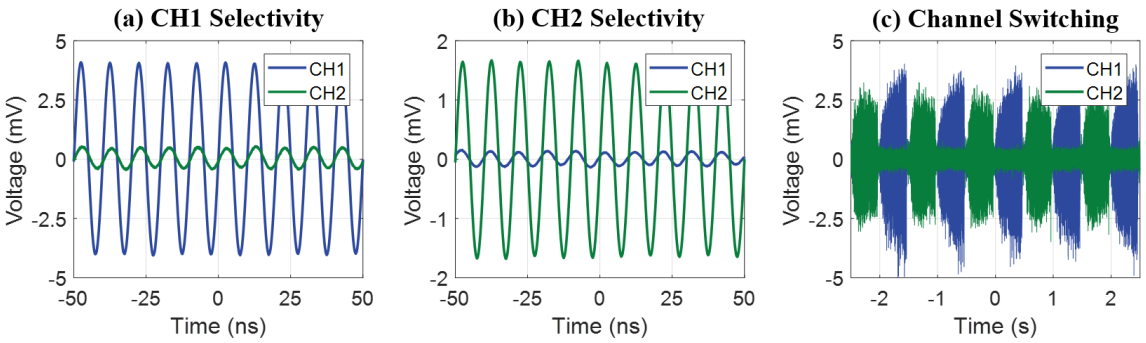

Figure 9.3: Signals recovered from CH1 and CH2 APDs showing spatial channel selectivity for (a) OPA steered to CH1 and (b) OPA steered to CH2. (c) PRBS recovered from CH1 and CH2 APDs showing electronically switchable time division multiplexing of the two spatially distinct wireless channels.

tone with a 100-Mbps PRBS and toggle the control voltage from 0 to a $2.5V_p$ square wave at 1 Hz to multiplex the transmitted data between the two detectors, shown in Fig. 9.3c. (Slight variations in detected voltage amplitude between experiments are due to APD repositioning and changes in LC driving voltage.) This adaptive modality represents time-division multiplexing of two beam paths (i.e. two channels) with one instantaneous active channel.

Here, we have presented the first visible-light integrated-OPA-based FSOC transmitter and used it to demonstrate the first integrated-OPA-based UWOC link. We experimentally demonstrated a 1-Gbps on-off-keying (OOK) link and an electronically-switchable point-to-multipoint link with channel selectivity of greater than 19 dB through a water-filled tank. This integrated OPA transmitter chip can reduce the size, weight, and mechanical complexity of apparatus for UWOC systems. Moving forward, we intend to scale this architecture for longer-range communications, extend its functionality to shorter green-blue wavelengths for further reduced water absorption, explore multi-beam emitters for underwater and free-space MIMO (multiple-input, multiple-output) optical communications, and implement an advanced architecture to emit circularly polarized light for robustness to turbulent water [117].

9.2 Silicon-Photonics-Enabled Chip-Based 3D Printer

The following work was led by Sabrina Corsetti (MIT) and done in collaboration with Tal Sneh (MIT), Alex Stafford (UT Austin), Zachariah A. Page (UT Austin), and Jelena Notaros (MIT). This work has been published in [118].

9.2.1 Introduction to 3D Printing

Imagine if it were possible to create 3D objects in the palm of your hand within seconds using only a single photonic chip. Although 3D printing has revolutionized the way we create in nearly every aspect of modern society [119–122], current 3D printers rely on large and complex mechanical systems to enable layer-by-layer addition of material. This limits print speed, resolution, portability, form factor, and material complexity. Although there have been recent efforts in developing novel photocuring-based 3D printers that utilize light to transform matter from liquid resins to solid objects using advanced methods [123, 124], they remain reliant on bulky and complex mechanical systems.

To address these limitations, we combine the fields of silicon photonics and photochemistry to propose the first chip-based 3D printer. The proposed system consists of only a single millimeter-scale photonic chip without any moving parts that emits reconfigurable visible-light holograms up into a simple stationary resin well to enable non-mechanical volumetric 3D printing, as depicted in Fig. 9.4a. This system enables a highly-compact, portable, and low-cost solution for the next generation of 3D printers.

Here, we develop a proof-of-concept system that serves as a fundamental stepping stone on the path towards this volumetric chip-based 3D-printer vision. Specifically, we experimentally demonstrate a stereolithography-inspired version of the chip-based 3D printer (depicted in Fig. 9.4b) capable of 3D printing arbitrary patterns in two dimensions using a beam-steering integrated visible-light liquid-crystal-based optical phased array (discussed in Ch. 7) and visible-light-curable resins. The resin used in the stereolithography-inspired proof-of-concept demonstration of the chip-based 3D

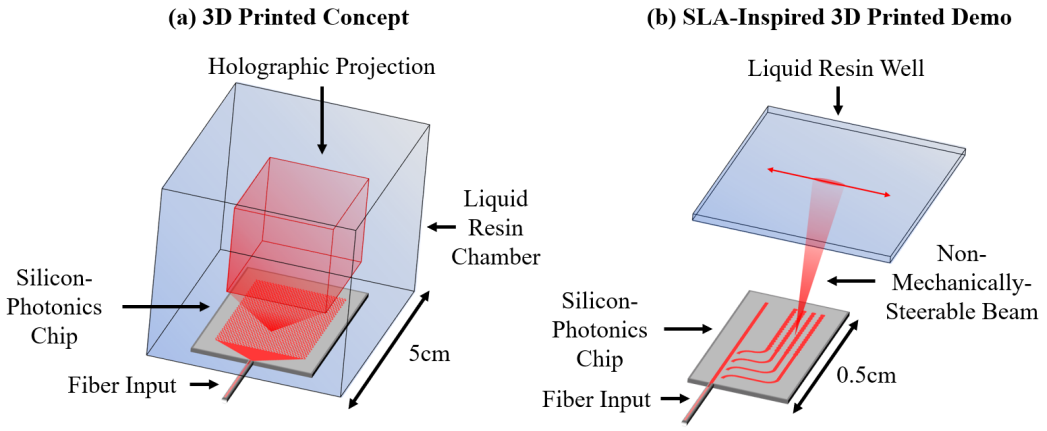

Figure 9.4: (a) Conceptual diagram of the proposed chip-based 3D printer, showing a hologram formed by a chip within a resin chamber (not to scale). (b) Conceptual diagram of the proof-of-concept stereolithography-inspired chip-based 3D printer demonstrated in this work (not to scale).

printer is a three-component-photosystem-based resin designed for efficient photocuring at visible wavelengths, as developed in [125, 126].

9.2.2 Chip-Based 3D Printer Experimental Setup and Results

Using the visible-light integrated optical phased array (discussed in Ch. 7) and the visible-light-curable resin developed in [125, 126], we demonstrate 3D printing using a chip-based system for the first time.

The setup used for this printing demonstration is shown in Fig. 9.5a. The fabricated and packaged 3D-printer photonic chip is mounted on a chuck, with a sample stage that supports liquid resin wells mounted on a positioning system above the chip. Light is routed from an off-chip diode laser centered at 637 nm via a P1-630Y cleaved fiber and is edge coupled to the on-chip system.

To create a well for the liquid resin, two coverslips are separated by one layer of double-sided tape on the left-hand side of the well and one layer of single-sided tape on the right-hand side of the well to ensure that the coverslips are securely attached, while also creating an easy-access hinge for removing cured prints from the well. This creates a chamber with a thickness of approximately 60 μm into which 55 μL of liquid resin is pipetted. The well containing the resin is then clamped into the

sample stage above the chip and centered on the main lobe emitted by the integrated optical phased array, as shown in Fig. 9.5a. Resin preparation and 3D printing are performed in a dark environment to prevent curing from visible-light sources other than the integrated optical phased array.

After centering the resin sample on the main lobe of the integrated optical phased array, we use the visible-light microscope path to monitor curing, which is observable via diffraction of the integrated optical phased array's radiation pattern around a solidified voxel. As depicted in Fig. 9.5b, a 3D-printed voxel presents as a bleached region (white/transparent) within remaining leftover resin (blue) due to photobleaching of the blue aza-Br photoredox compound during the photocuring reaction. Using a Kim wipe and isopropyl alcohol, we separate the cured print from the remaining uncured liquid resin. The result is a free-standing 3D-printed voxel in the shape of the integrated optical phased array's main lobe (Fig. 9.5b). The single voxel depicted in Fig. 9.5b measures approximately 0.5 mm $\times$ 0.125 mm in the plane of the photograph with a height of approximately 60 µm. The voxel height is determined by the spacing of the resin well's coverslips (60 µm for this test). The planar dimensions of the voxel are determined by the distance between the integrated optical phased array and the resin well, since the integrated optical phased array used for this proof-of-concept 3D printer emits a diffracting beam ($0.4° \times 1.6°$). In this demonstration, we

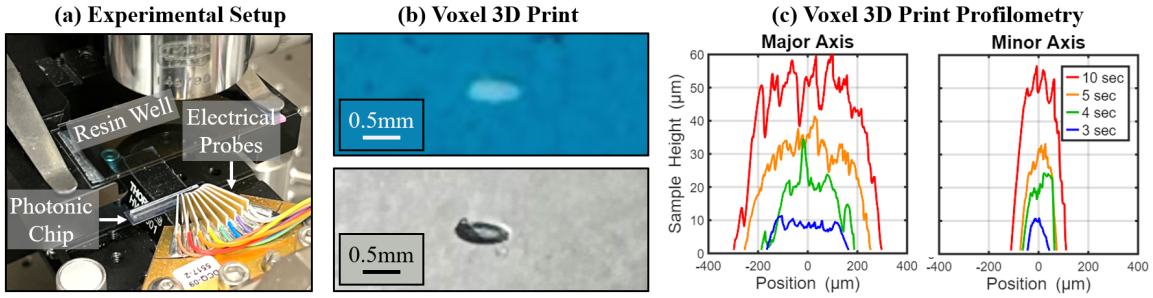

Figure 9.5: (a) Photograph of the setup used for the proof-of-concept 3D-printer demonstration, depicting the input fiber, photonic chip, and resin well. (b) Photographs of a 3D-printed voxel, created using the chip-based printer, within a well of remaining liquid resin (top) and the same solid 3D-printed voxel after separation from the remaining liquid resin (bottom). (c) Measured dimensions for four separate voxels 3D printed with varying printing times of 3, 4, 5, and 10 seconds, demonstrating the formation of voxels as a function of time.

placed the resin well 2.5 cm over the surface of the 3D-printer chip, resulting in sub-millimeter-scale voxels (Fig. 9.5b–c). The use of focusing integrated optical phased arrays developed by our group [47] in future iterations of the chip-based 3D printer would enable printing of even smaller micron-scale voxels.

To characterize the curing rate and print formation process of these voxel prints, we performed curing and profilometry for 3D prints with varying curing time intervals (Fig. 9.5c). Specifically, we 3D printed four single voxels using four separate resin wells with varying printing times of 3, 4, 5, and 10 seconds. After separating the resulting voxels from the remaining liquid resin, we used a Veeco Dektak 150 Surface Profilometer to measure the height of the prints along their major and minor (longer and shorter) axes. As depicted in Fig. 9.5c, we find that 3D-printed voxels grow as a function of time, eventually reaching a plateau upon growing to the top of the resin well, at a height of approximately 60 μm. To demonstrate the rapid curing capability of the system for this test, we set the power of the off-chip diode laser such that approximately 6.7 μW of optical power was supplied to the main lobe of the integrated optical phased array. At this power, we observe voxel printing within seconds (Fig. 9.5c). Even at significantly lower optical powers on the order of 100 pW, we can still observe voxel formation within 10 minutes, with a nonlinear relationship between optical power and printing time [125, 126].

Utilizing the non-mechanical beam-steering capabilities of the visible-light integrated optical phased array (discussed in Ch. 7), we then moved beyond the printing of single voxels and demonstrated 3D printing of one- and two-dimensional patterns.

To enable non-mechanical beam steering in the array dimension of the integrated optical phased array, we use electronic probes to contact the photonic chip's integrated electrodes and apply a 10-kHz square wave across the electrodes of the liquid-crystal phase shifter. We vary the peak voltage of this applied square wave to tune the phase gradient applied across the antennas and, hence, steer the formed beam in the array dimension by up to 7.2° within ±3.4 V. as shown in Fig. 7.6b. Further details regarding integrated-optical-phased-array beam-steering characterization are provided in Ch. 7.

Using this non-mechanical beam-steering capability, we demonstrate 3D printing of a line into the resin, as shown in Fig. 9.6a. We print this line by sweeping the voltage applied to the liquid-crystal phase shifter from 0 V_p to 3 V_p. As the voltage applied to the phase shifter is increased, the refractive index of the liquid crystal relative to the mode in the phase shifter increases, leading to lower confinement of the mode in the bus waveguide. As a result, the power delivered to the integrated optical phased array antennas decreases as the radiation pattern steers. To compensate for this, we print for longer times at higher voltages than for lower voltages, to ensure uniform curing along the line. As depicted in Fig. 9.6a, the 3D-printed line is distinguishable from the remaining blue liquid resin, as in the case of the single-voxel print in Fig. 9.5b. We again separate the print from the remaining liquid using a Kim wipe and isopropyl alcohol, and we demonstrate that the result is once again a free-standing 3D-printed solid.

Using single-line prints as a building block, we now demonstrate the system's ability to 3D print arbitrary patterns in two dimensions, thus realizing our proof-of-concept stereolithography-inspired chip-based 3D printer system. To transition from single-line prints to arbitrary two-dimensional patterns, we use the resin well's mechanical positioning stage. Specifically, after printing each one-dimensional line in a desired pattern, we use the mechanical stage to move the well with micron-

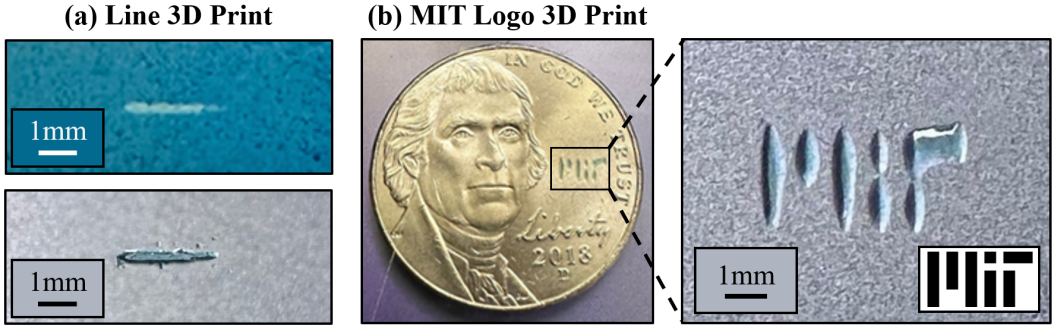

Figure 9.6: (a) Photographs of a 3D-printed line, created using the chip-based printer, within a well of remaining liquid resin (top) and the same solid 3D-printed line after separation from the remaining liquid resin (bottom). (b) Photographs of a 3D-printed MIT logo, created using the chip-based printer, with a U.S. nickel for scale (left) and zoomed in (right).

scale precision in the second dimension. As a specific demonstration, we perform a print of the Massachusetts Institute of Technology (MIT) logo, creating each line in the print from a subset of the single-line voltage range (0-3 V_p). To promote rapid yet controlled printing for this demonstration, we set the power of the off-chip diode laser such that approximately 1.9 μW of optical power was supplied to the main lobe of the integrated optical phased array. Between each line of the print, we decrease the integrated optical phased array's output power to prevent curing between components. As oxygen in the sample is quenched during the print, the curing rate becomes faster [126]. We thus adapt the amount of time spent on each component of the logo to ensure uniform curing (e.g., printing the vertical component of the "T" in the logo faster than the bottom component of the "I"). The final print, performed in under 6 minutes total, is depicted in Fig. 9.6b, once again separated from any remaining liquid resin using a Kim wipe and isopropyl alcohol.

This work combines the fields of silicon photonics and photochemistry to propose the first chip-based 3D-printing technology. The proposed system consists of only a single millimeter-scale photonic chip without any moving parts that emits reconfigurable visible-light holograms up into a simple stationary resin well to enable non-mechanical volumetric 3D printing.

The chip-based 3D-printing technology introduced in this work has the potential to enable a highly-compact, portable, and low-cost solution for the next generation of 3D printers. Such a solution would offer a more accessible and rapid mechanism for generating 3D objects, impacting a wide range of application areas, including military, medical, engineering, and consumer.

9.3 Integrated-Photonics-Based Devices and Architectures for Advanced Cooling of Trapped Ions

The following work was led by Ashton Hattori (MIT), Sabrina Corsetti (MIT), and Tal Sneh (MIT) and done in collaboration with Reuel Swint (MIT Lincoln Laboratory),

Patrick T. Callahan (MIT Lincoln Laboratory), Colin D. Bruzewicz (MIT Lincoln Laboratory), Felix Knollmann (MIT), Robert McConnell (MIT Lincoln Laboratory), John Chiaverini (MIT Lincoln Laboratory), and Jelena Notaros (MIT). This work has been published in [11, 127].

9.3.1 Introduction to Trapped-Ion Quantum Systems

Systems of trapped ions are a promising modality for quantum information processing due to their long coherence times and strong ion-ion interactions, which enable high-fidelity two-qubit gates [128]. Most current implementations are comprised of complex free-space optical systems, whose large size and susceptibility to vibrations and drift can limit fidelity and addressability of ion arrays, hindering scaling to large numbers of qubits. Recent works based on integrated photonic devices offer a potential avenue to address many of these challenges [10–12, 14].

Motional state cooling is a key optical function in trapped-ion systems. To date, integrated-photonics-based cooling demonstrations have been limited to Doppler and resolved-sideband cooling [10, 14]. However, polarization-gradient (PG) and electromagnetically-induced-transparency (EIT) cooling can offer better cooling performance in multi-ion systems, where sub-Doppler temperatures in several non-degenerate modes are desirable. While free-space demonstrations of these cooling schemes have been shown [129, 130], each having an advantage for differing applications, integrated versions of these systems have not yet been realized.

In this work, we propose integrated-photonics-based system architectures and the design of key integrated photonic components for both PG and EIT cooling of trapped ions (conceptual diagram shown in Fig. 9.7a). Specifically, we design the systems for a wavelength of 422 nm to target the $S_{1/2}$ to $P_{1/2}$ transition of $^{88}Sr^{+}$, a commonly used ion species for trapped-ion qubits.

9.3.2 Integrated-Photonics-Based Architectures for Trapped-Ion Cooling

We leverage a 200-mm wafer-scale visible-wavelength process developed at MIT Lincoln Laboratory to enable low-loss waveguide fabrication over a wavelength range relevant to commonly used ion species [65]. The platform consists of two bottom layers of 100-nm-thick silicon nitride (Si_3N_4) and an upper layer of 100-nm-thick alumina (Al_2O_3) separated by 90 nm of silicon dioxide (SiO_2). A top metal layer is etched to create linear-ion-trap electrodes that confine ions 50 μm above the trap surface via radiofrequency and DC voltages [128].

Trapped ions located in a suitable laser-polarization gradient can achieve sub-

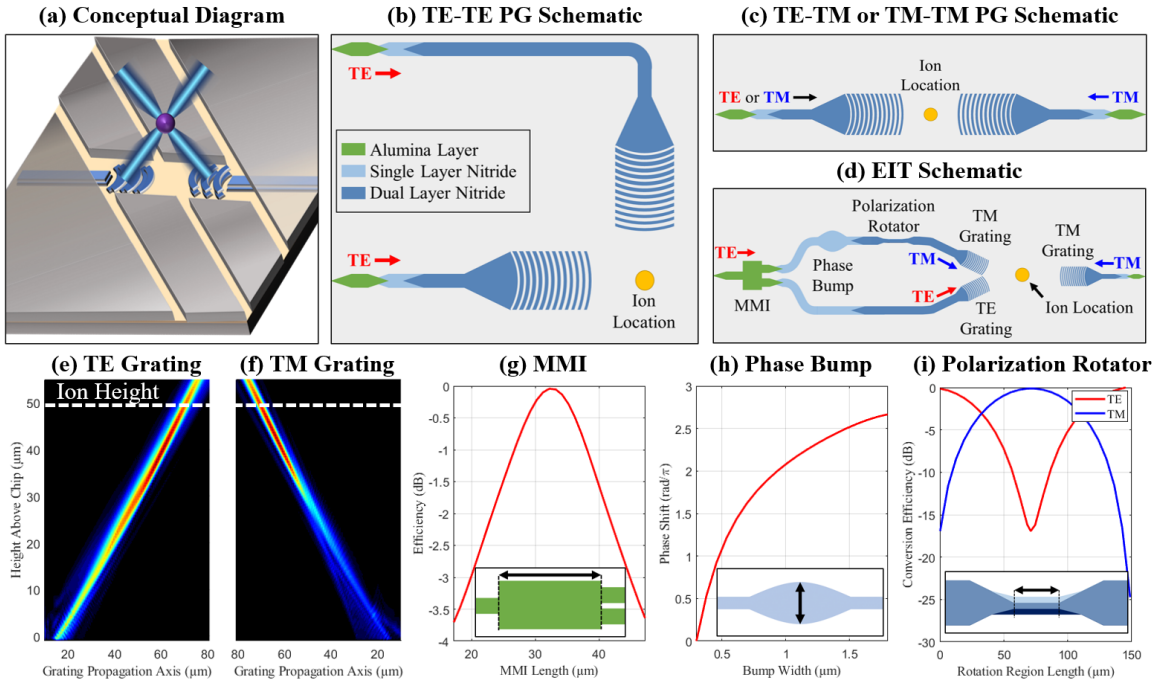

Figure 9.7: (a) Conceptual diagram of the integrated PG-cooling system. Simplified schematics showing the proposed integrated-photonics-based architectures for (b) TE-TE PG cooling, (c) TE-TM or TM-TM PG cooling, and (d) EIT cooling (not to scale). Simulated emission profiles for the (e) TE grating and (f) TM grating, showing focusing near the height of the ion. (g) Simulated MMI efficiency as a function of MMI length (inset shows device schematic). (h) Simulated phase delay as a function of phase bump width (inset shows device schematic). (i) Simulated conversion efficiency of the off-axis polarization rotator with TE in blue and TM in red (inset shows device schematic).

Doppler temperatures due to the preferential scattering of cooling photons in a spatially-varying, state-dependent energy potential [129]. Appropriate polarization gradients can be realized on-chip using different configurations of integrated grating couplers; for example, two transverse-electric (TE) gratings placed orthogonal to each other (TE-TE), a TE and transverse-magnetic (TM) grating placed opposite to each other (TE-TM), or two TM gratings placed opposite to each other (TM-TM) all suffice. The simulated emission profiles for gratings specifically designed for TE and TM are shown in Fig. 9.7e–f. Both gratings are designed to match intensity and focus near the ion at an angle of 45°, maximizing intensity at the ion location. In all three polarization configurations, light is routed to these gratings via two separate inverse-taper edge couplers and a combination of 650-nm-wide alumina waveguides, 300-nm-wide dual-layer silicon-nitride waveguides, and vertical transitions between layers. The final proposed architectures for PG cooling are shown in Fig. 9.7b–c.

EIT cooling enables near ground-state cooling over a wide frequency range by suppressing unwanted heating mechanisms otherwise incurred during laser cooling. Previous free-space demonstrations have relied on two appropriately-polarized laser sources (one circular and one linear) to create the desired laser absorption profile [130]. Fig. 9.7d depicts integrated realization of both the circular and linear sources. To generate the circularly polarized source, light is coupled on chip via an inverse-taper edge coupler to an alumina waveguide. Next, the light is split evenly into two arms using a 32.2-μm-long 1x2 alumina multi-mode interferometer (MMI); simulated efficiency as a function of device length for the MMI is shown in Fig. 9.7g. In the upper arm, the light is transitioned to single-layer silicon nitride. Then, the waveguide is adiabatically widened for a given length, forming a phase bump to impart a 90° phase shift; simulated phase as a function of bump width is shown in Fig. 9.7h. After passing through the phase bump, the light is transitioned to dual-layer nitride. There, it goes through an off-axis polarization rotator, which rotates the incoming light from TE to TM (described in Sec. 9.3.3); the conversion efficiency as a function of device length can be seen in Fig. 9.7i, with a peak simulated conversion efficiency of 99.15% [127]. Finally, the TM light in the upper arm is emitted via a TM grating.

In the lower arm from the MMI, the TE light is transitioned to dual-layer nitride and is emitted via a TE grating. The two gratings in each arm are angled so that the beams combine and form approximately circularly polarized light at the ion location. The linear TM input is coupled on-chip from an inverse-taper edge coupler into an alumina waveguide. Next, it is transitioned to dual-layer silicon nitride, where it emits from a focusing TM grating placed opposite to the circularly polarized source, thus enabling EIT cooling.

In this work, we have developed a framework for two advanced trapped-ion cooling schemes, PG and EIT, using a visible-wavelength silicon-photonics platform at 422 nm. We have also developed designs of key integrated-photonics components required to realize these architectures. This approach provides a scalable platform that promises more rapid cooling of multiple vibrational modes when compared to previously shown integrated approaches. Additionally, these approaches should be applicable to neutral-atom laser cooling when tailored to other wavelengths.

9.3.3 Integrated Visible-Light Polarization Rotators and Splitters for Trapped-Ion Systems

Polarization control plays an important role in photonic integrated circuits (PICs), where it can enhance polarization-sensitive device performance as well as enable systems that can benefit from orthogonal modes, such as increased channel density for communications [131,132]. As such, there has been extensive research into integrated polarization rotators and splitters [132–136]; so far, however, they have only been shown at infrared (IR) wavelengths.

Recently, there has been a significant drive to develop PICs at visible wavelengths that require polarization manipulation, in particular for chip-scale atomic systems and qubit state preparation [10, 136] (discussed in Sec. 9.3.2). However, integrated polarization-control devices for these systems have yet to be developed, a particular challenge given the scaling of device dimensions with wavelength.

In this work, we demonstrate the design of the first integrated polarization rotators

and splitters operating at blue wavelengths. Specifically, using combinations of single and dual silicon-nitride (SiN) waveguide sections, we show an adiabatic polarization rotator, a compact off-axis polarization rotator, and a mode-coupling polarization splitter all operating at a wavelength of 422 nm.

Similar to the above section, the devices in this work were designed for fabrication compatibility with the MIT Lincoln Laboratory 200-mm wafer fabrication platform for ultraviolet to near-IR wavelengths [65], which consists of a 100-nm-thick alumina (Al_2O_3) layer and two 100-nm-thick silicon-nitride (Si_3N_4) layers separated by 90 nm of silicon dioxide (SiO_2).

First, we design an adiabatic polarization rotator which converts between the fundamental TE and TM modes on chip (Fig. 9.8a). This device begins with an asymmetric coupler that converts the input fundamental TE mode to the next higher

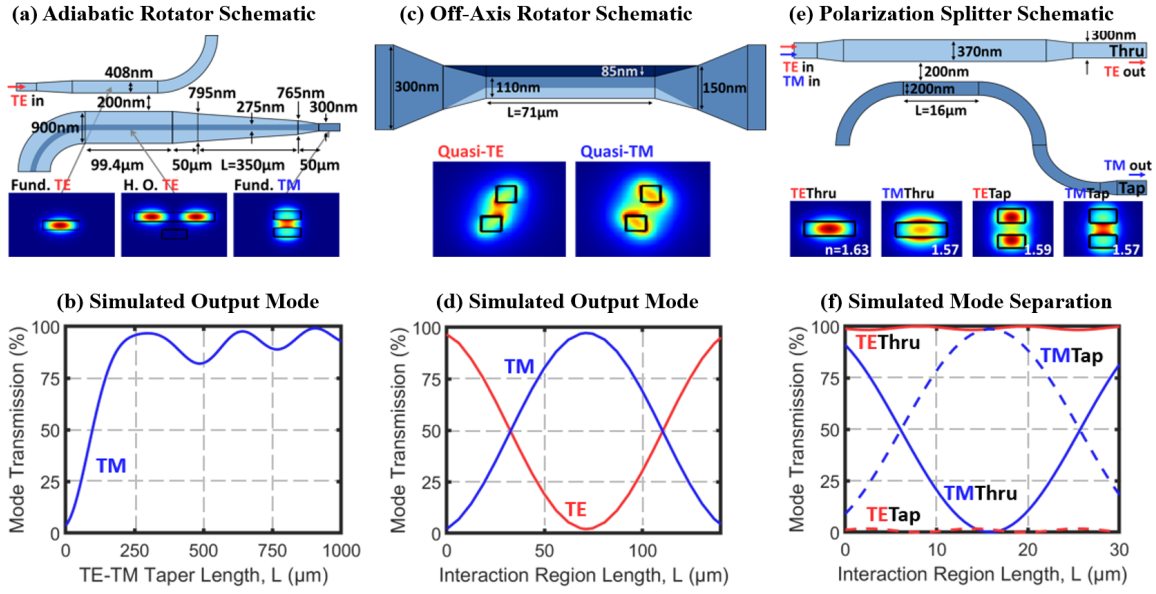

Figure 9.8: (a) Schematic (not to scale) of the adiabatic rotator, with relevant mode profiles shown. (b) Mode conversion efficiency of the adiabatic rotator as a function of TE-TM taper length. (c) Schematic of the off-axis rotator, with mode profiles that demonstrate the 45° optical axis rotation of the fundamental modes in the interaction region. (d) Mode conversion efficiency of the off-axis rotator as a function of interaction length. (e) Schematic of the polarization splitter, with mode profiles demonstrating the effective index match and contrast between the fundamental TM and TE modes, respectively. (f) Mode splitting efficiencies for the thru and tap ports for the polarization splitter as a function of interaction length.

order TE mode. The mode then enters an adiabatic taper, which passes through an anti-crossing between the higher order TE and fundamental TM modes, transferring power from one mode to the other. This anti-crossing is enabled by breaking the vertical symmetry via the dual SiN layer (Fig. 9.8a) [133]. By utilizing a three-stage taper that varies more rapidly on either side of the anti-crossing, the total device length is reduced without a significant sacrifice in performance. The total device length is 550 μm, giving a simulated device efficiency of 93.78%, corresponding to an extinction ratio of 11.78 dB (Fig. 9.8b).

As a complement to the above device, it is useful to have a more compact polarization rotator that can be used in more densely integrated systems. To this end, we also design an off-axis rotator that works on the principle of mode coupling between the two lowest-order modes (Fig. 9.8c), which have a high coupling coefficient [134]. By horizontally offsetting two stacked waveguides appropriately in the coupling region, both the fundamental modes become quasi-TE and TM, corresponding to an effective optical axis oriented at 45°. As a result, the fundamental modes exhibit beating and, by appropriate choice of length, the input TE mode can be efficiently converted to TM [134]. Gradual tapers into and out of the coupling region minimize radiative losses due to mode mismatch. The total device length is only 111 μm, achieving a simulated efficiency of 99.15%, corresponding to an extinction ratio of 20.7 dB (Fig. 9.8d).

Third, we design an integrated asymmetric directional-coupler-based polarization splitter, using the dual SiN layers to maximize TM coupling into the tap port, while minimizing coupling of the TE mode (Fig. 9.8e). The device consists of a single-layer thru port and a dual-layer tap port, where the effective indices of the TM modes are matched between the two arms of the coupler. Due to their asymmetry, the two arms exhibit very different effective indices for TE [135] (Fig. 9.8e). As a result, the fundamental TM mode periodically strongly couples between the arms of the device along the length of the coupling region, while the TE mode exhibits only low-amplitude oscillations (Fig. 9.8f). The length of the coupling region of this device is only 16 μm, providing a compact device that allows for extinction ratios of 46.3 dB

for TM input and 18.7 dB for TE input for their respective ports.

In this work, we design the first integrated polarization rotators and splitter operating at blue wavelengths, enabling integrated polarization-diversity schemes, increased datacom channel density, and advanced chip-scale atomic systems.

9.4 Optical Tweezing Using Integrated Optical Phased Arrays

The following work was led by Tal Sneh (MIT) and done in collaboration with Sabrina Corsetti (MIT), Kru Kikkeri (MIT), Joel Voldman (MIT), and Jelena Notaros (MIT). This work has been published in [137, 138].

9.4.1 Introduction to Optical Trapping and Tweezing

Optical trapping and tweezing has garnered significant interest as a preferred technology for the non-contact manipulation of cells and microscale particles, producing impactful research for applications including cell classification, force sensing, and characterization [139, 140]. However, the cost, size, and complexity of these tools when using standard bulk-optical components has limited their utility. As an alternative, the development of on-chip optical traps has been pursued, using evanescent fields from waveguides, resonators, and plasmonic devices [141–143]. While these systems have offered significant advantages in cost, form factor, and complexity, they have been restricted to trapping within microns of the chip surface, which limits their widespread adoption in practical biophysics experiments and for in-vivo applications that require millimeter-scale standoffs. In addition, many of these prior integrated optical tweezers have been fundamentally limited to passive trapping demonstrations that lack active spatial tuning of the optical fields, necessary for object tweezing and manipulation.

In contrast, integrated optical phased arrays (OPAs), which enable emission and non-mechanical control of arbitrary free-space radiation patterns from compact pho-

tonics chips, have the potential to resolve these limitations. Specifically, they provide a promising approach to extending the standoff operating distance, enabling spatial tuning for tweezing, and expanding to holographic multi-beam capability for sorting in the future. However, motivated by applications such as LiDAR sensing, the majority of integrated OPA demonstrations to date have been limited to generating and steering beams in the far field [48], which do not generate the tightly-focused beam profiles required for optical trapping. Recently, our group demonstrated the first integrated OPAs that enable these focusing beam profiles [47].

In this work, we demonstrate integrated OPA-based optical trapping and tweezing for the first time. The OPA system focuses the emitted light and provides a steerable potential-energy well that can be used to trap and tweeze microscale particles (Fig. 9.9a–b). Using this approach, we increase the standoff distance of integrated optical tweezers by over two orders of magnitude compared to prior demonstrations and show trapping and non-mechanical tweezing of polystyrene microspheres 5 mm above the surface of a silicon-photonic chip. We then use the tweezers to stretch mouse lymphoblast cells, showing, to the best of our knowledge, the first cell experiments using single-beam integrated optical tweezers.

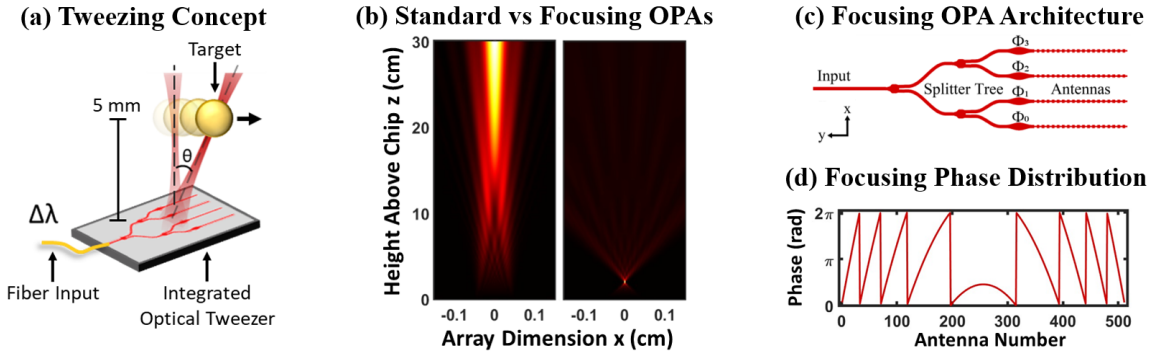

Figure 9.9: (a) Conceptual diagram depicting microsphere tweezing using an OPA by varying the input laser wavelength. (b) Simulated array-factor intensity above the chip for a standard non-focusing OPA (left) and near-field-focusing OPA with a 20-mm focal height (right). (c) Schematic of a passive splitter-tree-based focusing OPA architecture with 4 antennas (not to scale). (d) Element phase distribution for a focusing OPA with a 20-mm focal height, 512 antennas, 2-μm antenna pitch, and 1550-nm wavelength.

9.4.2 Chip-Based Optical Tweezing of Microspheres and Cells

The near-field-focusing integrated OPA [47] was fabricated in a CMOS-compatible foundry process at the SUNY Polytechnic Institute. At the input, an inverse-taper edge coupler couples light from a 1550-nm-wavelength off-chip tunable laser source into an on-chip silicon waveguide. A 9-stage splitter tree network then distributes the input power to 512 waveguide arms with a final pitch of 2 μm. Each arm is terminated with a 0.9-mm-long grating-based antenna that radiates the light upwards out of the chip. Before each antenna, a phase bump structure is placed to encode a static hyperbolic phase distribution (Fig. 9.9d) that enables focusing of the off-chip emission in the array dimension (x). Additionally, the antenna period is adiabatically chirped to enable focusing in the antenna dimension (y). The OPA architecture is shown in Fig. 9.9c. Additional details on the focusing integrated OPA are provided in [47].

To characterize our integrated OPA-based optical trap, the trap chip is mounted beneath a sample stage, and light is coupled onto the chip from a tunable benchtop laser.

To demonstrate optical trapping, we use samples consisting of two coverslips separated by a thickness of 375 μm, into which a 5.5% v/v solution of 10-μm-diameter polystyrene microspheres suspended in deionized water is pipetted. The sample is clamped into the stage, and a target sphere is moved into the focal spot of the trap, where its motion is recorded for 75 seconds. To verify that the motion of the sphere is reduced specifically due to the trap, the laser is turned off, and the sphere's motion is recorded for an additional 75 seconds. Using the TrackMate plugin for ImageJ [144], we track the motion of a group of microspheres, of which the middle sphere is trapped, as shown in Fig. 9.10a.

To quantify the trap's stiffness, we use the equipartition theorem and the mean squared displacement of spheres in the trap, measured using TrackMate [144, 145]. We perform four repeated measurements over a range of input powers. As shown in Fig. 9.10b, the results follow the expected linear trend, with error bars calculated as

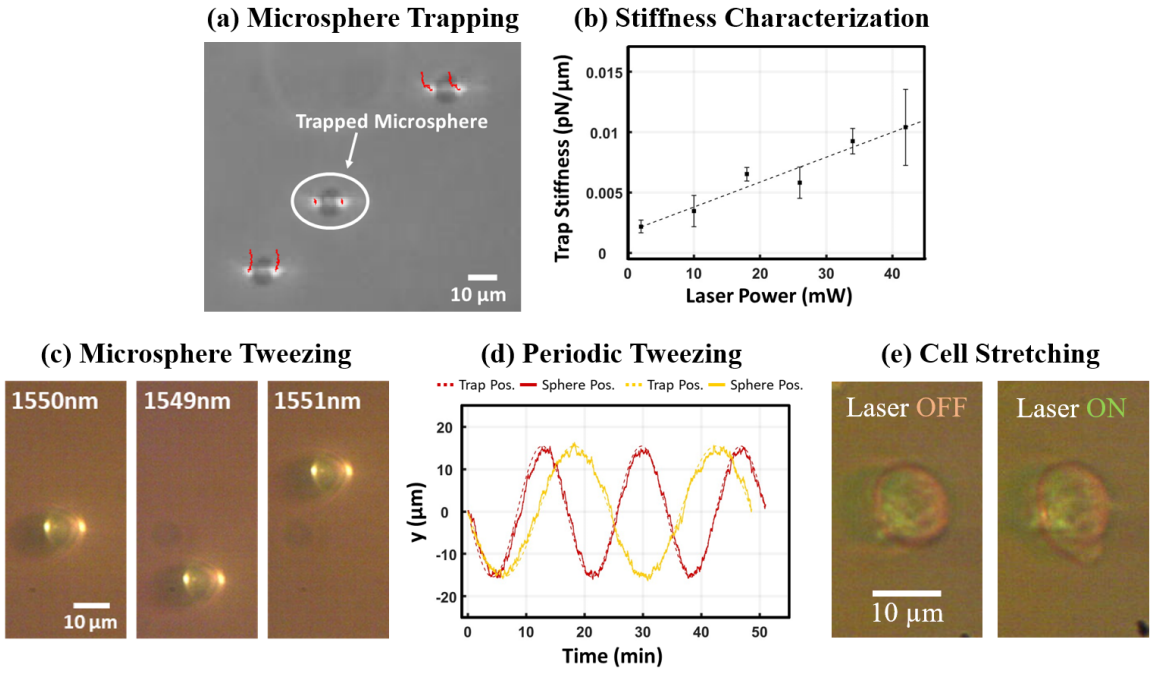

Figure 9.10: (a) Micrograph of microspheres in a sample well with superimposed tracks showing their motion over time (red lines); the motion of the microsphere located at the focal spot of the OPA (circled in white) is significantly reduced compared to its neighbors, indicating successful trapping. (b) Measured trap stiffness versus optical power for polystyrene microsphere trapping; error bars are found by calculating the standard error of the dataset. (c) Micrographs showing the position of a microsphere for input wavelengths of 1550 nm (left), 1549 nm (center), and 1551 nm (right); the position varies with input wavelength, confirming successful tweezing. (d) Position of the spot formed by the optical trap (dashed line) and position of the optically tweezed microsphere (solid line) versus time for two different sinusoidal wavelength control signals, demonstrating consistent tweezing over arbitrary 1D patterns. (e) Micrograph showing a TIB-49 mouse lymphoblast cell trapped in the focus of the optical trap (left); the wavelength of the input laser is reduced by 0.6 nm, steering the trap focus in the -y direction below the cell, resulting in the cell being stretched downward by the movement of the trap (right).

the standard error of the measurements.

To transform the system from a static trap to dynamic tweezers, we leverage the non-mechanical spot steering capability of our OPA system. Specifically, we vary the wavelength of the laser input into the OPA system to steer the location of the spot emitted by the OPA, resulting in the microsphere successfully following its motion. To demonstrate that the microsphere can be steered in arbitrary patterns in one dimension, we show repeated tweezing of the microsphere in a sine-wave pattern with

two different frequencies (Fig. 9.10c–d).

Finally, we use the OPA system to perform, for the first time, cell experiments with single-beam integrated optical tweezers, showing controlled deformation of cells. We culture TIB-49 mouse lymphoblast cells in RPMI-1640 media with 10% Fetal Bovine Serum and 1% 10,000 U/mL Penicillin-Streptomycin. We incubate the cells at 37°C in a humidified 5% CO2 incubator and pipette them into a sample well. We position a cell in the optical trap and steer the trap in the y direction in the focal plane. We record the cell and observe that its bottom edge is attracted to the new trap position (Fig. 9.10e), leading to an increase in the cell aspect ratio of over 25% along its long axis. Upon turning off the laser, the cell relaxes to its prior unstretched state.

This work introduces a new modality for integrated optical tweezers, presenting a fundamentally different approach based on integrated OPAs that enables significantly larger standoff distances and arbitrary active tweezing functionality. This OPA-based approach offers the advantages in cost, footprint, complexity, and mass-producibility of integrated tweezers, while providing much of the functionality of bulk-optical systems. It thus represents a significant improvement in the utility and compatibility of integrated optical tweezers for biological research and opens the door to a variety of experiments that have not been previously possible with prior implementations of integrated tweezers, spanning biophysics research with microsphere-conjugated molecules, cell experimentation and sorting, and emerging in-vivo trapping research.

9.5 Conclusion

In this chapter, applications beyond augmented reality were presented, including underwater optical communications, chip-based 3D printers, trapped-ion quantum systems, and integrated optical tweezers.

In Sec. 9.1, we presented the first visible-light integrated-OPA-based FSOC transmitter and used it to demonstrate the first integrated-OPA-based UWOC link. We experimentally demonstrated a 1-Gbps on-off-keying (OOK) link and an electronically-

switchable point-to-multipoint link with channel selectivity of greater than 19 dB through a water-filled tank. This integrated OPA transmitter chip can reduce the size, weight, and mechanical complexity of apparatus for UWOC systems.

In Sec. 9.2, we combined the fields of silicon photonics and photochemistry to propose the first chip-based 3D-printing technology. The proposed system consists of only a single millimeter-scale photonic chip without any moving parts that emits reconfigurable visible-light holograms up into a simple stationary resin well to enable non-mechanical volumetric 3D printing. The chip-based 3D-printing technology introduced in this work has the potential to enable a highly-compact, portable, and low-cost solution for the next generation of 3D printers.

In Sec. 9.3, we developed a framework for two advanced trapped-ion cooling schemes, PG and EIT, using a visible-wavelength silicon-photonics platform at 422 nm. We have also developed designs of key integrated-photonics components required to realize these architectures. This approach provides a scalable platform that promises more rapid cooling of multiple vibrational modes when compared to previously shown integrated approaches. Additionally, we designed the first integrated polarization rotators and splitter operating at blue wavelengths, enabling integrated polarization-diversity schemes, increased datacom channel density, and advanced chip-scale atomic systems.

In Sec. 9.4, we introduced a new modality for integrated optical tweezers, presenting a fundamentally different approach based on integrated OPAs that enables significantly larger standoff distances and arbitrary active tweezing functionality. This OPA-based approach offers the advantages in cost, footprint, complexity, and mass-producibility of integrated tweezers, while providing much of the functionality of bulk-optical systems. It thus represents a significant improvement in the utility and compatibility of integrated optical tweezers for biological research and opens the door to a variety of experiments that have not been previously possible with prior implementations of integrated tweezers, spanning biophysics research with microsphere-conjugated molecules, cell experimentation and sorting, and emerging in-vivo trapping research.

Chapter 10

Conclusion

In summary, in this work, recent advances in the development of a novel integrated-photonics-based holographic display, VIPER (Visible Integrated Photonics Enhanced Reality), were reviewed.

In Ch. 1, the general VIPER display concept was proposed and outlined. The VIPER display consists of a single discreet transparent chip that sits directly in front of the user's eye and projects visible-light 3D holograms that only the user can see. It presents a highly discreet and fully holographic solution for the next generation of augmented-reality displays.

In Ch. 2, to enable fabrication of the VIPER display, the first transparent 300-mm-wafer foundry platform on glass and the first 300-mm-wafer foundry platform on flexible substrates were developed for visible-light integrated photonics. First, we developed a visible-light silicon-photonics platform and wafer-scale fabrication process. Then, we developed a wafer-scale transfer process to transfer photonic layers from rigid and opaque silicon handle wafers to unique substrates. Next, we developed a transparent platform and wafer-scale fabrication process. We demonstrated fabricated transparent silicon-photonics wafers and chips. Finally, we developed a wafer-scale flexible platform and wafer-scale fabrication process. We demonstrated fabricated flexible silicon-photonics wafers and chips, and performed optical characterization and bend durability studies. This platform and wafer-scale fabrication process for photonics wafers that are transparent or flexible opens the door for the

field of silicon photonics to new application areas.

In Ch. 3, as an initial proof-of-concept demonstration, a novel passive optical-phased-array-based architecture and holographic image encoding methodology were developed and used to demonstrate a large-scale passive version of the VIPER display that generates a static virtual holographic image of a wire-framed cube.

Then, to enable compact and efficient modulation for dynamic encoding of the VIPER display, liquid-crystal material was integrated into the VIPER platform and used to demonstrate the first integrated visible-light liquid-crystal-based phase and amplitude modulators. In Ch. 4, background information on important liquid-crystal properties, such as birefringence and molecular alignment, were discussed. Additionally, integration of liquid-crystal medium with the developed photonics platform and overall liquid-crystal operation were described. Furthermore, the in-house chip-scale liquid-crystal packaging process was outlined, which consists of the back-end steps of reactive-ion etching, photolithography, photonic-to-glass chip alignment, liquid-crystal injection, and final cavity sealing.

In Ch. 5, the first integrated visible-light liquid-crystal-based phase modulators were proposed, developed, and experimentally demonstrated. These devices leverage the birefringence of liquid crystal to actively tune the effective index of a silicon-nitride waveguide and induce a phase shift over the device length. The device operation was described, key variables that affect the mode interaction and resulting phase shift were discussed, and phase modulation was experimentally demonstrated. An example device was experimentally shown to achieve a 41π phase shift within ± 2.4 V for a 500-μm-long modulator, which means that a 2π phase shifter would need to be only 24.4 μm long. When compared to traditional silicon-nitride phase modulators based on heaters, which are on the order of hundreds of microns to several millimeters long, this liquid-crystal-based device is one to two orders of magnitude shorter. This device is a compact and low-power solution to the challenge of integrated phase modulation in silicon nitride.

In Ch. 6, we proposed and experimentally demonstrated the first integrated visible-light liquid-crystal-based variable-tap amplitude modulators. These devices leverage

the birefringence of liquid-crystal medium to actively tune the coupling coefficient between two waveguides and, hence, vary the amplitude of light coupled between these waveguides. First, we proposed and developed the theory behind these integrated liquid-crystal-based variable-tap devices. Next, we outlined the design procedure for how we determine the optimal waveguide widths and coupler lengths of these devices to maximize amplitude modulation. Finally, we demonstrated experimental results of an example fabricated device that achieves strong amplitude modulation with a tradeoff of higher insertion loss, showing amplitude modulation with 15.4-dB tap-port extinction and 36% thru-to-tap-port switching within ± 3.1 V for a 14.7-μm-long device, as well as a complementary example fabricated device that maintains low insertion loss with a slightly lower port switching of 13% for an 8-μm-long device, both at a 637-nm operating wavelength. These small-form-factor variable-tap devices provide a compact and low-power solution to integrated visible-light amplitude modulation and will enable high-density integrated visible-light systems in the future.

In Ch. 7, we presented the first proposal and demonstration of liquid-crystal-based integrated optical phased arrays. We developed a cascaded integrated OPA architecture with a compact and power-efficient LC-based phase-shifting region and used it to enable visible-light beam forming and steering. We demonstrated vital device design, including vertical-layer transitions, LC-based phase modulators, evanescent taps, and grating-based antennas. We fabricated this OPA system and used it to experimentally demonstrate beam steering at a 632.8-nm wavelength with a $0.4^\circ \times 1.6^\circ$ power full-width at half maximum and 7.2° beam-steering range within ± 3.4 V.

In Sec. 8.1, these liquid-crystal-based components were used to develop a novel compact and efficient active version of the optical-phased-array-based VIPER pixel and experimentally validate its functionality. Using this active pixel as a building block, the architecture for the full active VIPER display was developed and used to demonstrate initial dynamic video display functionality with a proof-of-concept 4x4 pixel display, in Sec. 8.2. The path towards further scaling to a large-scale active display with increased number of pixels and multi-wavelength functionality

was discussed.

In Ch. 9, applications beyond augmented reality were presented, including underwater optical communications, chip-based 3D printers, trapped-ion quantum systems, and integrated optical tweezers. In Sec. 9.1, we presented the first visible-light integrated-OPA-based FSOC transmitter and used it to demonstrate the first integrated-OPA-based UWOC link. In Sec. 9.2 we combined the fields of silicon photonics and photochemistry to propose the first chip-based 3D-printing technology. The proposed system consists of only a single millimeter-scale photonic chip without any moving parts that emits reconfigurable visible-light holograms up into a simple stationary resin well to enable non-mechanical volumetric 3D printing. In Sec. 9.3, we developed a framework for two advanced trapped-ion cooling schemes, PG and EIT, using a visible-wavelength silicon-photonics platform at 422 nm. We have also developed designs of key integrated-photonics components required to realize these architectures. For example, we designed the first integrated polarization rotators and splitter operating at blue wavelengths. In Sec. 9.4, we introduced a new modality for integrated optical tweezers, presenting a fundamentally different approach based on integrated OPAs that enables significantly larger standoff distances and arbitrary active tweezing functionality.

Bibliography

[1] J. Notaros, M. Raval, M. Notaros, and M. R. Watts, "Integrated-phased-array-based visible-light near-eye holographic projector," in *CLEO: Science and Innovations*, p. STu3O.4, Optica Publishing Group, 2019.

[2] M. Raval, A. Yaacobi, and M. R. Watts, "Integrated visible light phased array system for autostereoscopic image projection," *Optics Letters*, vol. 43, no. 15, pp. 21–24, 2018.

[3] T. Agocs, T. Balogh, T. Forgacs, F. Bettio, E. Gobbetti, G. Zanetti, and E. Bouvier, "A large scale interactive holographic display," in *Virtual Reality Conference*, p. 311, IEEE, 2006.

[4] J. Hahn, H. Kim, Y. Lim, G. Park, and B. Lee, "Wide viewing angle dynamic holographic stereogram with a curved array of spatial light modulators," *Optics Express*, vol. 16, no. 16, pp. 12372–12386, 2008.

[5] C. M. Gussen, P. S. Diniz, M. L. Campos, W. A. Martins, F. M. Costa, and J. N. Gois, "A survey of underwater wireless communication technologies," *J. Commun. Inf. Sys*, vol. 31, no. 1, pp. 242–255, 2016.

[6] Y. Song, W. Lu, B. Sun, Y. Hong, F. Qu, J. Han, W. Zhang, and J. Xu, "Experimental demonstration of mimo-ofdm underwater wireless optical communication," *Optics Communications*, vol. 403, pp. 205–210, 2017.

[7] G. Cossu, R. Corsini, A. Khalid, S. Balestrino, A. Coppelli, A. Caiti, and E. Ciaramella, "Experimental demonstration of high speed underwater visible light communications," in *2013 2nd International workshop on optical wireless communications (IWOW)*, pp. 11–15, IEEE, 2013.

[8] T.-C. Wu, Y.-C. Chi, H.-Y. Wang, C.-T. Tsai, and G.-R. Lin, "Blue laser diode enables underwater communication at 12.4 gbps," *Scientific Reports*, vol. 7, p. 40480, 2017.

[9] G. Schirripa Spagnolo, L. Cozzella, and F. Leccese, "Underwater optical wireless communications: Overview," *Sensors*, vol. 20, no. 8, p. 2261, 2020.

[10] R. J. Niffenegger, J. Stuart, C. Sorace-Agaskar, D. Kharas, S. Bramhavar, C. D. Bruzewicz, W. Loh, R. T. Maxson, R. McConnell, D. Reens, G. N. West, J. M.

Sage, and J. Chiaverini, "Integrated multi-wavelength control of an ion qubit," *Nature*, vol. 586, no. 7830, pp. 538–542, 2020.

[11] A. Hattori, S. Corsetti, T. Sneh, M. Notaros, R. Swint, P. T. Callahan, C. D. Bruzewicz, F. Knollmann, R. McConnell, J. Chiaverini, *et al.*, "Integrated-photonics-based architectures for polarization-gradient and eit cooling of trapped ions," in *Frontiers in Optics*, pp. FM4B–3, Optica Publishing Group, 2022.

[12] G. Moody, V. J. Sorger, D. J. Blumenthal, P. W. Juodawlkis, W. Loh, C. Sorace-Agaskar, A. E. Jones, K. C. Balram, J. C. F. Matthews, A. Laing, *et al.*, "2022 roadmap on integrated quantum photonics," *Journal of Physics: Photonics*, vol. 4, no. 1, p. 012501, 2022.

[13] J. Wang, F. Sciarrino, A. Laing, and M. G. Thompson, "Integrated photonic quantum technologies," *Nature Photonics*, vol. 14, no. 5, pp. 273–284, 2020.

[14] K. K. Mehta, C. Zhang, M. Malinowski, T.-L. Nguyen, M. Stadler, and J. P. Home, "Integrated optical multi-ion quantum logic," *Nature*, vol. 586, no. 7830, pp. 533–537, 2020.

[15] W. D. Sacher, F.-D. Chen, H. Moradi-Chameh, X. Liu, I. F. Almog, T. Lordello, M. Chang, A. Naderian, T. M. Fowler, E. Segev, T. Xue, S. Mahallati, T. A. Valiante, L. C. Moreaux, J. K. S. Poon, and M. L. Roukes, "Optical phased array neural probes for beam-steering in brain tissue," *Optics Letters*, vol. 47, no. 5, pp. 1073–1076, 2022.

[16] E. Shim, Y. Chen, S. Masmanidis, and M. Li, "Multisite silicon neural probes with integrated silicon nitride waveguides and gratings for optogenetic applications," *Scientific Reports*, vol. 6, p. 22693, 2016.

[17] W. D. Sacher, X. Luo, Y. Yang, F.-D. Chen, T. Lordello, J. C. C. Mak, X. Liu, T. Hu, T. Xue, P. G.-Q. Lo, M. L. Roukes, and J. K. S. Poon, "Visible-light silicon nitride waveguide devices and implantable neurophotonic probes on thinned 200 mm silicon wafers," *Optics Express*, vol. 27, no. 26, pp. 37400–37418, 2019.

[18] W. D. Sacher, X. Liu, I. F. Almog, A. Fomenko, T. Lordello, F.-D. Chen, H. Moradi-Chameh, A. Naderian, M. Chang, T. M. Fowler, T. A. Valiante, A. M. Lozano, L. C. Moreaux, J. K. S. Poon, and M. L. Roukes, "Nanophotonic neural probes for in vivo light sheet imaging," in *Conference on Lasers and Electro-Optics*, p. SM4H.6, Optica Publishing Group, 2019.

[19] A. Mohanty, Q. Li, M. A. Tadayon, S. P. Roberts, G. R. Bhatt, E. Shim, X. Ji, J. Cardenas, S. A. Miller, A. Kepecs, and M. Lipson, "Reconfigurable nanophotonic silicon probes for sub-millisecond deep-brain optical stimulation," *Nature Biomedical Engineering*, vol. 4, pp. 223–231, 2020.

[20] M. A. Livingston, L. J. Rosenblum, D. G. Brown, G. S. Schmidt, S. J. Julier, Y. Baillot, J. E. Swan, Z. Ai, and P. Maassel, "Military applications of augmented reality," *Handbook of augmented reality*, pp. 671–706, 2011.

[21] T. Sielhorst, M. Feuerstein, and N. Navab, "Advanced medical displays: A literature review of augmented reality," *Journal of Display Technology*, vol. 4, no. 4, pp. 451–467, 2008.

[22] W. S. Khor, B. Baker, K. Amin, A. Chan, K. Patel, and J. Wong, "Augmented and virtual reality in surgery—the digital surgical environment: applications, limitations and legal pitfalls," *Annals of translational medicine*, vol. 4, no. 23, 2016.

[23] T. Morimoto, T. Kobayashi, H. Hirata, K. Otani, M. Sugimoto, M. Tsukamoto, T. Yoshihara, M. Ueno, and M. Mawatari, "Xr (extended reality: virtual reality, augmented reality, mixed reality) technology in spine medicine: status quo and quo vadis," *Journal of Clinical Medicine*, vol. 11, no. 2, p. 470, 2022.

[24] Y.-C. Liu and M.-H. Wen, "Comparison of head-up display (hud) vs. head-down display (hdd): driving performance of commercial vehicle operators in taiwan," *International Journal of Human-Computer Studies*, vol. 61, no. 5, pp. 679–697, 2004.

[25] J. Xiong, E.-L. Hsiang, Z. He, T. Zhan, and S.-T. Wu, "Augmented reality and virtual reality displays: emerging technologies and future perspectives," *Light: Science & Applications*, vol. 10, no. 1, p. 216, 2021.

[26] B. Kress and T. Starner, "A review of head-mounted displays (hmd) technologies and applications for consumer electronics," *Photonic Applications for Aerospace, Commercial, and Harsh Environments IV*, vol. 8720, pp. 62–74, 2013.

[27] L. Google, "Discover glass enterprise." https://www.google.com/glass/start/.

[28] C. Microsoft, "Microsoft hololens 2." https://microsoft.com/microsoft-hololens/en-us.

[29] G. Kramida, "Resolving the vergence-accommodation conflict in head-mounted displays," *IEEE transactions on visualization and computer graphics*, vol. 22, no. 7, pp. 1912–1931, 2015.

[30] D. M. Hoffman, A. R. Girshick, K. Akeley, and M. S. Banks, "Vergence–accommodation conflicts hinder visual performance and cause visual fatigue," *Journal of Vision*, vol. 8, no. 3, pp. 33–33, 2008.

[31] T. Shibata, J. Kim, D. M. Hoffman, and M. S. Banks, "Visual discomfort with stereo displays: effects of viewing distance and direction of vergence-accommodation conflict," in *Stereoscopic Displays and Applications XXII*, vol. 7863, pp. 222–230, SPIE, 2011.

[32] C. Martinez, V. Krotov, B. Meynard, and D. Fowler, "See-through holographic retinal projection display concept," *Optica*, vol. 5, no. 10, pp. 1200–1209, 2018.

[33] B. Meynard, K. Millard, D. Fowler, Y. Lee, S. Garcia, K. Ribaud, P. Grosse, and C. Martinez, "Lpcvd silicon nitride photonic integrated components designed at 532 nm wavelength for a novel retinal projection concept and visible domain applications," *Journal of Lightwave Technology*, 2023.

[34] G.-Y. Lee, J.-Y. Hong, S. Hwang, S. Moon, H. Kang, S. Jeon, H. Kim, J.-H. Jeong, and B. Lee, "Metasurface eyepiece for augmented reality," *Nature Communications*, vol. 9, no. 1, p. 4562, 2018.

[35] S. Lan, X. Zhang, M. Taghinejad, S. Rodrigues, K.-T. Lee, Z. Liu, and W. Cai, "Metasurfaces for near-eye augmented reality," *ACS Photonics*, vol. 6, no. 4, pp. 864–870, 2019.

[36] C. Jang, C.-K. Lee, J. Jeong, G. Li, S. Lee, J. Yeom, K. Hong, and B. Lee, "Recent progress in see-through three-dimensional displays using holographic optical elements," *Applied Optics*, vol. 55, no. 3, pp. A71–A85, 2016.

[37] J. Xiong, K. Yin, K. Li, and S.-T. Wu, "Holographic optical elements for augmented reality: principles, present status, and future perspectives," *Advanced Photonics Research*, vol. 2, no. 1, p. 2000049, 2021.

[38] E. Bayati, A. Wolfram, S. Colburn, L. Huang, and A. Majumdar, "Design of achromatic augmented reality visors based on composite metasurfaces," *Applied Optics*, vol. 60, no. 4, pp. 844–850, 2021.

[39] A. H. Atabaki, S. Moazeni, F. Pavanello, H. Gevorgyan, J. Notaros, L. Alloatti, M. T. Wade, C. Sun, S. A. Kruger, H. Meng, K. A. Qubaisi, I. Wang, B. Zhang, A. Khilo, C. V. Baiocco, M. A. Popović, V. M. Stojanović, and R. J. Ram, "Integrating photonics with silicon nanoelectronics for the next generation of systems on a chip," *Nature*, vol. 556, no. 7701, pp. 349–354, 2018.

[40] C. Sun, M. T. Wade, Y. Lee, J. S. Orcutt, L. Alloatti, M. S. Georgas, A. S. Waterman, J. M. Shainline, R. R. Avizienis, S. Lin, B. R. Moss, R. Kumar, F. Pavanello, A. H. Atabaki, H. M. Cook, A. J. Ou, J. C. Leu, Y.-H. Chen, K. Asanović, R. J. Ram, M. A. Popović, and V. M. Stojanović, "Single-chip microprocessor that communicates directly using light," *Nature*, vol. 528, no. 7583, pp. 534–538, 2015.

[41] D. T. Spencer, T. Drake, T. C. Briles, J. Stone, L. C. Sinclair, C. Fredrick, Q. Li, D. Westly, B. R. Ilic, A. Bluestone, *et al.*, "An optical-frequency synthesizer using integrated photonics," *Nature*, vol. 557, no. 7703, pp. 81–85, 2018.

[42] C. V. Poulton, M. J. Byrd, P. Russo, E. Timurdogan, M. Khandaker, D. Vermeulen, and M. R. Watts, "Long-range lidar and free-space data communication with high-performance optical phased arrays," *IEEE Journal of Selected Topics in Quantum Electronics*, vol. 25, no. 5, pp. 1–8, 2019.

[43] P. Bhargava, T. Kim, C. V. Poulton, J. Notaros, A. Yaacobi, E. Timurdogan, C. Baiocco, N. Fahrenkopf, S. Kruger, T. Ngai, Y. Timalsina, M. R. Watts, and V. Stojanović, "Fully integrated coherent lidar in 3d-integrated silicon photonics/65nm cmos," in *2019 Symposium on VLSI Circuits*, pp. C262–C263, IEEE, 2019.

[44] C. V. Poulton, A. Yaacobi, D. B. Cole, M. J. Byrd, M. Raval, D. Vermeulen, and M. R. Watts, "Coherent solid-state lidar with silicon photonic optical phased arrays," *Optics Letters*, vol. 42, no. 20, pp. 4091–4094, 2017.

[45] J. Sun, E. Timurdogan, A. Yaacobi, E. S. Hosseini, and M. R. Watts, "Large-scale nanophotonic phased array," *Nature*, vol. 493, no. 7431, pp. 195–199, 2013.

[46] T. Kim, P. Bhargava, C. V. Poulton, J. Notaros, A. Yaacobi, E. Timurdogan, C. Baiocco, N. Fahrenkopf, S. Kruger, T. Ngai, Y. Timalsina, M. R. Watts, and V. Stojanović, "A single-chip optical phased array in a wafer-scale silicon photonics/cmos 3d-integration platform," *IEEE Journal of Solid-State Circuits*, vol. 54, no. 11, pp. 3061–3074, 2019.

[47] J. Notaros, C. V. Poulton, M. Raval, and M. R. Watts, "Near-field-focusing integrated optical phased arrays," *Journal of Lightwave Technology*, vol. 36, no. 24, pp. 5912–5920, 2018.

[48] J. Notaros, N. Li, C. V. Poulton, Z. Su, M. J. Byrd, E. S. Magden, E. Timurdogan, C. Baiocco, N. M. Fahrenkopf, and M. R. Watts, "Cmos-compatible optical phased array powered by a monolithically-integrated erbium laser," *Journal of Lightwave Technology*, vol. 37, no. 24, pp. 5982–5987, 2019.

[49] M. J. Heck, "Highly integrated optical phased arrays: photonic integrated circuits for optical beam shaping and beam steering," *Nanophotonics*, vol. 6, no. 1, pp. 93–107, 2017.

[50] T. Komljenovic, R. Helkey, L. Coldren, and J. E. Bowers, "Sparse aperiodic arrays for optical beam forming and lidar," *Optics Express*, vol. 25, no. 3, pp. 2511–2528, 2017.

[51] F. Aflatouni, B. Abiri, A. Rekhi, and A. Hajimiri, "Nanophotonic projection system," *Optics Express*, vol. 23, no. 16, pp. 21012–21022, 2015.

[52] R. Fatemi, A. Khachaturian, and A. Hajimiri, "A nonuniform sparse 2-d large-fov optical phased array with a low-power pwm drive," *IEEE Journal of Solid-State Circuits*, vol. 54, no. 5, pp. 1200–1215, 2019.

[53] D. N. Hutchison, J. Sun, J. K. Doylend, R. Kumar, J. Heck, W. Kim, C. T. Phare, A. Feshali, and H. Rong, "High-resolution aliasing-free optical beam steering," *Optica*, vol. 3, no. 8, pp. 887–890, 2016.

[54] J. Notaros, C. V. Poulton, M. J. Byrd, M. Raval, and M. R. Watts, "Integrated optical phased arrays for quasi-bessel-beam generation," *Optics Letters*, vol. 42, no. 17, pp. 3510–3513, 2017.

[55] J. Zhou, J. Sun, A. Yaacobi, C. V. Poulton, and M. R. Watts, "Design of 3d hologram emitting optical phased arrays," in *Integrated Photonics Research, Silicon and Nanophotonics*, pp. IT4A–7, Optica Publishing Group, 2015.

[56] W. S. Rabinovich, P. G. Goetz, M. Pruessner, R. Mahon, M. S. Ferraro, D. Park, E. Fleet, and M. J. DePrenger, "Free space optical communication link using a silicon photonic optical phased array," in *Free-Space Laser Communication and Atmospheric Propagation XXVII*, vol. 9354, pp. 96–101, SPIE, 2015.

[57] M. J. Byrd, C. V. Poulton, M. Khandaker, E. Timurdogan, D. Vermeulen, and M. R. Watts, "Free-space communication links with transmitting and receiving integrated optical phased arrays," in *Frontiers in Optics*, pp. FTu4E–1, Optica Publishing Group, 2018.

[58] S. Chung, H. Abediasl, and H. Hashemi, "A monolithically integrated large-scale optical phased array in silicon-on-insulator cmos," *IEEE Journal of Solid-State Circuits*, vol. 53, no. 1, pp. 275–296, 2017.

[59] M. S. Hai, A. Leinse, T. Veenstra, and O. Liboiron-Ladouceur, "A thermally tunable 1× 4 channel wavelength demultiplexer designed on a low-loss si3n4 waveguide platform," in *Photonics*, vol. 2, pp. 1065–1080, MDPI, 2015.

[60] Z. Yong, H. Chen, X. Luo, A. Govdeli, H. Chua, S. S. Azadeh, A. Stalmashonak, G.-Q. Lo, J. K. Poon, and W. D. Sacher, "Power-efficient silicon nitride thermo-optic phase shifters for visible light," *Optics Express*, vol. 30, no. 5, pp. 7225–7237, 2022.

[61] M. Notaros, T. Dyer, M. Raval, C. Baiocco, J. Notaros, and M. R. Watts, "Integrated visible-light liquid-crystal-based phase modulators," *Optics Express*, vol. 30, no. 8, pp. 13790–13801, 2022.

[62] M. Notaros, T. Dyer, A. Hattori, K. Fealey, S. Kruger, and J. Notaros, "Flexible wafer-scale silicon-photonics fabrication platform," in *Frontiers in Optics*, pp. FW1E–3, Optica Publishing Group, 2022.

[63] E. Timurdogan, Z. Su, C. V. Poulton, M. J. Byrd, S. Xin, R.-J. Shiue, B. R. Moss, E. S. Hosseini, and M. R. Watts, "Aim process design kit (aimpdkv2. 0): Silicon photonics passive and active component libraries on a 300mm wafer," in *Optical Fiber Communication Conference*, pp. M3F–1, Optica Publishing Group, 2018.

[64] M. de Cea, Z. Li, M. Notaros, J. Notaros, and R. J. Ram, "Single-mode waveguide-coupled light emitting diodes in unmodified silicon photonics fabrication processes," *APL Photonics*, vol. 8, no. 8, 2023.

[65] C. Sorace-Agaskar, D. Kharas, S. Yegnanarayanan, R. T. Maxson, G. N. West, W. Loh, S. Bramhavar, R. J. Ram, J. Chiaverini, J. Sage, *et al.*, "Versatile silicon nitride and alumina integrated photonic platforms for the ultraviolet to short-wave infrared," *IEEE Journal of Selected Topics in Quantum Electronics*, vol. 25, no. 5, pp. 1–15, 2019.

[66] Z. Ma, "An electronic second skin," *Science*, vol. 333, no. 6044, pp. 830–831, 2011.

[67] H. C. Ko, M. P. Stoykovich, J. Song, V. Malyarchuk, W. M. Choi, C.-J. Yu, J. B. Geddes Iii, J. Xiao, S. Wang, Y. Huang, *et al.*, "A hemispherical electronic eye camera based on compressible silicon optoelectronics," *Nature*, vol. 454, no. 7205, pp. 748–753, 2008.

[68] M. Raval, C. V. Poulton, and M. R. Watts, "Unidirectional waveguide grating antennas with uniform emission for optical phased arrays," *Optics Letters*, vol. 42, no. 13, pp. 2563–2566, 2017.

[69] R. W. Gerchberg and W. O. Saxton, "A practical algorithm for the determination of plane from image and diffraction pictures," *Optik*, vol. 35, no. 2, pp. 237–246, 1972.

[70] J. R. Fienup, "Reconstruction of an object from the modulus of its fourier transform," *Optics Letters*, vol. 3, no. 1, pp. 27–29, 1978.

[71] M. Raval, *Integrated optical phased arrays for three-dimensional display applications*. PhD thesis, Massachusetts Institute of Technology, 2020.

[72] M. Notaros, M. Raval, J. Notaros, and M. R. Watts, "Integrated visible-light liquid-crystal phase modulator," in *Frontiers in Optics*, p. FW6B.5, Optica Publishing Group, 2018.

[73] A. G. Coleto, M. Notaros, and J. Notaros, "Integrated liquid-crystal-based modulators: Packaging processes and evaluation techniques," in *IPC*, IEEE, 2023.

[74] K. Shtyrkova, P. T. Callahan, N. Li, E. S. Magden, A. Ruocco, D. Vermeulen, F. X. Kärtner, M. R. Watts, and E. P. Ippen, "Integrated cmos-compatible q-switched mode-locked lasers at 1900nm with an on-chip artificial saturable absorber," *Optics Express*, vol. 27, no. 3, pp. 3542–3556, 2019.

[75] W. D. Sacher, Y. Huang, G.-Q. Lo, and J. K. Poon, "Multilayer silicon nitride-on-silicon integrated photonic platforms and devices," *Journal of Lightwave Technology*, vol. 33, no. 4, pp. 901–910, 2015.

[76] D. Pérez, J. Fernández, R. Baños, J. D. Doménech, A. M. Sánchez, J. M. Cirera, R. Mas, J. Sánchez, S. Durán, E. Pardo, *et al.*, "Thermal tuners on a silicon nitride platform," *arXiv preprint arXiv:1604.02958*, 2016.

[77] V. S. S. Sundaram, E. Manfreda-Schulz, T. Palone, V. Deenadayalan, G. A. Howland, and S. F. Preble, "Thermo-optic silicon nitride phase shifters for visible light," in *Frontiers in Optics*, p. JTu5A.32, Optica Publishing Group, 2022.

[78] L. Van Iseghem, U. Khan, P. Edinger, C. Errando-Herranz, A. Y. Takabayashi, H. Sattari, K. B. Gylfason, N. Quack, J. Beeckman, and W. Bogaerts, "Liquid crystal phase shifter integrated in a silicon photonics platform," in *22nd European Conference on Integrated Optics, ECIO 2020*, 2020.

[79] Y. Atsumi, K. Watabe, N. Uda, N. Miura, and Y. Sakakibara, "Initial alignment control technique using on-chip groove arrays for liquid crystal hybrid silicon optical phase shifters," *Optics Express*, vol. 27, no. 6, pp. 8756–8767, 2019.

[80] Y. Xing, T. Ako, J. P. George, D. Korn, H. Yu, P. Verheyen, M. Pantouvaki, G. Lepage, P. Absil, A. Ruocco, C. Koos, J. Leuthold, K. Neyts, J. Beeckman, and W. Bogaerts, "Digitally controlled phase shifter using an soi slot waveguide with liquid crystal infiltration," *IEEE Photonics Technology Letters*, vol. 27, no. 12, pp. 1269–1272, 2015.

[81] J. Pfeifle, L. Alloatti, W. Freude, J. Leuthold, and C. Koos, "Silicon-organic hybrid phase shifter based on a slot waveguide with a liquid-crystal cladding," *Optics Express*, vol. 20, no. 14, pp. 15359–15376, 2012.

[82] W. De Cort, J. Beeckman, T. Claes, K. Neyts, and R. Baets, "Wide tuning of silicon-on-insulator ring resonators with a liquid crystal cladding," *Optics Letters*, vol. 36, no. 19, pp. 3876–3878, 2011.

[83] W. De Cort, J. Beeckman, R. James, F. A. Fernández, R. Baets, and K. Neyts, "Tuning of silicon-on-insulator ring resonators with liquid crystal cladding using the longitudinal field component," *Optics Letters*, vol. 34, no. 13, pp. 2054–2056, 2009.

[84] A. Di Falco and G. Assanto, "Tunable wavelength-selective add–drop in liquid crystals on a silicon microresonator," *Optics Communications*, vol. 279, no. 1, pp. 210–213, 2007.

[85] C. Vázquez, P. Contreras, J. Montalvo, J. M. S. Pena, A. d'Alessandro, and D. Donisi, "Switches and tunable filters based on ring resonators and liquid crystals," in *Photonic Materials, Devices, and Applications II*, vol. 6593, pp. 406–415, SPIE, 2007.

[86] B. Maune, R. Lawson, C. Gunn, A. Scherer, and L. Dalton, "Electrically tunable ring resonators incorporating nematic liquid crystals as cladding layers," *Applied Physics Letters*, vol. 83, no. 23, pp. 4689–4691, 2003.

[87] J. Ptasinski, S. W. Kim, L. Pang, I.-C. Khoo, and Y. Fainman, "Optical tuning of silicon photonic structures with nematic liquid crystal claddings," *Optics Letters*, vol. 38, no. 12, pp. 2008–2010, 2013.

[88] T.-J. Wang, W.-J. Li, and T.-J. Chen, "Radially realigning nematic liquid crystal for efficient tuning of microring resonators," *Optics Express*, vol. 21, no. 23, pp. 28974–28979, 2013.

[89] J. Dai, M. Zhang, F. Zhou, Y. Wang, L. Lu, and D. Liu, "Efficiently tunable and fabrication tolerant double-slot microring resonators incorporating nematic liquid crystal as claddings," *Optics Communications*, vol. 350, pp. 235–240, 2015.

[90] Z. Zhang, Z. You, and D. Chu, "Fundamentals of phase-only liquid crystal on silicon (LCOS) devices," *Light: Science & Applications*, vol. 3, p. e213, 2014.

[91] W. P. B. Jr. and L. A. Lei, "Advances in liquid crystal on silicon (LCOS) spatial light modulator technology," in *SPIE Display Technologies and Applications for Defense, Security, and Avionics*, vol. 8736, SPIE, 2013.

[92] N. Collings, T. Davey, J. Christmas, D. Chu, and B. Crossland, "The applications and technology of phase-only liquid crystal on silicon devices," *Journal of Display Technology*, vol. 7, no. 3, pp. 112–119, 2011.

[93] P. G. de Gennes and J. Prost, *The Physics of Liquid Crystals*. Oxford University Press, 1995.

[94] A. Sneh and K. M. Johnson, "High-speed continuously tunable liquid crystal filter for wdm networks," *Journal of Lightwave Technology*, vol. 14, no. 6, pp. 1067–1080, 1996.

[95] J. Beeckman, K. Neyts, and P. J. M. Vanbrabant, "Liquid-crystal photonic applications," *Optical Engineering*, vol. 50, no. 8, pp. 1–18, 2011.

[96] R. A. Alla, *On the Control of Nematic Liquid Crystal Alignment*. PhD thesis, University of Gothenburg, 2013.

[97] J. Li, C.-H. Wen, S. Gauza, R. Lu, and S.-T. Wu, "Refractive indices of liquid crystals for display applications," *Journal of Display Technology*, vol. 1, no. 1, p. 51, 2005.

[98] V. Tkachenko, A. Marino, and G. Abbate, "Study of nematic liquid crystals by spectroscopic ellipsometry," *Molecular Crystals and Liquid Crystals*, vol. 527, no. 1, pp. 80–236, 2010.

[99] H. Jansen, H. Gardeniers, M. de Boer, M. Elwenspoek, and J. Fluitman, "A survey on the reactive ion etching of silicon in microtechnology," *Journal of Micromechanics and Microengineering*, vol. 6, no. 1, pp. 14–28, 1996.

[100] S. Tachi, K. Tsujimoto, and S. Okudaira, "Low-temperature reactive ion etching and microwave plasma etching of silicon," *Applied Physics Letters*, vol. 52, no. 8, pp. 616–618, 1988.

[101] M. Elwenspoek, U. Lindberg, H. Kok, and L. Smith, "Wet chemical etching mechanism of silicon," in *IEEE Micro Electro Mechanical Systems An Investigation of Micro Structures, Sensors, Actuators, Machines and Robotic Systems*, pp. 223–228, IEEE, 1994.

[102] A. J. van Roosmalen, "Review: dry etching of silicon oxide," *Vacuum*, vol. 34, no. 3–4, pp. 429–436, 1984.

[103] R. Sun, M. Beals, A. Pomerene, J. Cheng, C.-y. Hong, L. Kimerling, and J. Michel, "Impedance matching vertical optical waveguide couplers for dense high index contrast circuits," *Optics Express*, vol. 16, no. 16, pp. 11682–11690, 2008.

[104] O. Sato, N. Iwata, J. Kawamura, T. Maeda, Y. Tsujii, J. Watanabe, and M. Tokita, "An in-plane switching liquid crystal cell with weakly anchored liquid crystals on the electrode substrate," *Journal of Materials Chemistry C*, vol. 5, no. 18, pp. 4384–4387, 2017.

[105] J. H. Yoon, E. J. Seo, S. J. Lee, Y. J. Lim, H. S. Shin, S. M. Song, J.-M. Myoung, and S. H. Lee, "Fast switching and luminance-controlled fringe-field switching liquid crystal device for vehicle display," *Liquid Crystals*, vol. 46, no. 11, pp. 1747–1752, 2019.

[106] W.-S. Kang, J.-W. Moon, G.-D. Lee, S.-H. Lee, J.-H. Lee, B.-K. Kim, and H.-C. Choi, "Retardation free in-plane switching liquid crystal display with high speed and wide-view angle," *Journal of the Optical Society of Korea*, vol. 15, no. 2, pp. 161–167, 2011.

[107] H. S. Shin, R. Manda, T. H. Kim, J. G. Park, Y. J. Lim, B. K. Kim, Y. H. Lee, and S. H. Lee, "Multi-layered carbon nanotube uv polariser for photo-alignment of liquid crystals," *Liquid Crystals*, vol. 47, no. 11, pp. 1604–1611, 2020.

[108] M. Geis, T. Lyszczarz, R. Osgood, and B. Kimball, "30 to 50 ns liquid-crystal optical switches," *Optics Express*, vol. 18, no. 18, pp. 18886–18893, 2010.

[109] J. Notaros, M. Notaros, M. Raval, and M. R. Watts, "Liquid-crystal-based visible-light integrated optical phased arrays," in *CLEO: Science and Innovations*, p. STu3O.3, Optica Publishing Group, 2019.

[110] M. Notaros, J. Notaros, M. Raval, and M. R. Watts, "Integrated visible-light liquid-crystal variable-tap amplitude modulator," in *Integrated Photonics Research, Silicon and Nanophotonics*, p. ITh2C.6, Optica Publishing Group, 2019.

[111] D. DeSantis, M. Notaros, M. Torres, and J. Notaros, "Underwater wireless optical communications using integrated optical phased arrays," in *IPC*, IEEE, 2023.

[112] M. C. Shin, A. Mohanty, K. Watson, G. R. Bhatt, C. T. Phare, S. A. Miller, M. Zadka, B. S. Lee, X. Ji, I. Datta, and M. Lipson, "Chip-scale blue light phased array," *Optics Letters*, vol. 45, no. 7, pp. 1934–1937, 2020.

[113] Z. Zhang, M. Notaros, Z. Gao, U. Chakraborty, J. Notaros, and D. S. Boning, "Impact of process variations on splitter-tree-based integrated optical phased arrays," *Optics Express*, vol. 31, no. 8, pp. 12912–12921, 2023.

[114] Z. Zhang, M. Notaros, Z. Gao, U. Chakraborty, J. Notaros, and D. S. Boning, "Impact of spatial variations on splitter-tree-based integrated optical phased arrays," in *Optical Fiber Communication Conference*, pp. W2A–35, Optica Publishing Group, 2023.

[115] J. Notaros, F. Pavanello, M. T. Wade, C. M. Gentry, A. Atabaki, L. Alloatti, R. J. Ram, and M. A. Popović, "Ultra-efficient cmos fiber-to-chip grating couplers," in *2016 Optical Fiber Communications Conference and Exhibition (OFC)*, pp. 1–3, IEEE, 2016.

[116] Sonardyne, "Bluecomm 200." https://www.sonardyne.com /products/bluecomm-200-wireless-underwater-link/.

[117] O. Korotkova, N. Farwell, and E. Shchepakina, "Light scintillation in oceanic turbulence," *Waves in Random and Complex Media*, vol. 22, no. 2, pp. 260–266, 2012.

[118] S. Corsetti, M. Notaros, T. Sneh, A. Stafford, Z. A. Page, and J. Notaros, "Visible-light integrated optical phased arrays for chip-based 3d printing," in *Integrated Photonics Research, Silicon and Nanophotonics*, pp. IM2B–4, Optica Publishing Group, 2022.

[119] B. Narupai and A. Nelson, "100th anniversary of macromolecular science viewpoint: macromolecular materials for additive manufacturing," *ACS Macro Letters*, vol. 9, no. 5, pp. 627–638, 2020.

[120] T. Wallin, J. Pikul, and R. F. Shepherd, "3d printing of soft robotic systems," *Nature Reviews Materials*, vol. 3, no. 6, pp. 84–100, 2018.

[121] S. C. Ligon, R. Liska, J. Stampfl, M. Gurr, and R. M´ulhaupt, "Polymers for 3d printing and customized additive manufacturing," *Chemical reviews*, vol. 117, no. 15, pp. 10212–10290, 2017.

[122] F. Rajabasadi, L. Schwarz, M. Medina-Sánchez, and O. G. Schmidt, "3d and 4d lithography of untethered microrobots," *Progress in Materials Science*, vol. 120, p. 100808, 2021.

[123] M. Regehly, Y. Garmshausen, M. Reuter, N. F. König, E. Israel, D. P. Kelly, C.-Y. Chou, K. Koch, B. Asfari, and S. Hecht, "Xolography for linear volumetric 3d printing," *Nature*, vol. 588, no. 7839, pp. 620–624, 2020.

[124] B. E. Kelly, I. Bhattacharya, H. Heidari, M. Shusteff, C. M. Spadaccini, and H. K. Taylor, "Volumetric additive manufacturing via tomographic reconstruction," *Science*, vol. 363, no. 6431, pp. 1075–1079, 2019.

[125] A. Stafford, D. Ahn, E. K. Raulerson, K.-Y. Chung, K. Sun, D. M. Cadena, E. M. Forrister, S. R. Yost, S. T. Roberts, and Z. A. Page, "Catalyst halogenation enables rapid and efficient polymerizations with visible to far-red light," *Journal of the American Chemical Society*, vol. 142, no. 34, pp. 14733–14742, 2020.

[126] D. Ahn, L. M. Stevens, K. Zhou, and Z. A. Page, "Rapid high-resolution visible light 3d printing," *ACS Central Science*, vol. 6, no. 9, pp. 1555–1563, 2020.

[127] T. Sneh, A. Hattori, M. Notaros, S. Corsetti, and J. Notaros, "Design of integrated visible-light polarization rotators and splitters," in *Frontiers in Optics*, pp. JTu5A–48, Optica Publishing Group, 2022.

[128] C. D. Bruzewicz, J. Chiaverini, R. McConnell, and J. M. Sage, "Trapped-ion quantum computing: Progress and challenges," *Applied Physics Reviews*, vol. 6, no. 2, 2019.

[129] M. Joshi, A. Fabre, C. Maier, T. Brydges, D. Kiesenhofer, H. Hainzer, R. Blatt, and C. Roos, "Polarization-gradient cooling of 1d and 2d ion coulomb crystals," *New Journal of Physics*, vol. 22, no. 10, p. 103013, 2020.

[130] C. Roos, D. Leibfried, A. Mundt, F. Schmidt-Kaler, J. Eschner, and R. Blatt, "Experimental demonstration of ground state laser cooling with electromagnetically induced transparency," *Physical Review Letters*, vol. 85, no. 26, p. 5547, 2000.

[131] C. Sun, Y. Yu, Y. Ding, Z. Li, W. Qi, and X. Zhang, "Integrated mode-transparent polarization beam splitter supporting thirteen data channels," *Photonics Research*, vol. 8, no. 6, pp. 978–985, 2020.

[132] M. Watts and H. Haus, "Integrated mode-evolution-based polarization rotators," *Optics Letters*, vol. 30, no. 2, pp. 138–140, 2005.

[133] D. Dai and J. E. Bowers, "Novel concept for ultracompact polarization splitter-rotator based on silicon nanowires," *Optics Express*, vol. 19, no. 11, pp. 10940–10949, 2011.

[134] Z. Wang and D. Dai, "Ultrasmall si-nanowire-based polarization rotator," *JOSA B*, vol. 25, no. 5, pp. 747–753, 2008.

[135] F. Zhang, J. Zheng, Y. Song, W. Liu, P. Xu, and A. Majumdar, "Ultrabroadband and compact polarizing beam splitter in silicon photonics," *OSA Continuum*, vol. 3, no. 3, pp. 560–567, 2020.

[136] K. Gallacher, P. F. Griffin, E. Riis, M. Sorel, and D. J. Paul, "Silicon nitride waveguide polarization rotator and polarization beam splitter for chip-scale atomic systems," *APL Photonics*, vol. 7, no. 4, 2022.

[137] T. Sneh, S. Corsetti, M. Notaros, K. Kikkeri, J. Voldman, and J. Notaros, "Optical tweezing of microspheres and cells using integrated optical phased arrays," in *IPC*, IEEE, 2023.

[138] T. Sneh, S. Corsetti, M. Notaros, and J. Notaros, "Focusing integrated optical phased arrays for chip-based optical trapping," in *CLEO: Science and Innovations*, pp. STh4G–4, Optica Publishing Group, 2022.

[139] A. Ashkin, "Acceleration and trapping of particles by radiation pressure," *Physical Review Letters*, vol. 24, no. 4, p. 156, 1970.

[140] O. M. Marago, P. H. Jones, P. G. Gucciardi, G. Volpe, and A. C. Ferrari, "Optical trapping and manipulation of nanostructures," *Nature Nanotechnology*, vol. 8, no. 11, pp. 807–819, 2013.

[141] M. L. Juan, M. Righini, and R. Quidant, "Plasmon nano-optical tweezers," *Nature Photonics*, vol. 5, no. 6, pp. 349–356, 2011.

[142] Y. Sun, X.-C. Yuan, L. Ong, J. Bu, S. Zhu, and R. Liu, "Large-scale optical traps on a chip for optical sorting," *Applied Physics Letters*, vol. 90, no. 3, 2007.

[143] S. Yu, J. Lu, V. Ginis, S. Kheifets, S. W. D. Lim, M. Qiu, T. Gu, J. Hu, and F. Capasso, "On-chip optical tweezers based on freeform optics," *Optica*, vol. 8, no. 3, pp. 409–414, 2021.

[144] J.-Y. Tinevez, N. Perry, J. Schindelin, G. M. Hoopes, G. D. Reynolds, E. Laplantine, S. Y. Bednarek, S. L. Shorte, and K. W. Eliceiri, "Trackmate: An open and extensible platform for single-particle tracking," *Methods*, vol. 115, pp. 80–90, 2017.

[145] G. Pesce, G. Volpe, O. M. Maragó, P. H. Jones, S. Gigan, A. Sasso, and G. Volpe, "Step-by-step guide to the realization of advanced optical tweezers," *JOSA B*, vol. 32, no. 5, pp. B84–B98, 2015.